공학박사 학위논문

Prediction of anisotropic strengths of steel pipe using the homogeneous yield function-based anisotropic hardening model with multi-component evolution law

다중 상태변수를 갖는 비등방성 왜곡경화모델을 이용한 강관의 강도 이방성 예측

2021 년 8 월

서울대학교 대학원

재료공학부

최 홍 진

Prediction of anisotropic strengths of steel pipe using the homogeneous yield function-based anisotropic hardening model with multi-component evolution law

다중 상태변수를 갖는 비등방성 왜곡경화모델을 이용한 강관의 강도 이방성 예측

지도 교수 이 명 규

이 논문을 공학박사 학위논문으로 제출함

2021 년 8 월

서울대학교 대학원

재료공학부

최 홍 진

최홍진의 공학박사 학위논문을 인준함

2021 년 8 월

위 원 장 _____ 유 웅 열 _____

부위원장 _____ 이 명 규 _____

위 원 _____ 한 흥 남 _____

위 원 _____ 이 진 우 _____

위 원 _____ 강 수 창 _____

Abstract

In this study, a numerical model for the prediction of anisotropic strengths of API steel pipe using a distortional anisotropic hardening model, namely, the HAH model, is proposed. The investigated HAH model can express the material behaviors under reverse and cross-loading paths. The multi-component evolution laws for the reverse loading behavior were additionally implemented to improve the predictive accuracy of the existing HAH model. For the stable finite element implementation of the model, the fully implicit stress update algorithm was first developed. The proposed algorithm solves a complete set of residuals as nonlinear functions of stress, equivalent plastic strain, and all the state variables of the model. Also, the consistent tangent modulus is provided. Comprehensive comparison assessments are presented regarding the accuracy and stability with different numerical algorithms, strain increments, material properties, and loading conditions. The flow stress and r-value evolutions under reverse/cross-loading conditions prove that the fully implicit algorithm with a complete set of residuals is robust and accurate, even with large strain increments. By contrast, the cutting-plane method and partially-implicit Euler backward method, which are characterized by a reduced number of residuals, result in unstable responses under abrupt

loading path changes. Furthermore, as an alternative method for calculating complex first and second derivatives of the model, algorithms with analytical and numerical derivatives were studied. The developed algorithms are implemented into the finite element modeling of a large-size S-rail forming and springback. The fully implicit algorithm performs well for the whole simulation with the solely static implicit scheme. Finally, as an application of the HAH model with multi-component evolution laws, the strengths prediction of the steel plate after bending and reverse bending (BRB) deformation was conducted. The BRB test was designed to mimic the common pipe manufacturing process in a practical manner. The predicted directional strengths agree well when the HAH model is employed. By contrast, the classical isotropic hardening and iso-kinematic hardening model over- and under-estimate the strengths. The improved accuracy of the strength prediction with the investigated HAH is attributed to the anisotropic identification of the flow behavior under both load reversal and cross-loading conditions, whereas the isotropic-kinematic hardening only considers the flow behavior at load reversal.

Keywords: Anisotropic hardening; Cross-loading; Fully implicit stress update algorithm; Strength prediction; Pipe forming

Student number: 2018-39490

Contents

List of Tables

List of Figures

analysis: (a) 5% compression along RD followed by (b) 10% tension along RD, (c) 5% compression along RD followed by (d) 10% tension along 54° to RD. The dashed line and the solid line represent before deformation and after deformation, respectively.

Figure. 3.4. Stress-equivalent plastic strain curve and evolution of the HAH yield surface for MAT 1: (a) flow stress curve and (b) HAH yield locus for C5T10R.

Figure. 3.5. Stress-equivalent plastic strain curve and evolution of e-HAH yield surface for MAT 1: (a) flow stress curve and (b) HAH yield locus for C5T10CR.

Figure. 3.6. Stress-equivalent plastic strain curve and evolution of e-HAH yield surface for MAT 2: (a) flow stress curve and (b) HAH yield locus for C5T10R.

Figure. 3.7. Stress-equivalent plastic strain curve and evolution of e-HAH yield surface for MAT 2: (a) flow stress curve and (b) HAH yield locus for C5T10CR.

Figure. 3.8. The evolution of the flow stresses and r-values of MAT 1 under C5T10R path for different stress integration algorithms with strain increments:

(a),(b) $\Delta\varepsilon_{xx} = 5\times10^{-3}$, (c), (d) $\Delta\varepsilon_{xx} = 5\times10^{-4}$, and (e), (f) $\Delta\varepsilon_{xx} = 5\times10^{-6}$.

Figure. 3.9. The evolution of the flow stresses and r-values of MAT 2 under C5T10R path for different stress integration algorithms with strain increments: (a),(b) $\Delta\varepsilon_{xx} = 5\times10^{-3}$, (c), (d) $\Delta\varepsilon_{xx} = 5\times10^{-4}$, and (e), (f) $\Delta\varepsilon_{xx} = 5\times10^{-6}$.

Figure. 3.10. Evolutions of the state variables g_1 for different stress integration algorithms with strain increment $\Delta\varepsilon_{xx} = 5\times10^{-3}$: (a) MAT 1and (b) MAT 2.

Figure. 3.11. The evolution of the flow stresses and r-values of MAT 1 under C5T10CR path for different stress integration algorithms with strain increments: (a),(b) $\Delta\varepsilon_{xx} = 5\times10^{-3}$, (c), (d) $\Delta\varepsilon_{xx} = 5\times10^{-4}$, and (e), (f) $\Delta\varepsilon_{xx} = 5\times10^{-6}$

Figure. 3.12. The evolution of the flow stresses and r-values of MAT 2 under the C5T10CR path for different stress integration algorithms with strain increments: (a),(b) $\Delta\varepsilon_{xx} = 5\times10^{-3}$, (c), (d) $\Delta\varepsilon_{xx} = 5\times10^{-4}$, and (e), (f) $\Delta\varepsilon_{xx} = 5\times10^{-6}$.

Figure 3.13. The evolutions of (a) g_1, (b) g_2 for different numerical algorithms under the C5T10CR loading path. The strain increment is $\Delta\varepsilon_{xx} = 5\times10^{-3}$.

Figure 4.22. (a) Identified true stress-strain curve implemented in the finite element model, the resultant (apparent) stress-strain curve, and experimental data. (b) Magnified (predicted) flow curve in the inhomogeneous deformation region. (c) Evolution of inhomogeneous deformation during yield point phenomenon. The color code denotes the equivalent plastic strain.

Figure 4.23. Comparison of predicted engineering stress-strain curves after BRB loading. The FE predicted curves are compared between the perfect plastic and linear softening model at the yield point elongation region: (a) 0°, (b) 45°, and (c) 90° tensile curves.

1. Introduction

1.1. Anisotropic strengths of the API steel pipe

API steel pipe is the most efficient means of transporting crude oil. API steel pipes are exposed to various working environments such as deserts, polar regions, and the undersea. The pipes should satisfy the required mechanical properties according to the working environments. Therefore, the selection of the optimum material is one of the key factors in obtaining reliable mechanical properties of pipes after their formation. The required mechanical properties of manufactured pipes include commonly reported uniaxial tensile properties such as yield strength, uniform elongation, and tensile properties. In particular, the yield strengths along the transverse and longitudinal of the pipe are critical. The yield strength in the transverse or hoop direction decides the maximum internal pressure that the pipe can hold. The yield strength in the longitudinal direction provides the standard required for the structural stability of the pipe during installation or under a working environment. The transverse strength of the pipe was evaluated using common tensile tests on the specimens taken out from the pipe product. That is, the part of the pipe (in a tubular shape) is taken and flattened after applying reverse bending and

unloading. The longitudinal strength of the pipe was evaluated using the tensile specimen without the flattening process. Therefore, the deformation paths involved in these processes are complex. In terms of the change in material properties with respect to the initial (as-received) state of the plate (before pipe forming), the plate material experiences multiple bending, unloading, and reverse bending before the tensile test for a strength evaluation.

1.2. Anisotropic hardening behaviors and models

Changes in the deformation path bring the intricate microstructures, leading to more complex mechanical properties. The complex mechanical responses include the Bauschinger effect and transient flow behavior under reversed loading path [1-5]. These anisotropic hardening behaviors of sheet metals have been reported to be critical factors for the springback of automotive sheet parts [6-9]. More recently, the anisotropic hardening behavior of advanced sheet metals has been further investigated under more complex loading paths than simple reverse loading. For instance, the deformation of ferritic-phased steels shows significant stress overshooting (or larger stress than the monotonic flow stress) when the loading path changes to being orthogonal to the previous loading path [10-15]. Interestingly, du-al-phase steels with mixed ferrite and martensite phases exhibit a clear softening under

the same loading path changes [15-18]. These plastic behaviors under orthogonal loading path changes are called cross-hardening and cross-softening, respectively. Experimental observations on these complex mechanical behaviors, which cannot be explained through the simple isotropic plasticity model, require the implementation of new anisotropic models in the field of metal forming and plasticity. Indeed, this complex behavior can influence the formability and springback of advanced sheet metals [9].

In the literature, a significant amount of works have proposed models for the anisotropic hardening behavior. The kinematic hardening is a representative concept, which explains the Bauschinger effect and transient flow hardening at load reversal by introducing yield surface translation during plastic deformation. The kinematic hardening models were pioneered by Prager [19] and Ziegler [20], and further extended by adding nonlinear terms [21] or by coupling with the isotropic hardening model. The series of isotropic and kinematic hardening models was well implemented into the finite element (FE) simulations for sheet metals, especially when the metals exhibit the Bauschinger effect, transient behavior, and permanent softening under reversed loading paths [22-25].

The kinematic hardening-based anisotropic hardening models were further extended by combing the distortional hardening concept to reproduce mechanical responses under rather complex loading conditions, beyond the simple loading-reverse loading path. Ortiz and Popov [26] introduced the distortion of the yield surface by controlling the size of the effective stress. Feigenbaum and Dafalias [27,28] employed the fourth-rank anisotropic tensor as a function of plastic deformation, but the fundamental basis they used remained that of the isotropic-kinematic hardening. Teodosiu and Hu [29] introduced new effective values into the yield condition related to the structure and interactions of dislocations as a major plasticity mechanism. François [30] expressed the egg-shaped yield function by de-composing the deviatoric stress into its collinear and orthogonal parts with respect to the back stress of kinematic hardening. Badreddine et al. [31] developed a non-associated elastoplastic anisotropic hardening model, which is coupled with a damage model based on François's approach [30]. Qin et al. [32] suggested a model represent the Bauschinger effect with the kinematic hardening component, while other strain-path change effects could be expressed through the distortion of the yield surface.

Besides the kinematic hardening or combined kinematic-distortional hardening, several anisotropic hardening models are solely based on the

distortional hardening approach. Some of the distortional hardening models were developed to express the yield surface evolution by using the anisotropic coefficients as a function of the plastic work or equivalent plastic strain [33-36]. However, these models don't take into account the loading path change effect. Barlat and one the of co-authors of the present study [37-39] proposed a series of anisotropic hardening models without yield surface translation, which they named the homogeneous yield function based anisotropic hardening (HAH) models. The main concept of the HAH model consists of using the distortion of the yield surface along a designated loading path, which is called a microstructure deviator, and the distortional amounts are controlled via adequately defined plastic state variables. Later, the model was extended for reproducing the latent hardening, work hardening stagnation [38], as well as cross-softening under more general loading conditions [39]. The performance of the HAH model was validated through many applications, including the springback in U-draw bending and industrial S-rail forming [40-46]. The model is also applicable to the subjects where non-linear strain path effects are important, such as the fracture behaviors of metal after pre-deformation [47-49].

1.3. Stress update algorithms

As the constitutive models of plasticity advanced, especially the hardening laws, their implementations into FE simulations have become increasingly challenging. This is mainly attributed to the advanced constitutive models having more state variables, which are non-linearly cross-related. These challenges led to more robust numerical formulations and implementations of the constitutive models, which eventually determine the accuracy and robustness of the FE simulations. Numerous numerical algorithms have been proposed to take into account the stress integration or stress update using the elastic-plasticity constitutive models. The details of the general theoretical studies on these stress-integration algorithms for nonlinear plasticity have been well documented in a book by Simo [50].

The basic principle of the stress update algorithm for the classical rate-independent elastoplastic model consists of locating the stress state on the yield surface described in the six-dimensional stress space, which is consistent with the material hardening. The hardening of the material is often represented by a uniaxial stress-plastic-strain curve as a reference stress state. Most of the stress update algorithms have been developed in the elastic-predictor and plastic-corrector schemes. For example, the closest point

projection method (CPPM) [51-53] and the cutting-plane method (CPM) [54] have been employed as popular stress integration algorithms in FE models. The CPPM is often based on the Euler backward method (EBM), and thus it is an implicit method requiring the first and second derivatives of the yield surface to satisfy both the consistency and flow rule (or normality rule). In contrast, the CPM only satisfies the consistency condition without requiring the second derivative of the yield function; thus, this approach is also referred to as a semi-explicit method.

Regarding the stress integration algorithms on the distortional hardening models, similar approaches, based on either the CPPM or CPM schemes, have been reported. Lee et al. [55] implemented the first version of the HAH model into the commercial ABAQUS software using both the CPPM and CPM approaches. This implementation was also extended to the enhanced version of the HAH model; however, in this case, only the CPM scheme was applied in combination with a sub-stepping numerical method [56]. Recently, Choi and Yoon [57] also reported the implementation of the HAH model using the Euler backward scheme, but they calculated the derivatives of the yield function using numerical finite differences. More recently, Yoon et al. [58] coupled the CPPM scheme with a line-search algorithm for an updated version of the HAH model [59] to improve the numerical efficiency. However,

the existing numerical integration schemes do not fully exploit the implicit CPPM scheme. In other words, these approaches only account for the partial number of residuals to attain the solution process of linearized equations under the Newton-Raphson method. In this sense, these methods can be regarded as a partial or semi-implicit integration algorithm based on the Euler backward scheme.

1.4. Predictions of the pipe strength in previous studies

Taking advantage of the improved accuracy of the advanced constitutive models, the strengths of pipes manufactured by various processes have been predicted. Examples of pipe forming include UOE, JCOE, spiral, and roll forming processes, which have been selectively employed in consideration of the material properties, thickness, and pipe diameter. Although the details of these processes are different, their pipe-forming technologies involve common deformation paths dominated by multiple bending and reverse bending with superimposed stretching. Therefore, most studies on the model predictions of the pipe strength have used hardening models that account for the Bauschinger effect under reversed loading conditions. The kinematic hardening law has been regarded as the most appropriate for this purpose [60–66]. The investigations on the strength predictions using the well-known

nonlinear kinematic hardening model by Chaboche or its modified models are representative examples because they enable the reproduction of the anisotropic hardening response under load reversal [60–62, 64, 65]. Alternatively, a multi-surface kinematic hardening model, such as the two-surface model, was employed by Lee et al. [63] to predict the yield strength of roll-formed ERW pipes.

However, to date, most of the previous strength prediction models [60–66] have been characterized by reverse loading tests such as tension-compression (or compression–tension) tests along the material orientation of interest. In general, the material direction has been chosen along the circumferential of the tube or pipe for practical reasons. As a result, the yield strength along the direction could be predicted well within the expected accuracy. Several studies have predicted the yield strengths of pipes along other directions. Thibaux and Van den Abeele [62] predicted the yield strength of a pipe formed 30° off the rolling direction using their analytical model. They used average anisotropic hardening parameters calculated from the collected material data found in the literature. The predicted strengths were in good agreement with the overall tendency of the yield strength change after the pipe-forming process. However, in terms of quantitative accuracy, the predictions need to be improved. More recently, Cooreman et al. [61] presented a yield strength

prediction model using the isotropic yield function and Chaboche kinematic hardening law. They predicted the yield strengths of a spiral-formed pipe along both circumferential and longitudinal directions using a finite element simulation. In their study, they simplified the spiral-forming process through four-point bending tests, and the specimens along different orientations were removed after the bending tests. Their prediction was accurate in the circumferential direction, which corresponded to the transverse of the rolling direction. However, the predicted strengths along the other directions were not satisfactory because the kinematic hardening model employed in their study overestimated the flow softening in the longitudinal direction, which was identified based on the Bauschinger behavior in the circumferential direction. Therefore, a more advanced constitutive model, which accounts for path-dependent hardening behavior in both directions, needs to be implemented for the prediction of the pipe strength with better accuracy.

1.5. Objectives and outlines

Inspired by the advances and limitations of the current modeling approach, in this study, we aim to investigate the effect of the anisotropic hardening model on the strength prediction of a pipe manufactured through a multi-bending process. Because a pipe is formed with a constant radius of

curvature, as shown in Figure. 1.1(a), the laboratory-scale analysis employs a four-point plate bending process to equivalently simulate the pipe formation, as indicated in Figure. 1.1(b). The flattening process of the plate sample taken out of the pipe was conducted to fabricate dog-bone shape specimens. This process was simulated in the laboratory by bending the bent specimen in the reverse direction, which simulated the pipe formation. Subsequently, tensile tests were conducted for three specimens along different plate orientations. In particular, the strengths along both the circumferential and longitudinal directions of the major bending axis are evaluated. For the hardening model, the enhanced version of the HAH model [39] was used to represent the distortional hardening. An isotropic and kinematic hardening (IKH) model and a pure isotropic hardening (IH) model are comparatively considered to highlight the importance of the loading path-dependent constitutive law in a finite element simulation. Special modeling is applied to improve the HAH model under a strain path change by proposing multi-component evolution laws of the Bauschinger effect and the transient hardening behavior.

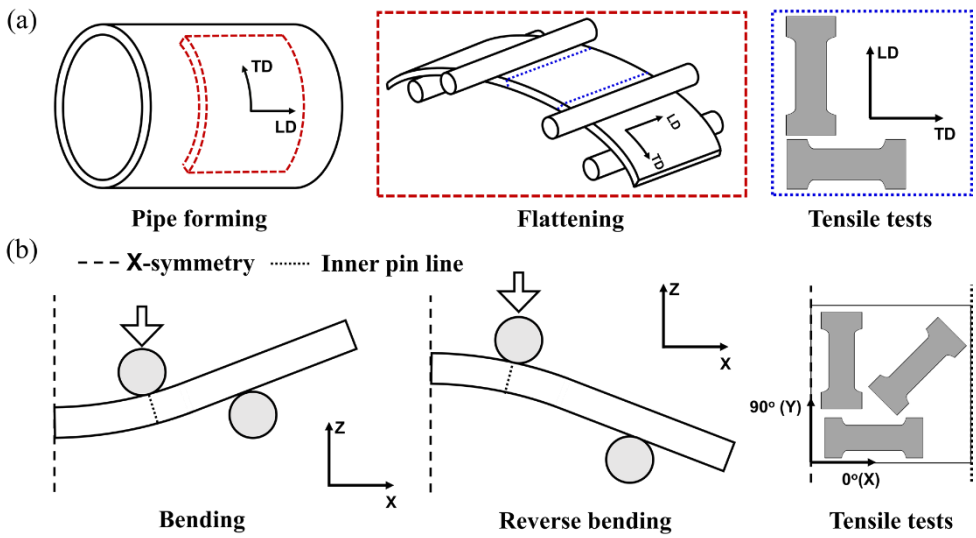

Figure. 1.1. (a) Schematic illustration of strength evaluation of a pipe along different orientations, and (b) its laboratory-scale experiment using a four-point bending test.

In Chapter 2, a summary of the investigated HAH distortional hardening model is presented with key evolution laws for the model state variables. The modified evolution rules of the state variables on the Bauschinger effect and transient hardening behavior are presented.

In Chapter 3, for the FE implementation of the HAH model, the stress integration algorithms of the HAH model were studied. The numerical integration algorithms investigated in this study are introduced, alongside a summary of previous studies. Based on the studied algorithms, the accuracy

and stability of the individual algorithms are comparatively evaluated via one-element analyses under two distinctive loading path changes. Also, an S-rail forming and springback simulation are provided as a benchmark problem to assess the validity of the proposed fully implicit numerical algorithm.

In Chapter 4, FE simulations for the anisotropic strengths prediction of steel plate after prior bending and reverse-bending are carried out using the developed fully implicit stress update algorithms in Chapter 4. The overall experimental procedures are described including the identification of used elastic-plastic constitutive models. The anisotropic strengths prediction results are provided with further discussion on the effect of hardening models and the yield point phenomenon.

It is expected that this study would be useful in investigating the mechanical properties of the plate after the pipe forming process. Note that the contents of the thesis were reconstructed from our two previous researches of H. Choi et al. (2021) [67, 68].

2. The homogeneous yield function based anisotropic hardening (HAH) model with multi-component evolution laws

2.1. Summary of the HAH hardening law

The HAH model was developed to predict the path-dependent anisotropic, non-linear evolution of plastic hardening [37–39]. The first version of the HAH model [37] could reproduce the commonly observed Bauschinger effect at load reversal, and it was further extended later to model the hardening or softening under cross-loading conditions [38, 39]. The model is based on the distortional hardening concept and does not include the commonly applied back stress tensor in the kinematic hardening laws. As a distortional hardening model, the HAH law involves a special state variable, which determines the direction of yield surface distortion at various loading path changes, and is called the microstructure deviator $\hat{\mathbf{h}}^{\mathbf{s}}$.

The yield criterion (F) defined with the HAH model is as follows:

$$F = \Phi\left(\mathbf{s},\, g_i, \hat{\mathbf{h}}^{\mathbf{s}}\right) - \bar{\sigma}\left(\bar{\varepsilon}\right) = \left(\Phi_s + \Phi_h\right)^{1/q} - \bar{\sigma}\left(\bar{\varepsilon}\right) = 0,\ \left(i = 1, 2, L, C, R\right), \qquad (2.1)$$

where Φ and $\bar{\sigma}$ are the yield surface and equivalent stress, $\mathbf{s}$ and $\hat{\mathbf{h}}^{\mathbf{s}}$ are the deviatoric and microstructure deviator tensors, and g_i and $\bar{\varepsilon}$ are the state variables and equivalent plastic strain, respectively. In this study, $\hat{\mathbf{h}}^{\mathbf{s}}$ is defined as $\hat{\mathbf{h}}^{\mathbf{s}} = \dfrac{\mathbf{h}^{\mathbf{s}}}{\sqrt{8/3\mathbf{h}^{\mathbf{s}} : \mathbf{h}^{\mathbf{s}}}}$ and the initial value of $\mathbf{h}^{\mathbf{s}}$ is set to the deviatoric stress ($\mathbf{s}$) at the beginning of the plastic deformation.

In Eq. (2.1), the yield surface is a combination of Φ_s and Φ_h, which represent the initially isotropic or anisotropic yield function and its distorting contribution along $\hat{\mathbf{h}}^{\mathbf{s}}$, respectively, and are defined as follows:

$$\Phi_s = \left\{ \phi(\tilde{\mathbf{s}})^2 + \phi(\tilde{\mathbf{s}}_p)^2 \right\}^{\frac{q}{2}}, \tag{2.2}$$

$$\Phi_h = f_1^q \left| \hat{\mathbf{h}}^{\mathbf{s}} : \mathbf{s} - \left| \hat{\mathbf{h}}^{\mathbf{s}} : \mathbf{s} \right| \right|^q + f_2^q \left| \hat{\mathbf{h}}^{\mathbf{s}} : \mathbf{s} + \left| \hat{\mathbf{h}}^{\mathbf{s}} : \mathbf{s} \right| \right|^q, \tag{2.3}$$

where q is a constant for determining the shape of the distorted yield surface. Note that Eq. (2.2) or Φ_s is initially undistorted but experiences another distortion in the orthogonal direction to the active loading direction. For this, the following equations are defined.

$$\mathbf{s}_c = \frac{8}{3}\left(\hat{\mathbf{h}}^{\mathbf{s}} : \mathbf{s} \right) \hat{\mathbf{h}}^{\mathbf{s}}, \tag{2.4}$$

$$\mathbf{s}_o = \mathbf{s} - \mathbf{s}_c = \mathbf{s} - \frac{8}{3}\left(\hat{\mathbf{h}}^{\mathbf{s}} : \mathbf{s}\right)\hat{\mathbf{h}}^{\mathbf{s}}, \tag{2.5}$$

where $\mathbf{s}_c$ and $\mathbf{s}_o$ are collinear and orthogonal to $\hat{\mathbf{h}}^{\mathbf{s}}$, respectively. Then, $\phi(\tilde{\mathbf{s}})$ and $\phi(\tilde{\mathbf{s}}_P)$ represent undistorted and orthogonally distorted functions, respectively, with the definitions of $\tilde{\mathbf{s}} = \mathbf{s}_c + \frac{1}{g_L}\mathbf{s}_o$ and $\tilde{\mathbf{s}}_P = \frac{(1-g_C)}{g_L}\mathbf{s}_o$. In addition, the variables g_L and g_C control the cross-hardening and softening of the flow stress, respectively. Note that if $g_L = g_C = 1$, Eq. (2.2) recovers its form as an isotropic yield function, or $\Phi_s = \phi(\mathbf{s})$.

Eq. (2.3) is introduced in the HAH concept for anisotropic distortion along $\hat{\mathbf{h}}^{\mathbf{s}}$, which is controlled by variables f_1 and f_2.

$$f_i = \left(g_i^{-q} - 1\right)^q, \quad i = 1, 2, \tag{2.6}$$

where the state variables g_i correspond to the ratio of the flow stress on the distorted yield surface to that in the isotropically expanding flow stress.

Figure. 2.1 shows a graphical interpretation of yield surface distortions in the π-plane when the loading is applied along $\hat{\mathbf{h}}^{\mathbf{s}}$, with two example cases of cross-hardening and softening shown in Figure. 2.2(a) and (b), respectively. Cross-hardening is defined as higher stress than monotonic stress in the

loading direction orthogonal to the current loading (see the red dashed surface in Figure. 2.2(a)). By contrast, when the flow stress in the loading direction orthogonal to the current loading is lower than that of the monotonic loading (see the blue dashed surface in Figure. 2.2(b)), it is defined as cross-softening. The normalized yield surfaces are also compared with those assumed as undergoing isotropic hardening (shown as a black solid line). The state variables used for the illustration are listed in Table 2.1.

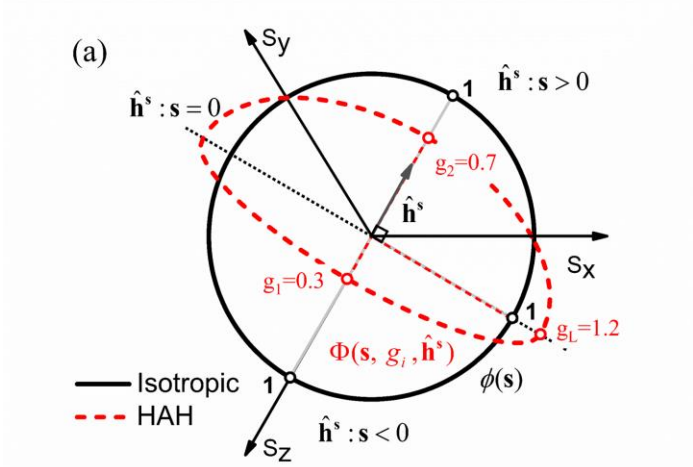

(a)

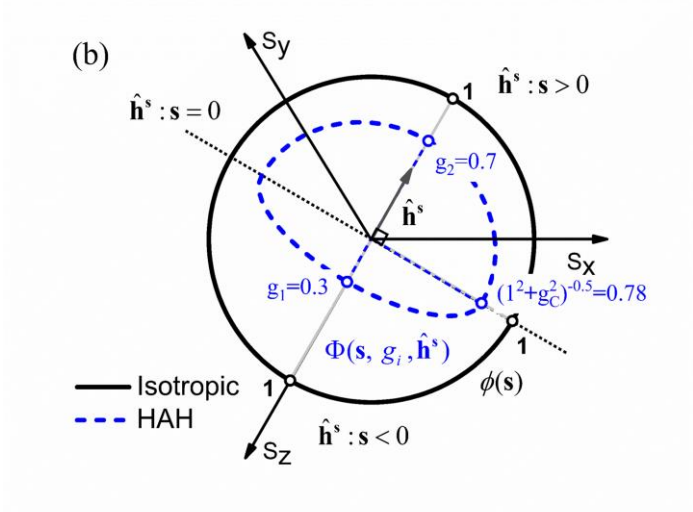

(b)

Figure. 2.1. Example HAH yield surfaces distorted under (a) cross-hardening and (b) cross-softening conditions. The black solid line represents an isotropically expanding yield surface, which is normalized by a reference tensile yield stress. The coordinates s_x, s_y, and s_z represent the π-plane.

Table 2.1. HAH state variables of the generic material used in Figure. 2.1.

	h_{11}	h_{22}	h_{33}	$h_{ij}\,(i \neq j)$	g_1	g_2	g_L	g_C
(a)	0.25	0.25	-0.5	0	0.3	0.7	1.2	1.0
(b)	0.25	0.25	-0.5	0	0.3	0.7	1.0	0.8

2.2. Evolutions of state variables for enhanced accuracy

The HAH model was developed to predict the path-dependent anisotropic, non-linear evolution of plastic hardening [37–39]. The first version of the HAH model [37] could reproduce the commonly observed Bauschinger effect at load reversal, and it was further extended later to model the hardening or softening under cross-loading conditions [38, 39]. The model is based on the distortional hardening concept and does not include the commonly applied back stress tensor in the kinematic hardening laws. As a distortional hardening model, the HAH law involves a special state variable, which determines the direction of yield surface distortion at various loading path changes, and is called the microstructure deviator $\hat{\mathbf{h}}^{\mathbf{s}}$.

State variables, $g_i\,(i = 1 \sim 4,\ L, C, R)$ and $\hat{\mathbf{h}}^{\mathbf{s}}$, are introduced to control the distortion of the yield surface. Although there are many choices of evolution

rules, in this study, they are expressed as functions of equivalent plastic strain. In the following sections, the evolution rules are described in detail by classifying them into three groups.

2.2.1. Multi-component evolution laws for load-reversal

In reversed loading, the flow stress produces the well-known Bauschinger effect, which is characterized by lower yield stress than the flow stress before loading path change, transient hardening, and permanent softening. As shown in Figure. 2.1, different state variables are associated with yield surface distortion with respect to the sign of $\hat{\mathbf{h}}^{s} : \mathbf{s}$. For example, if a current state is on the $\hat{\mathbf{h}}^{s} : \mathbf{s} > 0$ side, g_2 represents the transient behavior of the flow curve, and g_1 expresses the Bauschinger effect. The evolution laws of state variables associated with a load reversal are proposed as follows:

$$\frac{\mathrm{d}g_1}{\mathrm{d}\bar{\varepsilon}} = u_0 \cdot \frac{\mathrm{d}g_b}{\mathrm{d}\bar{\varepsilon}}\bigg|_{g_b=g_1} + \left(1-u_0\right) \cdot \frac{\mathrm{d}g_t}{\mathrm{d}\bar{\varepsilon}}\bigg|_{g_t=g_1}, \tag{2.7}$$

$$\frac{\mathrm{d}g_2}{\mathrm{d}\bar{\varepsilon}} = \left(1-u_0\right) \cdot \frac{\mathrm{d}g_b}{\mathrm{d}\bar{\varepsilon}}\bigg|_{g_b=g_2} + u_0 \cdot \frac{\mathrm{d}g_t}{\mathrm{d}\bar{\varepsilon}}\bigg|_{g_t=g_2}, \tag{2.8}$$

$$\frac{\mathrm{d}g_3}{\mathrm{d}\bar{\varepsilon}} = \left(1-u_0\right) \cdot \frac{\mathrm{d}g_s}{\mathrm{d}\bar{\varepsilon}}\bigg|_{g_s=g_3}, \tag{2.9}$$

$$\frac{\mathrm{d}g_4}{\mathrm{d}\bar{\varepsilon}} = u_0 \cdot \left.\frac{\mathrm{d}g_s}{\mathrm{d}\bar{\varepsilon}}\right|_{g_s = g_4}, \tag{2.10}$$

where $u_0 = 1$ if $\hat{\mathbf{h}}^{\mathbf{s}} : \mathbf{s} > 0$; otherwise $u_0 = 0$. The subscripts, " b ", " t ", and " s " of the state variables stand for the Bauschinger effect, transient behavior, and permanent softening, respectively. The evolution laws of the Bauschinger effect and the transient behavior are proposed as multi-component exponential functions of the equivalent plastic strain.

$$\frac{\mathrm{d}g_b}{\mathrm{d}\bar{\varepsilon}} = \sum_{j=1}^{n} \frac{\mathrm{d}g_{b,j}}{\mathrm{d}\bar{\varepsilon}} = \sum_{j=1}^{n} k_{2,j}\left(R_j k_3 - g_{b,j}\right), \tag{2.11}$$

$$\frac{\mathrm{d}g_t}{\mathrm{d}\bar{\varepsilon}} = \sum_{j=1}^{n} \frac{\mathrm{d}g_{t,j}}{\mathrm{d}\bar{\varepsilon}} = \sum_{j=1}^{n} k_{1,j}\left(R_j g_s - g_{t,j}\right), \tag{2.12}$$

$$\frac{\mathrm{d}g_s}{\mathrm{d}\bar{\varepsilon}} = k_5\left(k_4 - g_s\right), \tag{2.13}$$

where R_j is a parameter satisfying $\sum_{j=1}^{n} R_j = 1$. The suggested evolution laws converge the state variables to constants controlled with k_3 and k_4. The convergence rates are related to the constants $k_{2,j}$, $k_{1,j}$, and k_5. If $g_1 = g_2 = g_3 = g_4 = 1$, the model recovers isotropic hardening.

In the following illustration, the effectiveness of the multi-component evolution rule is presented by estimating the tension-compression-tension

flow curve obtained for the investigated material of the present study. As Figure 2.2. shows the material exhibits considerable Bauschinger effect and transient hardening. Also, the flow curves in the second tensile loading converge to the monotonic loading at large strain. Three sets of HAH hardening parameters are evaluated; one-component rule (n=1) in Eq. (2.11)-(2.12), two-component rule (n=2), and one-component without permanent softening parameter ($k_4 = 1$, $k_5 = 0$). Additionally, the isotropic hardening results were compared. All the parameters were determined by the Nelder-Mead simplex optimization. In Figure. 2.2(b), all curves predicted by different sets of evolution rules are compared. Both one- and two-component models could predict the reverse tensile curve with reasonable accuracy when a small amount of permanent softening is accounted for. However, the result indicates that the two-component evolution rule could more flexibly capture the smooth transient behavior from elastic to plastic region, and the gradually approaching flow stress toward the monotonic curve. The one-component rule without the permanent softening parameter significantly overestimated the flow curve at the second tensile loading. Considering this preliminary evaluation, the two-component model (n=2 in Eq. (2.11) and (2.12)) were used for all simulations with the HAH model in this study.

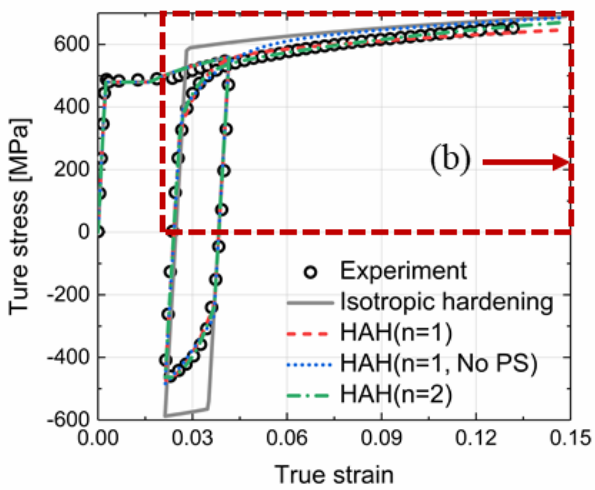

(a)

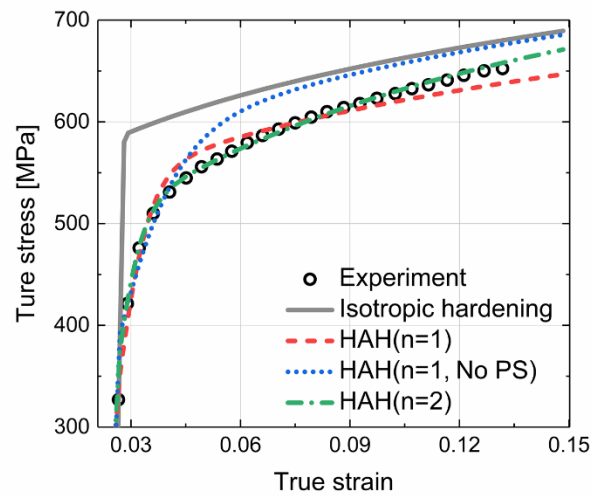

(b)

Figure. 2.2. (a) Tension-compression-tension curves calculated by HAH model with one-, two-component, and one-component without permanent softening (PS) parameters, and (b) the closed-up view during the second tension stage.

2.2.2. Latent hardening and contraction under cross-loadings

The loading path change is identified using a single scalar parameter, $\cos\chi$, as follows [38, 39]:

$$\frac{\mathrm{d}g_s}{\mathrm{d}\bar{\varepsilon}} = k_5\left(k_4 - g_s\right), \tag{2.14}$$

where $\hat{\mathbf{s}}$ is a normalized deviatoric stress tensor such as normalized $\mathbf{h}^{\mathbf{s}}$ in Eq. (2.1). Similar to the rule proposed in a previous study [39], the evolutions of cross-hardening and cross-softening are defined as follows:

$$\frac{\mathrm{d}g_L}{\mathrm{d}\bar{\varepsilon}} = k_L\left\{\frac{\bar{\sigma}\left(\bar{\varepsilon}\right)-\bar{\sigma}\left(0\right)}{\bar{\sigma}\left(\bar{\varepsilon}\right)}\left(\sqrt{L\left(1-\cos^2\chi\right)+\cos^2\chi}-1\right)+1-g_L\right\}, \tag{2.15}$$

$$\frac{\mathrm{d}g_C}{\mathrm{d}\bar{\varepsilon}} = k_C\left\{1+\left(C-1\right)\cdot\cos^2\chi - g_C\right\}, \tag{2.16}$$

where k_L, L, k_C, and C are constant parameters introduced for controlling the cross-hardening and softening, respectively. As shown in Eq. (2.16), cross-hardening does not occur if no loading path changes, or $\cos\chi = 1$. By contrast, cross-softening always occurs with plastic deformation and evolves under a cross-loading condition, or $\cos\chi = 0$. Note that if $L = C = 1$, there are no cross-loading effects.

2.2.3. Evolutions of the microstructure deviator

The microstructure deviator $\hat{\mathbf{h}}^{\mathbf{s}}$ determines the directions of the distortion under various loading path changes. The rotation or evolution of the microstructure deviator is defined as a function of the equivalent plastic strain as follows:

$$\frac{\mathrm{d}\hat{\mathbf{h}}^{\mathbf{s}}}{\mathrm{d}\bar{\varepsilon}} = \left(2\mathrm{u}_0 - 1\right) \cdot k \cdot \left\{ \left| \cos\chi \right|^{1/z} + g_R \right\} \left\{ \hat{\mathbf{s}} - \cos\chi \, \hat{\mathbf{h}}^{\mathbf{s}} \right\}, \tag{2.17}$$

where g_R is introduced to trigger an initial rotation of $\hat{\mathbf{h}}^{\mathbf{s}}$ under the cross-loading path. In addition, k and z are the model constants for g_R evolution. It evolves as

$$\frac{\mathrm{d}g_R}{\mathrm{d}\bar{\varepsilon}} = k_R \cdot \left\{ k_R^{'} \left(1 - \cos^2\chi\right) - g_R \right\}. \tag{2.18}$$

Here, k_R and $k_R^{'}$ are material constants, which are 5, 15, and 0.2, respectively, in this study. If $\cos\chi \geq 0$, $\hat{\mathbf{h}}^{\mathbf{s}}$ rotates toward the $\hat{\mathbf{s}}$ direction, but rotates toward the $-\hat{\mathbf{s}}$ direction if $\cos\chi < 0$. A more complete description of the evolution rules of the state variables can be found in [37–39].

3. Stress integration algorithms of HAH model

3.1. Motivation and general statement

The HAH model is featured with more number of plastic state variables than conventional isotropic hardening. Note that the only state variable in the von Mises isotropic model is the equivalent plastic strain. This increased number of state variables is inevitable for efficient modeling of path-dependent anisotropic hardening, while the overall numerical procedure becomes complex. The stress and microstructure deviator tensors and 8 plastic state variables ($\bar{\varepsilon}$ and $g_i \left(i = 1 \sim 4, L, C, R\right)$) are associated with the numerical stress integration of the HAH model. Therefore, a total of 20 unknowns (6 for stress tensor, 6 for microstructure deviator, and 8 state variables) are required to be solved by a stress integration algorithm for continuum elements. For the shell element under the plane stress assumption, the number of unknowns is reduced to 14. Moreover, the state variables are cross-related since the investigated distortional yield surface evolves as a function of the equivalent plastic strain. Therefore, if all the state variables are treated as independent, a total of 20 (or 14) nonlinear equations should be simultaneously solved for continuum (or shell) elements. However, if only

parts of the state variables are assumed as independent, the exact evolution of dependent variables should be included in the residuals of the independent variables. For the HAH model, this is not an easy task because the evolution laws cannot be expressed explicitly as functions of other independent variables. An additional iterative process is required to determine the state variables in the stress update algorithms in this case [55].

Another challenge in the computational modeling of HAH plasticity is the continuous, anisotropic distortions of yield surface during plastic deformation. The distortional characteristics may lead to abrupt changes in the first and/or second gradients of yield function, which are also complex functions of plastic deformation. The gradients are key factors in the flow rule of elastic-plasticity theory, and the accurate numerical integration algorithm implemented in the Euler backward scheme is essential for robust finite element simulations. Due to the difficulty, previous studies employed numerically calculated derivatives based on the finite difference method [57,58,69].

Motivated from the above issues in the finite element modeling for the distortional HAH model, in-depth comparative studies on the stress integration algorithms are tried in this study. For this purpose, numerical

investigations on two common algorithms are considered: the cutting plane method (CPM) and Euler backward method (EBM). Only plane stress condition is studied, but the overall approach can be directly extended to the general stress state. Moreover, the EBM algorithm is formulated with different numbers of residuals for updating state variables: EBM with 4 residuals (EBM-4R), and EBM with 14 residuals (EBM-14R) for the plane stress condition. The EBM-4R includes residuals for 3 stress components and an equivalent plastic strain, while the EBM-14R has additional 10 residuals for 3 microstructure deviator components and the 7 state variables on the yield function distortions. Then, to study the effect of the algorithm for calculating the derivatives of evolving yield surface, two different methods for updating the yield surface gradients are considered for the EBM-14R algorithm: analytically derived derivatives (EBM-14R/AD), and numerical derivatives based on the finite-difference (EBM-14R/ND). Note that only analytical derivatives are used for the EBM-4R algorithm. In summary, a total of 4 different stress integration algorithms are comparatively studied in the present studies; i.e., CPM, EBM-4R, EBM-14R/AD, EBM-14R/ND. In Figure. 3.1., the schematic interpretations of the 4 stress integration algorithms are presented. It is seen in Figure. 3.1(c) that the normal directions to the yield surface are not identical between the EBM algorithms with analytical and

numerical derivatives, which is resulted from the truncation error that occurred from the finite difference used for the numerical derivatives. The detailed derivations for the analytical and numerical derivatives of the HAH model are presented in Appendix A and B.

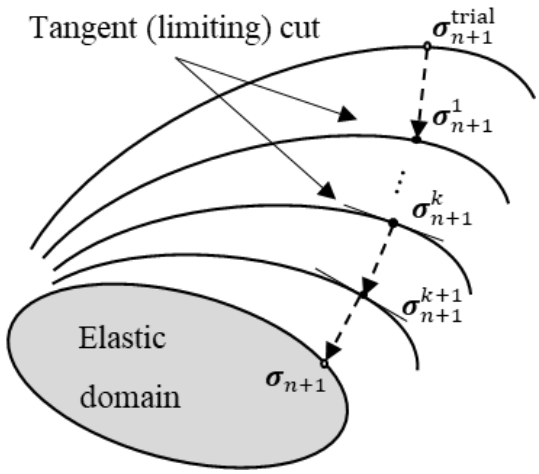

(a)

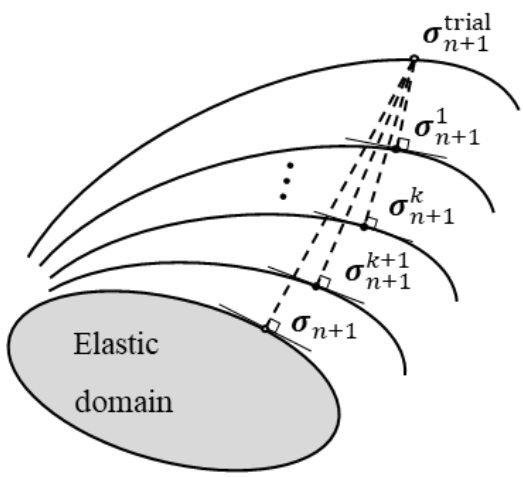

(b)

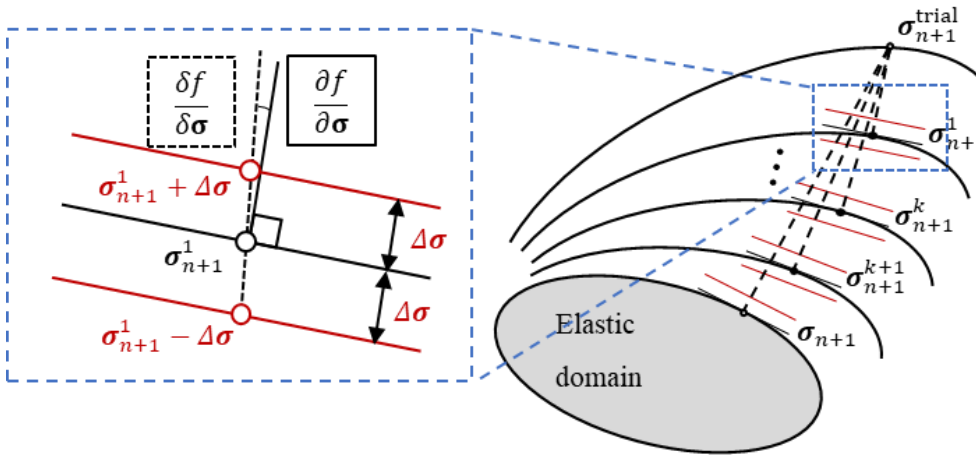

(c)

Figure 3.1. The geometrical interpretations of the implemented algorithms: (a) Cutting-plane method (CPM) (b) Euler backward method using analytical derivatives (EBM-AD) (c) Euler backward method using finite difference method (EBM-ND).

3.2. Stress update algorithms for elastic-plasticity

A In the implementation of small strain elastic-plasticity, the total strain increment, $\Delta\boldsymbol{\varepsilon}$ is additively decomposed into its elastic component, $\Delta\boldsymbol{\varepsilon}^{e}$ and plastic component, $\Delta\boldsymbol{\varepsilon}^{p}$.

$$\Delta\boldsymbol{\varepsilon} = \Delta\boldsymbol{\varepsilon}^{e} + \Delta\boldsymbol{\varepsilon}^{p}. \tag{3.1}$$

If the associated flow rule is applied, $\Delta\boldsymbol{\varepsilon}^{p}$ is calculated with the gradient

of yield function, Φ and a scalar multiplier, $\Delta\gamma$.

$$\Delta\boldsymbol{\varepsilon}^{\mathrm{p}} = \Delta\gamma \frac{\partial \Phi}{\partial \boldsymbol{\sigma}}. \tag{3.2}$$

The stress increment, $\Delta\boldsymbol{\sigma}$ is written as following for the isotropic linear elastic metals.

$$\Delta\boldsymbol{\sigma} = \mathbf{C} : \left(\Delta\boldsymbol{\varepsilon} - \Delta\boldsymbol{\varepsilon}^{\mathrm{p}}\right) = \mathbf{C} : \left(\Delta\boldsymbol{\varepsilon} - \Delta\gamma \frac{\partial \Phi}{\partial \boldsymbol{\sigma}}\right), \tag{3.3}$$

where $\mathbf{C}$ is the fourth-order elastic stiffness matrix. The relation between plastic multiplier, $\Delta\gamma$ and equivalent plastic strain increment, $\Delta\bar{\varepsilon}$ is obtained from the 1st order homogeneous function and the plastic work equivalence principle.

$$\Delta\bar{\varepsilon} = \frac{\boldsymbol{\sigma} : \Delta\boldsymbol{\varepsilon}^{\mathrm{p}}}{\Phi} = \frac{\boldsymbol{\sigma} : \Delta\gamma \dfrac{\partial \Phi}{\partial \boldsymbol{\sigma}}}{\Phi} = \Delta\gamma. \tag{3.4}$$

Therefore, it is noted that the stress integration in Eq. (3.3) is to update the equivalent plastic strain increment Eq. (3.4). Depending on the algorithmic treatment in the above general procedure, there have been various algorithmic procedures for numerically accurate and efficient integration methods.

In general, for most constitutive laws and their corresponding numerical implementations, the following predictor-corrector algorithm has been

employed.

$$\boldsymbol{\sigma}_{n+1}^{Trial} = \boldsymbol{\sigma}_n + \mathbf{C} : \Delta\boldsymbol{\varepsilon}_{n+1}, \tag{3.5}$$

$$R = \Phi\left(\boldsymbol{\sigma}_{n+1}^{Trial}, g_{i,n}, \hat{\mathbf{h}}_n^s\right) - \bar{\sigma}\left(\bar{\varepsilon}_n\right) < 0, \quad \left(i = 1 \sim 4, L, C, R\right), \tag{3.6}$$

where $\Delta\boldsymbol{\varepsilon}_{n+1}$ is the total strain increment at the current time step n+1, and $\boldsymbol{\sigma}_{n+1}^{Trial}$ is the trial stress as a predictor. The numerical algorithm begins to check the condition in Eq. (3.6) as an elastic process, while an iterative process is followed if the condition in Eq. (3.6) is not satisfied. Note that Eq. (3.6) is simplified to represent the yield function Φ as a function of state variables in the HAH model.

In the next sub-sections, existing numerical algorithms for the stress integration of the HAH model are first introduced, followed by the algorithmic development of the proposed modeling in the present work.

3.3. Stress integration algorithms for the HAH: a review of existing algorithms

3.3.1. Cutting-plane method (CPM)

Lee et al. presented the first numerical algorithm for the original HAH model [37, 55] and the enhanced version of the HAH model [56] based on the cutting-plane method (CPM). In their CPM approach, the only independent variable is the equivalent plastic strain, $\bar{\varepsilon}$. For each iteration of the current time step n+1, $\delta\Delta\bar{\varepsilon}_{n+1}^{(k+1)}$ is calculated from Eq. (3.2) –(3.4) using the linearized Eq. (3.6).

$$R_{n+1}^{(k)} + \left(\frac{\partial R}{\partial \Delta\bar{\varepsilon}}\right)_{n+1}^{(k)} \delta\left(\Delta\bar{\varepsilon}_{n+1}^{(k+1)}\right) = 0 \ , \tag{3.7}$$

$$\left(\frac{\partial R}{\partial \Delta\bar{\varepsilon}}\right)_{n+1}^{(k)} = \left(\frac{\partial \Phi}{\partial \boldsymbol{\sigma}} : \frac{\partial \boldsymbol{\sigma}}{\partial \Delta\bar{\varepsilon}}\right)_{n+1}^{(k)} - \left(\frac{\partial \bar{\sigma}}{\partial \Delta\bar{\varepsilon}}\right)_{n+1}^{(k)}, \tag{3.8}$$

$$\left(\frac{\partial \boldsymbol{\sigma}}{\partial \Delta\bar{\varepsilon}}\right)_{n+1}^{(k)} = -\mathbf{C} : \left(\frac{\partial \Phi}{\partial \boldsymbol{\sigma}}\right)_{n+1}^{(k)}, \tag{3.9}$$

$$\delta\left(\Delta\bar{\varepsilon}\right)_{n+1}^{(k+1)} = \frac{R_{n+1}^{(k)}}{\left(\frac{\partial \Phi}{\partial \boldsymbol{\sigma}} : \mathbf{C} : \frac{\partial \Phi}{\partial \boldsymbol{\sigma}}\right)_{n+1}^{(k)} + \left(\frac{\partial \bar{\sigma}}{\partial \Delta\bar{\varepsilon}}\right)_{n+1}^{(k)}}, \tag{3.10}$$

Then, the state variables and stress tensor for k+1 iteration can be explicitly

updated using the value in Eq. (3.10) as follows.

$$\Delta\bar{\varepsilon}_{n+1}^{(k+1)} = \Delta\bar{\varepsilon}_{n+1}^{(k)} + \delta\left(\Delta\bar{\varepsilon}_{n+1}^{(k+1)}\right), \tag{3.11}$$

$$g_{i,n+1}^{(k+1)} = g_{i,n+1}^{(k)} + \delta\left(g_{i,n+1}\right)^{(k)} = g_{i,n+1}^{(k)} + \left(\frac{dg_{i,n+1}}{d\bar{\varepsilon}}\right)^{(k)} \cdot \delta\left(\Delta\bar{\varepsilon}_{n+1}\right)^{(k+1)}, \quad \left(i = 1 \sim 4, L, C, R\right), \tag{3.12}$$

$$\hat{\mathbf{h}}_{n+1}^{s(k+1)} = \hat{\mathbf{h}}_{n+1}^{s(k)} + \delta\left(\hat{\mathbf{h}}_{n+1}^{s}\right)^{(k)} = \hat{\mathbf{h}}_{n+1}^{s(k)} + \left(\frac{d\hat{\mathbf{h}}_{n+1}^{s}}{d\bar{\varepsilon}}\right)^{(k)} \cdot \delta\left(\Delta\bar{\varepsilon}_{n+1}\right)^{(k+1)}, \tag{3.13}$$

$$\Delta\boldsymbol{\sigma}_{n+1}^{(k+1)} = \mathbf{C} : \left(\Delta\boldsymbol{\varepsilon}_{n+1} - \Delta\bar{\varepsilon}_{n+1}^{(k+1)}\right), \tag{3.14}$$

The iterative procedure continues until the following condition is satisfied.

$$\Phi\left(\boldsymbol{\sigma}_{n+1}^{(k+1)}, g_{i,n+1}^{(k+1)}, \hat{\mathbf{h}}_{n+1}^{s(k+1)}\right) - \bar{\sigma}\left(\bar{\varepsilon}_{n+1}^{(k+1)}\right) < \bar{\sigma}\left(\bar{\varepsilon}_{n}\right) \cdot \mathrm{Tol}, \quad \left(\mathrm{Tol} = 10^{-6}\right), \tag{3.15}$$

Therefore, in the CPM the only unknown variable is $\bar{\varepsilon}$ and all other variables are treated as a function of $\boldsymbol{\sigma}$. In the algorithmic aspect, this leads to the yield surface gradient (in Eq. (3.10)) expressed as a complex form.

$$\frac{\partial \Phi}{\partial \boldsymbol{\sigma}} = \Phi^{1-q}\left[\begin{array}{l}\left(\psi(\mathbf{s})+\psi(\mathbf{s}_p)\right)^{\frac{q}{2}-1}\left\{\psi(\mathbf{s})\dfrac{\partial\psi(\mathbf{s})}{\partial\boldsymbol{\sigma}}+\psi(\mathbf{s}_p)\dfrac{\partial\psi(\mathbf{s}_p)}{\partial\boldsymbol{\sigma}}\right\}\\ +\dfrac{\partial f_2}{\partial g_2}\cdot\dfrac{\partial g_2}{\partial\bar{\varepsilon}}\cdot\dfrac{\partial\bar{\varepsilon}}{\partial\boldsymbol{\sigma}}\cdot f_2^{q-1}(2\hat{\mathbf{h}}^s:\mathbf{s})^q\\ +2\cdot f_2^q\cdot(2\hat{\mathbf{h}}^s:\mathbf{s})^{q-1}\left\{\mathbf{s}:\left(\dfrac{\partial\hat{\mathbf{h}}^s}{\partial\bar{\varepsilon}}\otimes\dfrac{\partial\bar{\varepsilon}}{\partial\boldsymbol{\sigma}}\right)+\hat{\mathbf{h}}^s:\dfrac{\partial\mathbf{s}}{\partial\boldsymbol{\sigma}}\right\}\end{array}\right], \quad (3.16)$$

$\left(\text{when } \hat{\mathbf{h}}^s:\mathbf{s}>0\right)$.

Lee et al. [56] employed a Newton-Raphson procedure as an alternative to the analytical derivation of the gradient and an additional sub-stepping method was also used for numerical stability. Moreover, the further simplification of Eq. (3.16) was suggested by ignoring higher-order terms as follows.

$$\frac{\partial \Phi}{\partial \boldsymbol{\sigma}} = \Phi^{1-q}\left[\begin{array}{l}\left(\psi(\mathbf{s})+\psi(\mathbf{s}_p)\right)^{\frac{q}{2}-1}\left\{\psi(\mathbf{s})\dfrac{\partial\psi(\mathbf{s})}{\partial\boldsymbol{\sigma}}+\psi(\mathbf{s}_p)\dfrac{\partial\psi(\mathbf{s}_p)}{\partial\boldsymbol{\sigma}}\right\}\\ +2\cdot f_2^q\cdot(2\hat{\mathbf{h}}^s:\mathbf{s})^{q-1}\hat{\mathbf{h}}^s:\dfrac{\partial\mathbf{s}}{\partial\boldsymbol{\sigma}}\end{array}\right], \quad (3.17)$$

$\left(\text{when } \hat{\mathbf{h}}^s:\mathbf{s}>0\right)$.

In the implicit FE formulation, an algorithmic tangent modulus is commonly required to obtain a quadratic convergence rate. However, in the conventional CPM-based stress integration algorithm, this cannot be readily applied. For example, an additional numerical technique was proposed for the tangent moduli to preserve the quadratic convergence rate [54], but not for

the distortional hardening models. For the CPM of HAH or e-HAH in Lee et al. [55, 56], the continuum tangent modulus, $\mathbf{C}^{ep}$ was used as an alternative to the consistent tangent modulus.

$$\mathbf{C}^{ep} = \frac{d\boldsymbol{\sigma}_{n+1}}{d\boldsymbol{\varepsilon}_{n+1}} = \mathbf{C} - \left(\frac{\mathbf{C} : \frac{\partial \Phi_{n+1}}{\partial \boldsymbol{\sigma}_{n+1}} \otimes \mathbf{C} : \frac{\partial \Phi_{n+1}}{\partial \boldsymbol{\sigma}_{n+1}}}{\frac{\partial \Phi_{n+1}}{\partial \boldsymbol{\sigma}_{n+1}} : \mathbf{C} : \frac{\partial \Phi_{n+1}}{\partial \boldsymbol{\sigma}_{n+1}} + \frac{\partial \bar{\sigma}_{n+1}}{\partial \bar{\varepsilon}_{n+1}}} \right). \tag{3.18}$$

3.3.1. Euler backward method (EBM)

There are previous researches for developing the Euler backward method (EBM) based stress integration algorithm of distortional anisotropic hardening laws. However, their algorithms simplified the set of equations in the EBM algorithm by reducing the number of residuals associated with the state variables. Residuals on stress tensor and equivalent plastic strain were required to satisfy the common consistency condition in elastic-plasticity under the associated flow rule. However, this method has a similar problem as in the CPM-based algorithm [56] because parts of state variables should be functions of independent variables when the number of the residuals is less than that of independent variables in the enhanced version of the HAH model. This may cause difficulty in calculating the first and second derivatives of the yield function during its evolution as a function of plastic deformation.

The EBM algorithm developed by Lee et al. [55] introduced the following residuals.

$$\begin{aligned} &R_{1,n+1}^{(k)} = \Phi\left(\boldsymbol{\sigma}_{n+1}^{(k)},\ g_{i,n+1}^{(k)}, \hat{\mathbf{h}}_{i,n+1}^{s(k)}\right) - \bar{\sigma}\left(\bar{\varepsilon}_{n+1}^{(k)}\right), \\ &\left(i = 1-7,\ 5 = L,\ 6 = C,\ 7 = R\right), \end{aligned} \tag{3.19}$$

$$\mathbf{R}_{2,n+1}^{(k)} = -\Delta\boldsymbol{\varepsilon}_{n+1}^{p(k)} + \Delta\gamma\,\partial_{\sigma}\Phi_{n+1}^{(k)}, \tag{3.20}$$

To apply a multi-variable Newton-Raphson method, the residuals are linearized as follows.

$$R_{1,n+1}^{(k)} - \partial_{\bar{\varepsilon}}\bar{\sigma}\left(\bar{\varepsilon}_{n+1}^{(k)}\right)\cdot\delta\left(\Delta\bar{\varepsilon}_{n+1}\right)^{(k+1)} + \partial_{\boldsymbol{\sigma}}\Phi_{n+1}^{(k)} : \delta\left(\Delta\boldsymbol{\sigma}_{n+1}\right)^{(k+1)} = 0, \tag{3.21}$$

$$\begin{aligned} &\mathbf{R}_{2,n+1}^{(k)} + \partial_{\boldsymbol{\sigma}}\Phi_{n+1}^{(k)}\cdot\delta\left(\Delta\bar{\varepsilon}_{n+1}\right)^{(k+1)} + \Xi^{-1(k)}_{n+1} : \delta\left(\Delta\boldsymbol{\sigma}_{n+1}\right)^{(k+1)} = 0. \\ &\Xi^{-1(k)}_{n+1} = \left(\mathbf{C}^{-1} + \Delta\bar{\varepsilon}_{n+1}^{(k)}\,\partial^2_{\boldsymbol{\sigma}\boldsymbol{\sigma}}\Phi_{n+1}^{(k)}\right)^{-1} \end{aligned} \tag{3.22}$$

The linearized equations can be calculated with respect to $\delta\left(\Delta\bar{\varepsilon}_{n+1}\right)^{(k)}$, $\delta\left(\Delta\boldsymbol{\sigma}_{n+1}\right)^{(k)}$ by solving the following system.

$$\begin{Bmatrix} \delta\left(\Delta\bar{\varepsilon}_{n+1}\right)^{(k+1)} \\ \delta\left(\Delta\boldsymbol{\sigma}_{n+1}\right)^{(k+1)} \end{Bmatrix} = -\begin{bmatrix} \left(\dfrac{\partial R_1}{\partial\Delta\bar{\varepsilon}}\right)^{k}_{n+1} & \left(\dfrac{\partial R_1}{\partial\Delta\boldsymbol{\sigma}}\right)^{k}_{n+1} \\ \left(\dfrac{\partial \mathbf{R}_2}{\partial\Delta\bar{\varepsilon}}\right)^{k}_{n+1} & \left(\dfrac{\partial \mathbf{R}_2}{\partial\Delta\boldsymbol{\sigma}}\right)^{k}_{n+1} \end{bmatrix}^{-1} \cdot \begin{Bmatrix} R_{1,n+1}^{(k)} \\ \mathbf{R}_{2,n+1}^{(k)} \end{Bmatrix}. \tag{3.23}$$

After converged solutions of Eq. (3.23), the other variables are updated

explicitly using Eqs. (3.11)-(3.13). The iterative process stops when the following conditions are satisfied.

$$\left\| R_{1+i,n+1}^{(k)} \right\| < \bar{\sigma}\left(\bar{\varepsilon}_n\right) \cdot \mathrm{Tol}, \quad \left\| \mathbf{R}_{2,n+1}^{(k)} \right\| < \mathrm{Tol}. \tag{3.24}$$

As aforementioned, the major difficulty in this algorithmic procedure is with the calculation of the first and second derivatives due to the anisotropically evolving yield function, and this evolution is closely associated with the multiple numbers of dependent variables in the enhanced version of HAH. To overcome this issue, Lee et al. [55] employed the multi-step Newton-Raphson method by subdividing the variables g_{1or2}. Recently, Choi and Yoon [57] also applied the multi-stage EBM algorithm by using the sub-division of strain increment, $\Delta\boldsymbol{\varepsilon}_{n+1}$, which was originally proposed by Yoon et al. [70]. Yoon et al. [58] also used a line-search method for the step size control on Eq. (3.22) as an alternative effort to increase the stability of the algorithm for the distortional hardening model.

Contrary to the CPM algorithm, the EBM-based stress integrations have quadratic convergence which is consistent with the global Newton-Raphson method. The consistent tangent modulus can be expressed as follows.

$$\mathbf{C}^{\mathrm{ep}} = \boldsymbol{\Xi}_{\mathrm{n+1}} - \left(\frac{\boldsymbol{\Xi}_{\mathrm{n+1}} : \partial_{\boldsymbol{\sigma}} \Phi_{\mathrm{n+1}} \otimes \boldsymbol{\Xi}_{\mathrm{n+1}} : \partial_{\boldsymbol{\sigma}} \Phi_{\mathrm{n+1}}}{\partial_{\boldsymbol{\sigma}} \Phi_{\mathrm{n+1}} : \boldsymbol{\Xi}_{\mathrm{n+1}} : \partial_{\boldsymbol{\sigma}} \Phi_{\mathrm{n+1}} + \partial_{\bar{\varepsilon}} \bar{\sigma}\left(\bar{\varepsilon}_{\mathrm{n+1}}\right)} \right) \tag{3.25}$$

As shown in Eq. (3.25), the tangent modulus requires the calculations of the first and second derivatives of yield function under the associated flow rule. As discussed previously, the existing EBM-based algorithms introduced simpler forms without presenting complete derivations of their analytical set.

3.4. Stress integration algorithms for the HAH: proposed algorithms

3.4.1. Cutting-plane method (CPM)

In comparison with the CPM algorithm used by Lee et al. [55], where the effect of dependent variables is included in the yield surface gradient, the present CPM introduces the linearization of yield condition, Eq. (3.6) as follows.

$$\begin{aligned} \left(\frac{\partial \mathrm{R}}{\partial \Delta \bar{\varepsilon}} \right)_{\mathrm{n+1}}^{(\mathrm{k})} &= \left(\frac{\partial \Phi}{\partial \boldsymbol{\sigma}} : \frac{\partial \boldsymbol{\sigma}}{\partial \Delta \bar{\varepsilon}} \right)_{\mathrm{n+1}}^{(\mathrm{k})} + \left(\frac{\partial \Phi}{\partial \hat{\mathbf{h}}^{\mathbf{s}}} : \frac{\partial \hat{\mathbf{h}}^{\mathbf{s}}}{\partial \Delta \bar{\varepsilon}} \right)_{\mathrm{n+1}}^{(\mathrm{k})} \\ &+ \left(\sum_{\mathrm{i}} \frac{\partial \Phi}{\partial \mathrm{g}_{\mathrm{i}}} \cdot \frac{\partial \mathrm{g}_{\mathrm{i}}}{\partial \Delta \bar{\varepsilon}} \right)_{\mathrm{n+1}}^{(\mathrm{k})} - \left(\frac{\partial \bar{\sigma}}{\partial \Delta \bar{\varepsilon}} \right)_{\mathrm{n+1}}^{(\mathrm{k})} \end{aligned}, \tag{3.26}$$

After substituting Eqs. (3.26) and (3.9) into Eq. (25), $\delta\left(\Delta\bar{\varepsilon}\right)_{\mathrm{n+1}}^{(\mathrm{k+1})}$ can be calculated.

$$\delta\left(\Delta\bar{\varepsilon}\right)_{n+1}^{(k+1)} = R_{n+1}^{(k)} \Big/ \left\{ \begin{array}{l} \left(\dfrac{\partial \Phi}{\partial \boldsymbol{\sigma}} : \mathbf{C} : \dfrac{\partial \Phi}{\partial \boldsymbol{\sigma}} \right)_{n+1}^{(k)} - \left(\dfrac{\partial \Phi}{\partial \hat{\mathbf{h}}^{s}} : \dfrac{\partial \hat{\mathbf{h}}^{s}}{\partial \Delta\bar{\varepsilon}} \right)_{n+1}^{(k)} \\ - \left(\displaystyle\sum_{i} \dfrac{\partial \Phi}{\partial g_i} \cdot \dfrac{\partial g_i}{\partial \Delta\bar{\varepsilon}} \right)_{n+1}^{(k)} + \left(\dfrac{\partial \bar{\sigma}}{\partial \Delta\bar{\varepsilon}} \right)_{n+1}^{(k)} \end{array} \right\}, \tag{3.27}$$

The state variables and the stress tensor for the $(k+1)$th iteration at the current time step are iteratively updated by using Eqs. (3.11)-(3.14) until Eq. (3.15) is satisfied. The tangent modulus $\mathbf{C}^{ep}$ is also calculated using the consistency condition

$$\begin{array}{l} dR_{n+1} = \dfrac{\partial \Phi_{n+1}}{\partial \boldsymbol{\sigma}_{n+1}} : d\boldsymbol{\sigma}_{n+1} + \dfrac{\partial \Phi_{n+1}}{\partial \hat{\mathbf{h}}_{n+1}^{s}} : \dfrac{\partial \hat{\mathbf{h}}_{n+1}^{s}}{\partial \bar{\varepsilon}_{n+1}} d\bar{\varepsilon}_{n+1} \\ + \dfrac{\partial \Phi_{n+1}}{\partial g_{i,n+1}} \cdot \dfrac{\partial g_{i,n+1}}{\partial \bar{\varepsilon}_{n+1}} d\bar{\varepsilon}_{n+1} - \dfrac{\partial \bar{\sigma}_{n+1}}{\partial \bar{\varepsilon}_{n+1}} d\bar{\varepsilon}_{n+1} = 0 \end{array}, \tag{3.28}$$

By substituting Eq. (3.3) into Eq. (3.28), the elastoplastic tangent modulus is expressed as follows.

$$\mathbf{C}^{ep} = \frac{d\boldsymbol{\sigma}_{n+1}}{d\boldsymbol{\varepsilon}_{n+1}} = \mathbf{C} - \left(\frac{\mathbf{C} : \dfrac{\partial \Phi_{n+1}}{\partial \boldsymbol{\sigma}_{n+1}} \otimes \mathbf{C} : \dfrac{\partial \Phi_{n+1}}{\partial \boldsymbol{\sigma}_{n+1}}}{\dfrac{\partial \Phi_{n+1}}{\partial \boldsymbol{\sigma}_{n+1}} : \mathbf{C} : \dfrac{\partial \Phi_{n+1}}{\partial \boldsymbol{\sigma}_{n+1}} - \dfrac{\partial \Phi_{n+1}}{\partial \hat{\mathbf{h}}_{n+1}^{s}} : \dfrac{\partial \hat{\mathbf{h}}_{n+1}^{s}}{\partial \bar{\varepsilon}_{n+1}} - \dfrac{\partial \Phi_{n+1}}{\partial g_{i,n+1}} \cdot \dfrac{\partial g_{i,n+1}}{\partial \bar{\varepsilon}_{n+1}} + \dfrac{\partial \bar{\sigma}_{n+1}}{\partial \bar{\varepsilon}_{n+1}}} \right), \tag{3.29}$$

3.4.2. Fully implicit Euler backward method (EBM)

The characteristic of the enhanced version of the HAH model is that the state variables are cross-related to each other. The complexity resulted from the constitutive model makes it difficult in constructing exact linearization of the governing equation with a limited number of independent variables. This is the reason why the previous existing algorithms were developed with their simplifying methods. In this study, our effort is focused on deriving a fully implicit EBM algorithm by simultaneously solving the whole residuals defined for stress tensor, microstructure deviator tensor, and 8 state variables (or equivalently 14 unknowns) associated with the HAH at plane stress condition. To the best knowledge of the present authors, this is the first trial for the algorithmic implementation of the distortional anisotropic hardening enhanced HAH model.

In the following, a set of nonlinear equations defining residuals of the enhanced HAH model is provided. Eq. (3.30) is from the consistency condition, Eq. (3.31) represents the associated flow rule, Eq. (3.32) is for the state variables controlling the distortion of yield surface, and Eq. (3.33) is defined for the rotation of microstructure deviator, $\hat{\mathbf{h}}^{s}$.

$$
\begin{aligned}
&R_{1,n+1}^{(k)} = \Phi\left(\boldsymbol{\sigma}_{n+1}^{(k)},\, g_{i,n+1}^{(k)}, \hat{\mathbf{h}}^{s(k)}_{i,n+1}\right) - \bar{\sigma}\left(\bar{\varepsilon}_{n+1}^{(k)}\right), \\
&\left(i = 1-7,\ 5 = L,\ 6 = C,\ 7 = R\right),
\end{aligned}
\tag{3.30}
$$

$$
\mathbf{R}_{2,n+1}^{(k)} = -\Delta\boldsymbol{\varepsilon}_{n+1}^{p(k)} + \Delta\gamma\,\partial_{\sigma}\Phi_{n+1}^{(k)}, \tag{3.31}
$$

$$
R_{2+i,n+1}^{(k)} = g_{i,n+1}^{(k)} - g_{i,n} - \left(\frac{dg_{i,n+1}}{d\bar{\varepsilon}}\right)^{(k)} \cdot \Delta\bar{\varepsilon}_{n+1}^{(k)}\ , \tag{3.32}
$$

$$
\mathbf{R}_{10,n+1}^{(k)} = \Delta\hat{\mathbf{h}}^{s(k)}_{n+1} - \Delta\hat{\mathbf{h}}^{s}_{n} - \left(\frac{d\hat{\mathbf{h}}^{s}_{n+1}}{d\bar{\varepsilon}}\right)^{(k)} \cdot \Delta\bar{\varepsilon}_{n+1}^{(k)}, \tag{3.33}
$$

Linearization of Eqs. (3.30)-(3.33) leads to the following equations.

$$
\begin{aligned}
&R_{1,n+1}^{(k)} - \partial_{\bar{\varepsilon}}\bar{\sigma}\left(\bar{\varepsilon}_{n+1}^{(k)}\right)\cdot\delta\left(\Delta\bar{\varepsilon}_{n+1}\right)^{(k+1)} + \partial_{\boldsymbol{\sigma}}\Phi_{n+1}^{(k)} : \delta\left(\Delta\boldsymbol{\sigma}_{n+1}\right)^{(k+1)} \\
&+\sum_{i}\partial_{g_i} f_{n+1}^{(k)}\cdot\left(\Delta g_{i,n+1}\right)^{(k+1)} + \partial_{\hat{\mathbf{h}}^{s}}\Phi_{n+1}^{(k)} : \delta\left(\Delta\hat{\mathbf{h}}^{s}_{n+1}\right)^{(k+1)} = 0,
\end{aligned}
\tag{3.34}
$$

$$
\begin{aligned}
&\mathbf{R}_{2,n+1}^{(k)} + \partial_{\boldsymbol{\sigma}}\Phi_{n+1}^{(k)}\cdot\delta\left(\Delta\bar{\varepsilon}_{n+1}\right)^{(k+1)} + \Xi^{-1(k)}_{n+1} : \delta\left(\Delta\boldsymbol{\sigma}_{n+1}\right)^{(k+1)} \\
&+\sum_{g_i}\partial^{2}_{\boldsymbol{\sigma} g_i}\Phi_{n+1}^{(k)}\cdot\delta\left(\Delta g_{i,n+1}\right)^{(k+1)}\cdot\Delta\bar{\varepsilon}_{n+1}^{(k)} + \partial^{2}_{\boldsymbol{\sigma}\hat{\mathbf{h}}^{s}}\Phi_{n+1}^{(k)} : \delta\left(\Delta\hat{\mathbf{h}}^{s}_{n+1}\right)^{(k)}\cdot\Delta\bar{\varepsilon}_{n+1}^{(k+1)} = 0 \\
&\Xi^{-1(k)}_{n+1} = \left(\mathbf{C}^{-1} + \Delta\bar{\varepsilon}_{n+1}^{(k)}\,\partial^{2}_{\boldsymbol{\sigma}\boldsymbol{\sigma}}\Phi_{n+1}^{(k)}\right)^{-1}
\end{aligned}
\tag{3.35}
$$

$$
\begin{aligned}
&R^{(k)}_{2+i,n+1} - \left(\frac{dg_{i,n+1}}{d\bar{\varepsilon}} \right) \cdot \delta\left(\Delta\bar{\varepsilon}_{n+1} \right)^{(k+1)} \\
&-\partial_{\boldsymbol{\sigma}} \left(\frac{dg_{i,n+1}}{d\bar{\varepsilon}} \right) \cdot \delta\left(\Delta\boldsymbol{\sigma}_{n+1} \right)^{(k+1)} \cdot \Delta\bar{\varepsilon}^{(k)}_{n+1} \\
&-\partial_{g_i} \left(\frac{dg_{i,n+1}}{d\bar{\varepsilon}} \right) \cdot \delta\left(\Delta g_{i,n+1} \right)^{(k+1)} \cdot \Delta\bar{\varepsilon}^{(k)}_{n+1} \\
&-\partial_{\hat{\mathbf{h}}^{s}} \left(\frac{dg_{i,n+1}}{d\bar{\varepsilon}} \right) \cdot \delta\left(\Delta\hat{\mathbf{h}}^{s}_{n+1} \right)^{(k+1)} \cdot \Delta\bar{\varepsilon}^{(k)}_{n+1} = 0
\end{aligned}
, \tag{3.36}
$$

$$
\begin{aligned}
&\mathbf{R}^{(k)}_{10,n+1} + \Delta\hat{\mathbf{h}}^{s(k)}_{n+1} - \left(\frac{d\hat{\mathbf{h}}^{s}_{n+1}}{d\bar{\varepsilon}} \right)^{(k)} \cdot \delta\left(\Delta\bar{\varepsilon}_{n+1} \right)^{(k+1)} \\
&-\partial_{\boldsymbol{\sigma}} \left(\frac{d\hat{\mathbf{h}}^{s}_{n+1}}{d\bar{\varepsilon}} \right)^{(k)} : \delta\left(\Delta\boldsymbol{\sigma}_{n+1} \right)^{(k+1)} \cdot \Delta\bar{\varepsilon}^{(k)}_{n+1} \\
&-\partial_{g_i} \left(\frac{d\hat{\mathbf{h}}^{s}_{n+1}}{d\bar{\varepsilon}} \right)^{(k)} \cdot \delta\left(\Delta g_{i,n+1} \right)^{(k+1)} \cdot \Delta\bar{\varepsilon}^{(k)}_{n+1} \\
&-\partial_{\hat{\mathbf{h}}^{s}} \left(\frac{d\hat{\mathbf{h}}^{s}_{n+1}}{d\bar{\varepsilon}} \right)^{(k)} : \delta\left(\Delta\hat{\mathbf{h}}^{s}_{n+1} \right)^{(k+1)} \cdot \Delta\bar{\varepsilon}^{(k)}_{n+1} = 0
\end{aligned}
, \tag{3.37}
$$

Then, the solutions of the above-linearized equations are obtained for $\delta\left(\Delta\bar{\varepsilon}_{n+1} \right)^{(k+1)}$, $\delta\left(\Delta\boldsymbol{\sigma}_{n+1} \right)^{(k+1)}$, $\delta\left(\Delta g_{i,n+1} \right)^{(k+1)}$ and $\delta\left(\Delta\hat{\mathbf{h}}^{s}_{n+1} \right)^{(k+1)}$ by solving the following matrix equations.

$$\begin{Bmatrix} \delta\left(\Delta\bar{\varepsilon}_{n+1}\right)^{(k+1)} \\ \delta\left(\Delta\boldsymbol{\sigma}_{n+1}\right)^{(k+1)} \\ \delta\left(\Delta g_{i,n+1}\right)^{(k+1)} \\ \delta\left(\Delta\hat{\mathbf{h}}^{s}_{n+1}\right)^{(k+1)} \end{Bmatrix} = -\mathbf{J}^{-1}\cdot\begin{Bmatrix} R^{(k)}_{1,n+1} \\ \mathbf{R}^{(k)}_{2,n+1} \\ R^{(k)}_{2+i,n+1} \\ \mathbf{R}^{(k)}_{10,n+1} \end{Bmatrix}$$

$$\mathbf{J} = \begin{bmatrix} \left(\frac{\partial R_1}{\partial\Delta\bar{\varepsilon}}\right)^{k}_{n+1} & \left(\frac{\partial R_1}{\partial\Delta\boldsymbol{\sigma}}\right)^{k}_{n+1} & \left(\frac{\partial R_1}{\partial\Delta g_i}\right)^{k}_{n+1} & \left(\frac{\partial R_1}{\partial\Delta\hat{\mathbf{h}}^{s}}\right)^{k}_{n+1} \\ \left(\frac{\partial \mathbf{R}_2}{\partial\Delta\bar{\varepsilon}}\right)^{k}_{n+1} & \left(\frac{\partial \mathbf{R}_2}{\partial\Delta\boldsymbol{\sigma}}\right)^{k}_{n+1} & \left(\frac{\partial \mathbf{R}_2}{\partial\Delta g_i}\right)^{k}_{n+1} & \left(\frac{\partial \mathbf{R}_2}{\partial\Delta\hat{\mathbf{h}}^{s}}\right)^{k}_{n+1} \\ \left(\frac{\partial R_{2+i}}{\partial\Delta\bar{\varepsilon}}\right)^{k}_{n+1} & \left(\frac{\partial R_{2+i}}{\partial\Delta\boldsymbol{\sigma}}\right)^{k}_{n+1} & \left(\frac{\partial R_{2+i}}{\partial\Delta g_i}\right)^{k}_{n+1} & \left(\frac{\partial R_{2+i}}{\partial\Delta\hat{\mathbf{h}}^{s}}\right)^{k}_{n+1} \\ \left(\frac{\partial \mathbf{R}_{10}}{\partial\Delta\bar{\varepsilon}}\right)^{k}_{n+1} & \left(\frac{\partial \mathbf{R}_{10}}{\partial\Delta\boldsymbol{\sigma}}\right)^{k}_{n+1} & \left(\frac{\partial \mathbf{R}_{10}}{\partial\Delta g_i}\right)^{k}_{n+1} & \left(\frac{\partial \mathbf{R}_{10}}{\partial\Delta\hat{\mathbf{h}}^{s}}\right)^{k}_{n+1} \end{bmatrix}, \tag{3.38}$$

Eq. (3.38) shows that the Jacobian matrix has a size of 14 by 14 when it is expressed as the Voigt notation under the plane stress condition. By applying Newton's method, all state variables are updated for $(k+1)$th iteration and it continues until the residuals satisfy the following criteria.

$$\begin{aligned} &\left\|R^{(k)}_{1+i,n+1}\right\| < \bar{\sigma}\left(\bar{\varepsilon}_n\right)\cdot \mathrm{Tol},\ \left\|\mathbf{R}^{(k)}_{2,n+1}\right\| < \left\|\Delta\boldsymbol{\varepsilon}_{n+1}\right\|\cdot \mathrm{Tol}, \\ &\left\|R^{(k)}_{2+i,n+1}\right\| < \mathrm{Tol},\ \textit{and}\ \left\|\mathbf{R}^{(k)}_{10,n+1}\right\| < H^{-\frac{1}{2}}\cdot \mathrm{Tol} \end{aligned}, \tag{3.39}$$

In this study, tolerance, Tol is set to be 10^{-6} for all residuals with proper normalizations.

The linearized flow rule, Eq. (3.3) and isotropic linear elasticity, Eq. (3.2)

lead to the calculation of consistent tangent modulus $\mathbf{C}^{\mathrm{ep}}$ for the EBM of the enhanced HAH model as follows.

$$\mathrm{d}\boldsymbol{\sigma}_{\mathrm{n+1}} = \mathbf{C} : \left(\mathrm{d}\boldsymbol{\varepsilon}_{\mathrm{n+1}} - \mathrm{d}\boldsymbol{\varepsilon}^{p}_{\mathrm{n+1}} \right), \tag{3.40}$$

$$\begin{aligned} \mathrm{d}\boldsymbol{\varepsilon}^{p}_{\mathrm{n+1}} &= \mathrm{d}\Delta\bar{\varepsilon}_{\mathrm{n+1}} \cdot \partial_{\boldsymbol{\sigma}} \Phi_{\mathrm{n+1}} + \Delta\bar{\varepsilon}_{\mathrm{n+1}} \cdot \partial^{2}_{\boldsymbol{\sigma}\boldsymbol{\sigma}} \Phi_{\mathrm{n+1}} : \mathrm{d}\boldsymbol{\sigma}_{\mathrm{n+1}} \\ &+ \Delta\bar{\varepsilon}_{\mathrm{n+1}} \cdot \partial^{2}_{\boldsymbol{\sigma}\mathrm{g}_{\mathrm{i}}} \Phi_{\mathrm{n+1}} \cdot \mathrm{dg}_{\mathrm{i,n+1}} + \Delta\bar{\varepsilon}_{\mathrm{n+1}} \cdot \partial^{2}_{\boldsymbol{\sigma}\hat{\mathbf{h}}^{\mathbf{s}}} \Phi_{\mathrm{n+1}} : \mathrm{d}\hat{\mathbf{h}}^{\mathbf{s}}_{\mathrm{n+1}} \end{aligned}, \tag{3.41}$$

Substituting Eq. (3.41) into Eq. (3.40),

$$\begin{aligned} &\mathrm{d}\boldsymbol{\sigma}_{\mathrm{n+1}} = \boldsymbol{\Xi}_{\mathrm{n+1}} : \left(\mathrm{d}\boldsymbol{\varepsilon}_{\mathrm{n+1}} - \mathrm{d}\Delta\bar{\varepsilon}_{\mathrm{n+1}} \cdot \mathbf{A}_{\mathrm{n+1}} \right) \\ &\text{where} \\ &\mathbf{A}_{\mathrm{n+1}} = \left(\partial_{\boldsymbol{\sigma}} \Phi_{\mathrm{n+1}} + \partial^{2}_{\boldsymbol{\sigma}\mathrm{g}_{\mathrm{i}}} \Phi_{\mathrm{n+1}} \cdot \frac{\mathrm{dg}_{\mathrm{i,n+1}}}{\mathrm{d}\bar{\varepsilon}} \cdot \Delta\bar{\varepsilon}_{\mathrm{n+1}} + \partial^{2}_{\boldsymbol{\sigma}\hat{\mathbf{h}}^{\mathbf{s}}} \Phi_{\mathrm{n+1}} : \frac{\mathrm{d}\hat{\mathbf{h}}^{\mathbf{s}}_{\mathrm{n+1}}}{\mathrm{d}\bar{\varepsilon}} \cdot \Delta\bar{\varepsilon}_{\mathrm{n+1}} \right) \end{aligned}. \tag{3.42}$$

The consistency condition with Eq. (3.41) brings

$$\begin{aligned} &\mathrm{d}\Delta\bar{\varepsilon}_{\mathrm{n+1}} = \left\{ \partial_{\boldsymbol{\sigma}} \Phi_{\mathrm{n+1}} : \boldsymbol{\Xi}_{\mathrm{n+1}} : \mathrm{d}\boldsymbol{\varepsilon}_{\mathrm{n+1}} \right\} / \\ &\left\{ \partial_{\boldsymbol{\sigma}} \Phi_{\mathrm{n+1}} : \boldsymbol{\Xi}_{\mathrm{n+1}} : \mathbf{A}_{\mathrm{n+1}} - \partial_{\mathrm{g}_{\mathrm{i}}} \Phi_{\mathrm{n+1}} \cdot \frac{\mathrm{dg}_{\mathrm{i,n+1}}}{\mathrm{d}\bar{\varepsilon}} - \partial_{\hat{\mathbf{h}}^{\mathbf{s}}} \Phi_{\mathrm{n+1}} : \frac{\mathrm{d}\hat{\mathbf{h}}^{\mathbf{s}}_{\mathrm{n+1}}}{\mathrm{d}\bar{\varepsilon}} + \partial_{\bar{\varepsilon}} \bar{\sigma}\left(\bar{\varepsilon}_{\mathrm{n+1}} \right) \right\} \end{aligned}. \tag{3.43}$$

Finally, $\mathbf{C}^{\mathrm{ep}}$ can be calculated from Eqs. (3.43) and (3.42) as follows.

$$\begin{aligned} &\mathbf{C}^{\mathrm{ep}} = \boldsymbol{\Xi}_{\mathrm{n+1}} - \\ &\left(\frac{\boldsymbol{\Xi}_{\mathrm{n+1}} : \mathbf{A}_{\mathrm{n+1}} \otimes \boldsymbol{\Xi}_{\mathrm{n+1}} : \partial_{\boldsymbol{\sigma}} \Phi_{\mathrm{n+1}}}{\partial_{\boldsymbol{\sigma}} \Phi_{\mathrm{n+1}} : \boldsymbol{\Xi}_{\mathrm{n+1}} : \mathbf{A}_{\mathrm{n+1}} - \partial_{\mathrm{g}_{\mathrm{i}}} \Phi_{\mathrm{n+1}} \cdot \frac{\mathrm{dg}_{\mathrm{i,n+1}}}{\mathrm{d}\bar{\varepsilon}} - \partial_{\hat{\mathbf{h}}^{\mathbf{s}}} \Phi_{\mathrm{n+1}} : \frac{\mathrm{d}\hat{\mathbf{h}}^{\mathbf{s}}_{\mathrm{n+1}}}{\mathrm{d}\bar{\varepsilon}} + \partial_{\bar{\varepsilon}} \bar{\sigma}\left(\bar{\varepsilon}_{\mathrm{n+1}} \right)} \right) \end{aligned}. \tag{3.44}$$

Note that the previously formulated EBM-based algorithms with 4 residuals [55,57,58] can be retrieved if residuals in the current formulation are properly reduced. Moreover, the numerical algorithm can be simply extended to a general stress state. The flow chart of the proposed fully implicit EBM and CPM algorithms is shown in Figure 3.2.

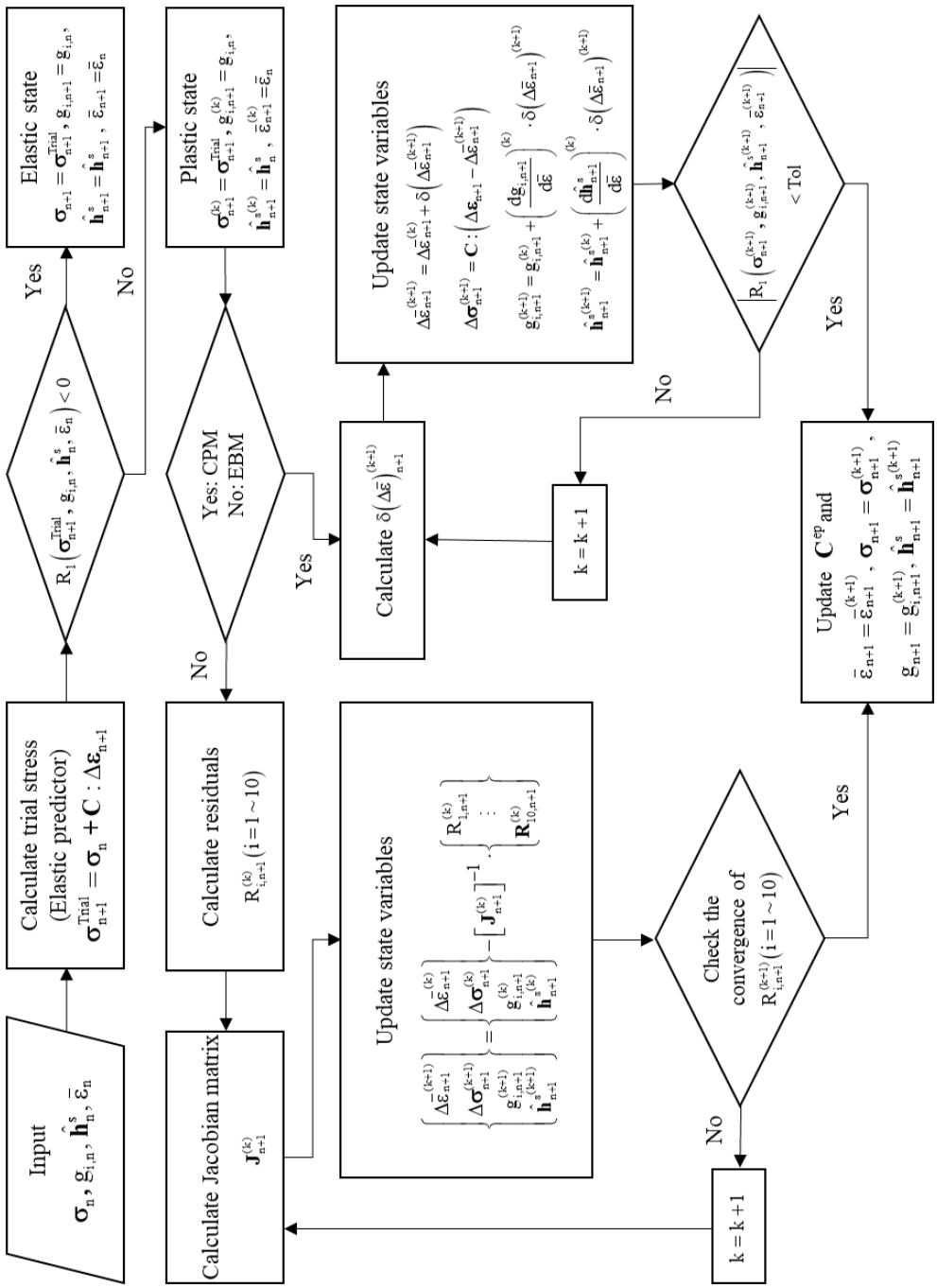

Figure 3.2. Flow chart for two stress update schemes; CPM and EBM.

3.5. Evaluations of stress update algorithms for the HAH

In this section, evaluations of the numerical accuracy and stability of the proposed stress integration algorithms are analyzed for different case problems. The algorithms described in the previous sections were implemented in the static implicit finite element software ABAQUS/Standard using the user material subroutine UMAT.

For the comparative study, 4 algorithms were implemented in the FE model; CPM, EBM-4R, EBM-14R/AD, EBM-14R/ND. Here, 4R and 14R denote 4 and 14 residuals based on EBM algorithms, respectively, and AD and ND represent the analytical derivative and numerically calculated derivatives based on finite difference, respectively. Note that the EBM-14R represents the fully implicit Euler backward algorithm implemented for the extended HAH model for the first time.

The two-level of the evaluation procedure is presented in the following sections. First is a very detailed fundamental analysis on the accuracy of the different algorithms for the investigated anisotropic hardening model, HAH. For this, the anisotropic characteristics of flow stress and r-value are predicted and evaluated under two different loading paths. Only a single element is used in this level to rule out other numerical effects. To clarify the effect of

anisotropic hardening responses of the enhanced HAH under different loading paths, various model materials are selectively compared. The investigated model materials for the evaluation exhibit high or low evolution rates, and hardening or softening under cross-loading. To represent the initial anisotropy of material, the non-quadratic anisotropic yield function, Yld2000-2d [71, 72] is employed. The summary of the initial (undistorted) yield function, Yld2000-2d is referred to Appendix C.

The other level is a real scale simulation based on the S-rail forming and springback process [42], which was proposed as a benchmark problem and often utilized for the analysis of constitutive model and numerical algorithm in the sheet metal forming community. The reason for choosing the benchmark is that most of the existing finite element simulations have been based on hybrid explicit and implicit algorithms. In other words, the forming process is solved by the dynamic explicit FE model as a quasi-static problem, while the springback is calculated by a static implicit algorithm. The first is applied to avoid divergence problems typically encountered in the contact problems between complex tools and sheet metal, and the implicit algorithm is optimum for the unloading process of springback to reduce the computational time. In this study, all the stress integration algorithms are implemented into the static implicit FE software and the numerical

performance of each algorithm is comparatively studied for their applicability to industrial-sized problems. Two materials, stainless steel (STS) and dual-phase steel (DP) are investigated because they have been used for real automotive parts and show distinctive anisotropic hardening behaviors under loading path changes.

3.5.1. One element analysis

In the one element analysis, the loading condition is a compression-tension (C-T). The accuracies of the predicted flow stress and r-value are compared for the investigated numerical algorithms. Two loading paths are simulated for the C-T test. The first path is a 5% compression along the rolling direction (RD) followed by a 10% tension in the same direction. This case is denoted as 'C5T10R'. Here, 'R' represents that the loading path is 'Reversed' loading. During the compression along RD, the rate of yield function distortion represented by the transient behavior and the Bauschinger effect is maximum on the opposite side of compressive loading or tension along RD.

The second loading path is a 5% compression along RD followed by 10% tension along 54° to the RD. Note that the angle 54° corresponds to the cross-

loading in which the condition $\mathbf{h}^{s} : \hat{\mathbf{s}} = 0$ is satisfied[1]. The second case is denoted as 'C5T10CR' in which 'CR' represents the "Cross" loading. This loading path is selected because the cross-loading effect with rotation of microstructure deviator becomes maximized at the loading direction with $\mathbf{h}^{s} : \hat{\mathbf{s}} = 0$ condition.

A 4-node shell element with reduced integration in ABAQUS/Standard, or S4R, is used. The boundary conditions for the above cases are schematically shown in Figure3.3.

The r-value along angle θ to RD is defined in Eq. (3.45) and calculated by nodal displacements of an element.

$$\begin{aligned} & r_{\theta} = \frac{\varepsilon^{p}_{width}}{\varepsilon^{p}_{thickness}} = -\frac{\varepsilon^{p}_{2}}{\varepsilon^{p}_{1} + \varepsilon^{p}_{2}}, \\ & \text{where } \left\{ \varepsilon^{p}_{1} = \ln\left(1 + \Delta u^{p}_{1}\right) \text{ and } \varepsilon^{p}_{2} = \ln\left(1 + \Delta u^{p}_{2}\right) \right\}, \end{aligned} \quad . \tag{3.45}$$

where, Δu^{p}_{1} and Δu^{p}_{2} are the element nodal displacements along RD and transverse direction (TD), respectively, during tension, and the superscript ' p ' represents the plastic part of the strain or displacement.

[1] The exact angle for the cross-loading condition is 54.74°.

In Table 1 and 2, the mechanical properties of the two model materials and the constitutive parameters for the initial yield function and e-HAH model are listed, respectively. The model material 'MAT 1' and 'MAT 2' have distinctive HAH parameters, but other properties such as elasticity, initial yield function, and isotropic hardening are identical. For the isotropic hardening, the power-law type Swift hardening law, $\bar{\sigma}\left(\bar{\varepsilon}\right) = \mathrm{K}\left(\mathrm{e}_0 + \bar{\varepsilon}\right)^{\mathrm{n}}$ is applied for both materials.

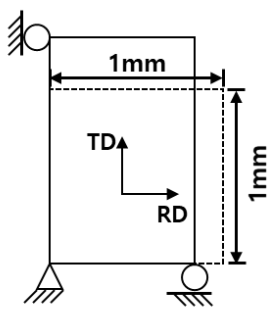

0° Compression

(a)

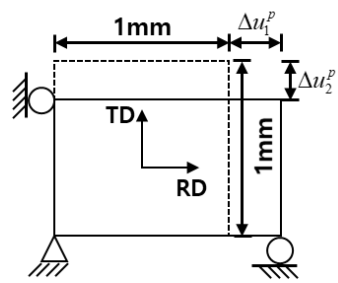

0° Tension

(b)

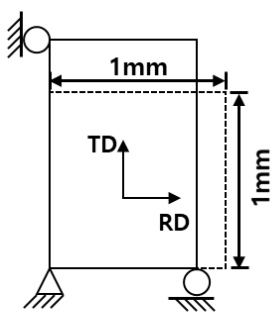

0° Compression

(c)

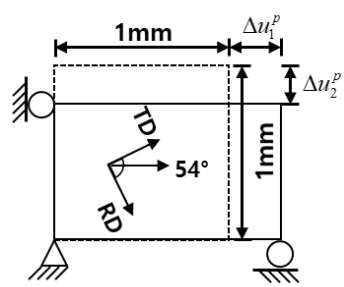

54° Tension

(d)

Figure 3.3. Boundary conditions for the one element compression-tension analysis: (a) 5% compression along RD followed by (b) 10% tension along RD, (c) 5% compression along RD followed by (d) 10% tension along 54° to RD. The dashed line and the solid line represent before deformation and after deformation, respectively.

Table 3.1. Anisotropic mechanical properties. The subscript 0, 45, 90 represent rolling direction (RD), diagonal direction (DD), and transverse direction (TD), respectively.

Material	σ_0/σ_0	σ_{45}/σ_0	σ_{90}/σ_0	σ_b/σ_0	r_0	r_{45}	r_{90}	r_b
MAT 1, 2	1.0	1.0	1.0	1.0	0.5	1.0	1.5	1.0

Table 3.2. Constitutive parameters of isotropic linear elasticity and e-HAH model.

Elastic and isotropic hardening parameters										
Material	E[GPa]		Poisson's ratio		K (MPa)		e_0		n	
MAT 1,2	70.0		0.33		500.0		0.01		0.2	
Yld2000-2d coefficients										
Material	m	α_1	α_2	α_3	α_4	α_5	α_6	α_7	α_8	
MAT 1,2	8.0	0.7826	1.1778	1.1075	0.9753	1.0154	0.9028	0.9989	0.9990	
Enhanced HAH model parameters										
Material	q	k	k_1	k_2	k_3	k_4	k_5	L	k_L	S	k_S
MAT 1	2.0	250.0	300.0	250.0	0.25	0.80	50	1.0	0.0	0.80	75.0
MAT 2	2.0	25.0	60	50.0	0.90	0.80	50	1.65	384.0	1.0	0.0

Figure 3.4-3.7 show the reference flow stress curves and the corresponding evolution of HAH surfaces of MAT 1 and MAT 2. Since the exact solutions are not available, a reference curve with a sufficiently small time step is assumed to be exact. The reference flow curves are obtained by the CPM implemented in the dynamic explicit FE software ABAQUS/Explicit with a user material subroutine VUMAT. The average strain increment is 2.4×10^{-8}. Figure 3.4(a) and Figure 3.6(a) present the flow stresses under the loading path C5T10R, while those in Figure 3.5(a) and Figure 3.7(a) are under C5T10CR. The evolutions of yield surfaces are provided in Figure 3.4(b) and Figure 3.6(b) for C5T10R, and Figure 3.5(b) and Figure 3.7(b) for C510CR. For comparison, the evolutions of isotropic yield surfaces are also included in the figures. In each figure, the three points A, B, C are indicated, where A and C represent the initial and final stress states during the second loading, respectively, and B is selected between the two loading points to compare the transient behavior in the second loading path.

Figure 3.4(a) and (b) show that a significant amount of the Bauschinger effect and permanent softening ($g_4 \cdot \bar{\sigma} = 0.8224 \cdot \bar{\sigma}$) are represented from the HAH parameters of MAT 1 under C5T10R. For C5T10CR in Figure 3.5(a) and (b), similar transient behavior and permanent softening are calculated, but the Bauschinger effect (contraction) is much less than the loading path

C5T10R. For MAT 2, the Bauschinger effect is less than the MAT 1 for loading path C5T10R though the permanent softening is also pronounced. However, the loading condition C5T10CR shows very noticeable stress overshooting after loading path change, and subsequent softening. Note that the two model materials MAT 1 and 2 are virtually designed to represent the characteristics of the HAH model.

In the following, the accuracy of each investigated stress integration algorithm is assessed with different time increments. The effect of time step size on the accuracy of stress update is evaluated by one element simulations under the two loading paths. Three different strain increments during tensile loading are considered: 5.0×10^{-3}, 5.0×10^{-4} and 5.0×10^{-6}.

From the simulations, the evolution of flow stress and r-value at the second loading step are evaluated and the averaged relative errors are reported using the following equations.

$$\begin{aligned} \text{Error}_{\sigma} &= \frac{1}{N}\sum_{m=1}^{N}\frac{\left|\sigma_m^{exact}-\sigma_m\right|}{\sigma_m^{exact}}\times 100(\%) \\ \text{Error}_{r} &= \frac{1}{N}\sum_{m=1}^{N}\frac{\left|r_{\theta,m}^{exact}-r_{\theta,m}\right|}{r_{\theta,m}^{exact}}\times 100(\%) \end{aligned} \quad . \tag{3.45}$$

where N is a total number of data points used for the error estimations.

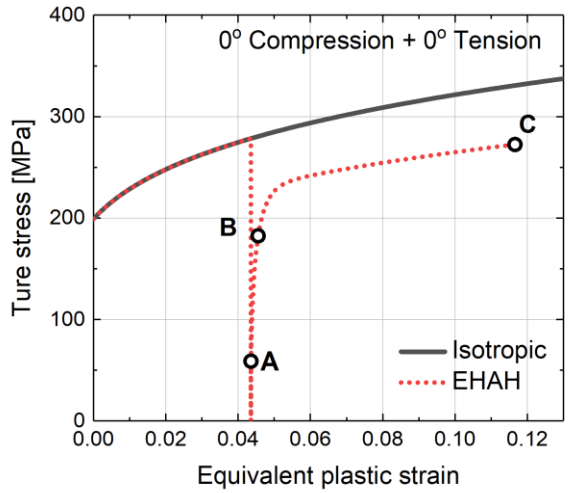

(a)

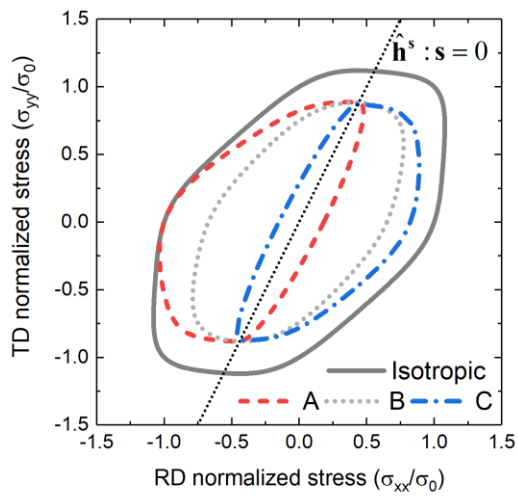

(b)

Figure. 3.4. Stress-equivalent plastic strain curve and evolution of the HAH yield surface for MAT 1: (a) flow stress curve and (b) HAH yield locus for C5T10R.

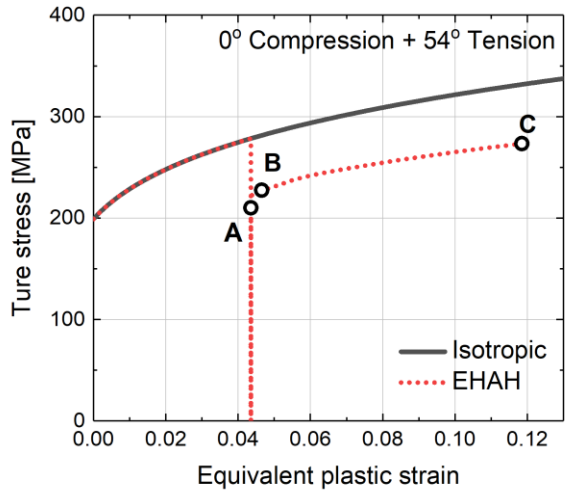

(a)

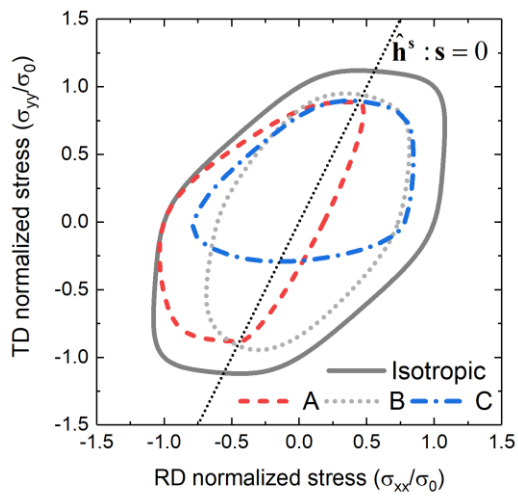

(b)

Figure. 3.5. Stress-equivalent plastic strain curve and evolution of e-HAH yield surface for MAT 1: (a) flow stress curve and (b) HAH yield locus for C5T10CR.

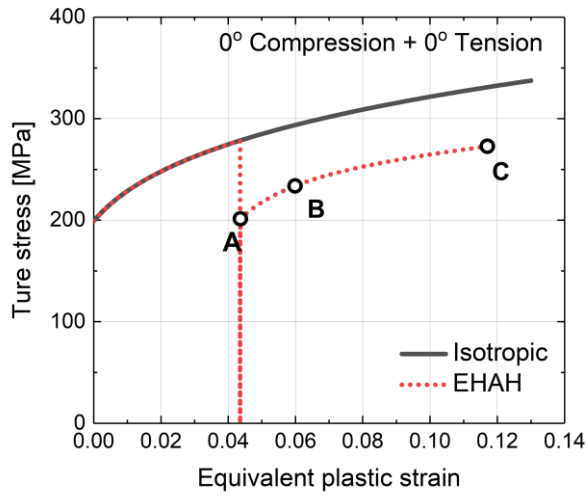

(a)

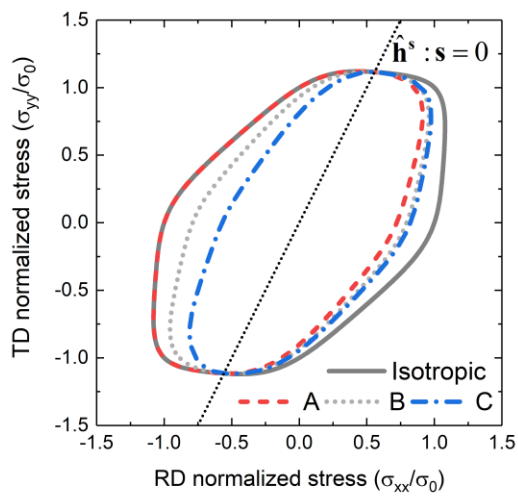

(b)

Figure. 3.6. Stress-equivalent plastic strain curve and evolution of e-HAH yield surface for MAT 2: (a) flow stress curve and (b) HAH yield locus for C5T10R.

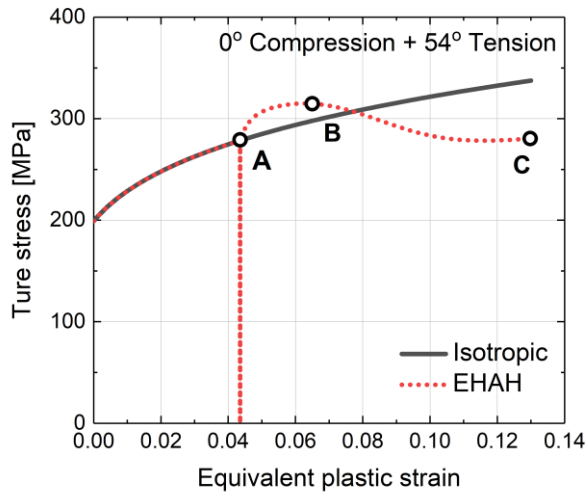

(a)

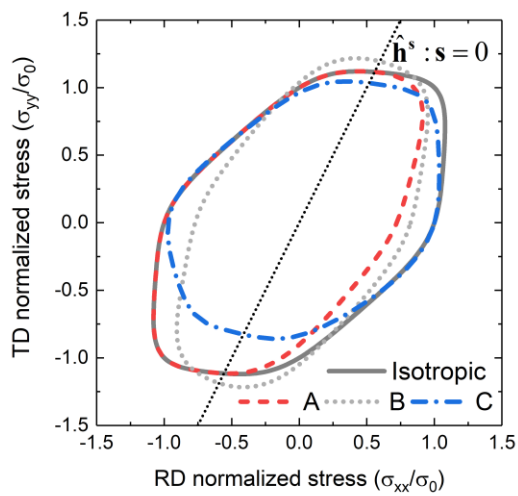

(b)

Figure. 3.7. Stress-equivalent plastic strain curve and evolution of e-HAH yield surface for MAT 2: (a) flow stress curve and (b) HAH yield locus for C5T10CR.

3.5.1.1. Loading condition: C5T10R

Figure 3.8 and 3.9 show the flow stress curves and r-value evolutions of MAT 1 and MAT 2, respectively, under the C5T10R loading path. Three different strain increments were applied to each stress integration algorithm for this analysis. The detailed values including relative errors and CPU times are also listed in Table 3 and 4 for MAT 1 and MAT 2, respectively. At the first glance, all the numerical algorithms investigated look to present rather similar results. But, there are some distinctive features in the predicted flow curves and r-values. Regarding the method of yield surface gradient calculation, both methods based on analytical derivatives (EBM-14R/AD) and finite difference (EBM-14R/ND) predicted almost the same level of accuracy when it is implemented in the fully implicit algorithm with 14 residuals. There are small differences in the computational cost measured by CPU time between the two cases. That is, EBM-14R/ND with finite difference method takes ~8% longer CPU time than the EBM-14R/AD with analytical derivatives.

The effect of investigated algorithms on the accuracy and stability of the simulations with the HAH model becomes considerable when the evolution of yield surface becomes drastic within a given time increment. The flow stress curves predicted by CPM and EBM-4R (with 4 residuals based) show

significant oscillations at the early strain range of MAT 1 when the strain increment is large with $\Delta\varepsilon_{xx} = 5\times10^{-3}$, which is shown in Figure 3.8(a) In contrast, the two algorithms with the same strain increment are stable for MAT 2 which shows less evolution rate than MAT 1 (Figure 3.9(a)). The state variable, g_1 controls the transient rate and Figure 3.10(a) shows its oscillations for MAT 1 when CPM and EBM-4R are used. As expected g_1 value of MAT 2 shows stable evolution even for the CPM and EBM-4R algorithms. In terms of the r-value evolution, the predicted values by CPM show very less accuracy for the strain increment of $\Delta\varepsilon_{xx} = 5\times10^{-3}$. This inaccuracy is attributed to the ignorance of flow rule as a residual during the algorithmic treatment in the CPM.

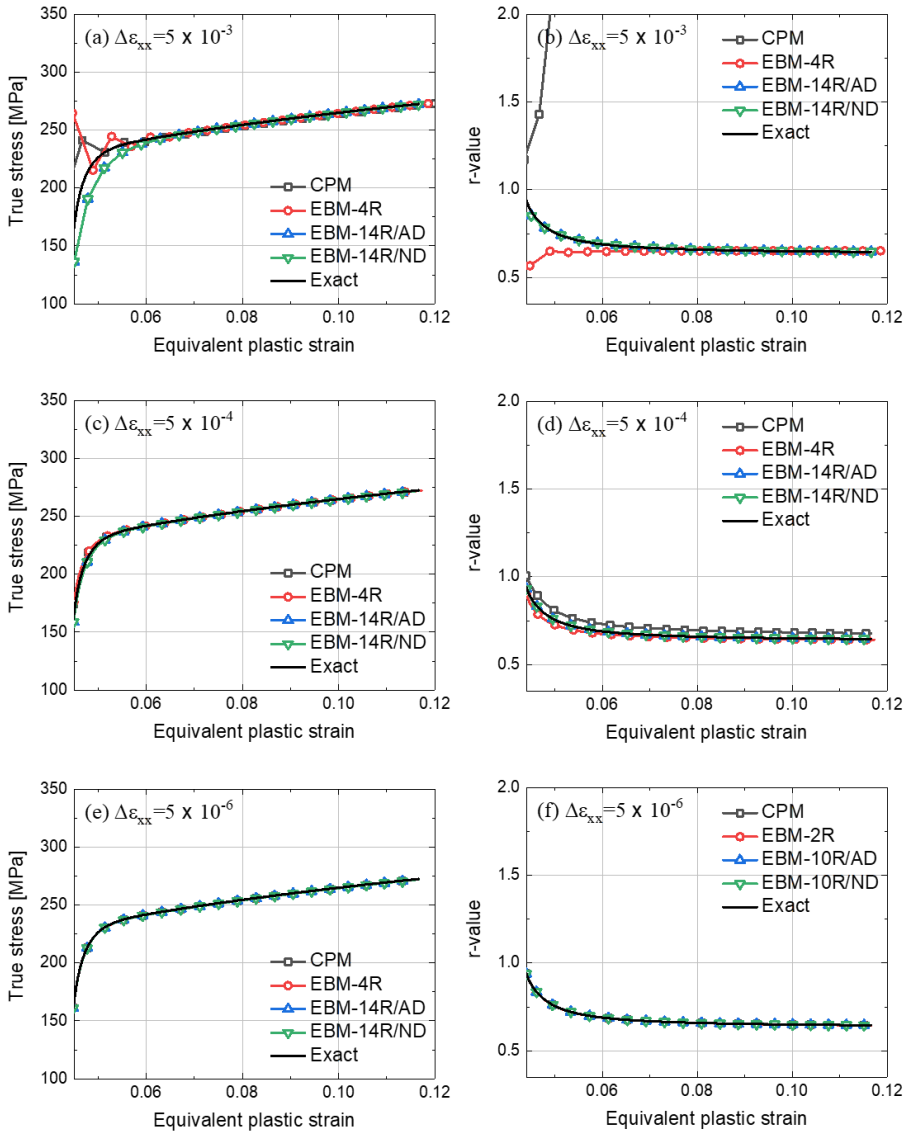

Figure. 3.8. The evolution of the flow stresses and r-values of MAT 1 under C5T10R path for different stress integration algorithms with strain increments: (a),(b) $\Delta\varepsilon_{xx} = 5\times10^{-3}$, (c), (d) $\Delta\varepsilon_{xx} = 5\times10^{-4}$, and (e), (f) $\Delta\varepsilon_{xx} = 5\times10^{-6}$.

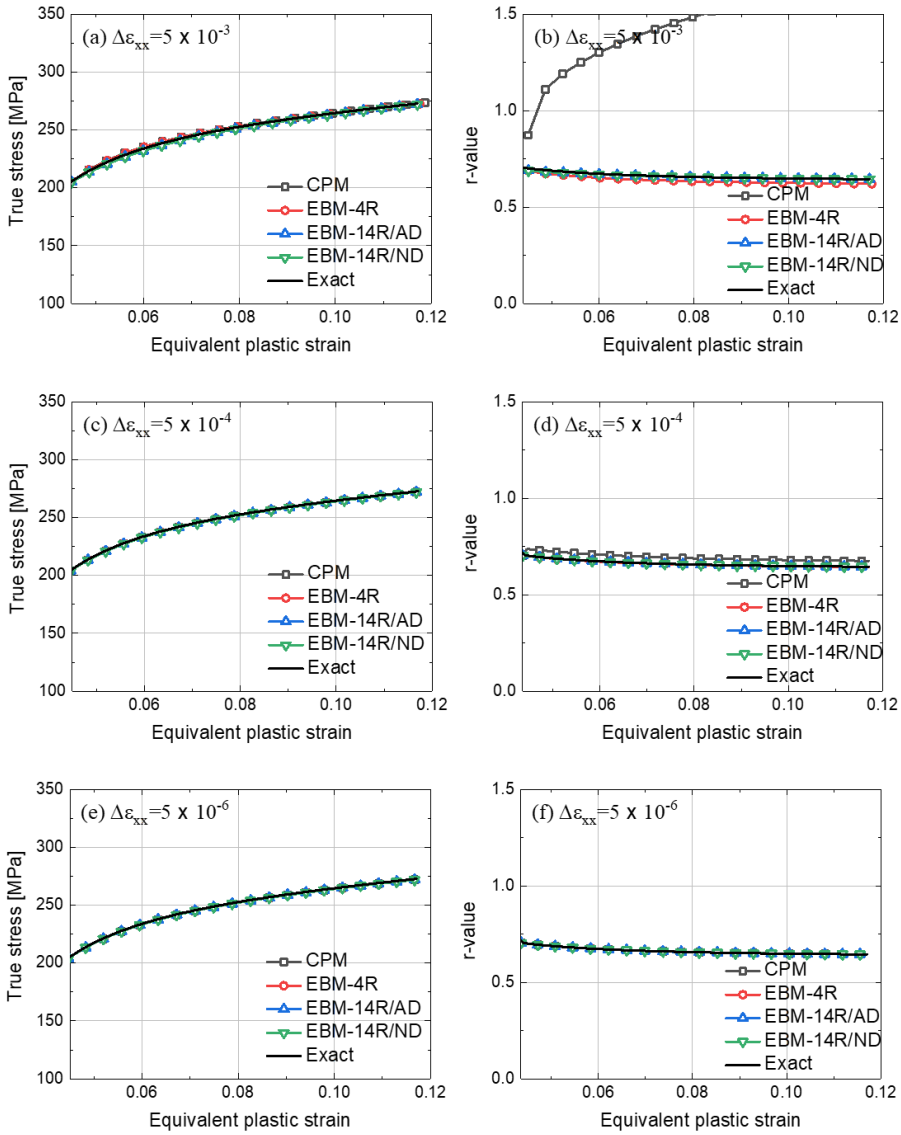

Figure. 3.9. The evolution of the flow stresses and r-values of MAT 2 under C5T10R path for different stress integration algorithms with strain increments: (a),(b) $\Delta\varepsilon_{xx} = 5\times10^{-3}$, (c), (d) $\Delta\varepsilon_{xx} = 5\times10^{-4}$, and (e), (f) $\Delta\varepsilon_{xx} = 5\times10^{-6}$.

Table 3.3. Average relative errors in the flow curves and r-values of MAT 1 under C5T10R.

Algorithm	$\Delta\varepsilon_{xx}$	$Error_{\sigma}$ (%)	$Error_{r}$ (%)	Total CPU time(sec)
CPM	5×10^{-3}	2.38	316	1.1
	5×10^{-4}	0.42	5.83	5.7
	5×10^{-6}	0.14	0.048	205
EBM-4R	5×10^{-3}	4.34	5.23	0.5
	5×10^{-4}	0.95	1.80	5.7
	5×10^{-6}	0.14	0.035	232
EBM-14R/AD	5×10^{-3}	1.62	0.63	0.6
	5×10^{-4}	0.32	0.10	5.8
	5×10^{-6}	0.14	0.010	231
EBM-14R/ND	5×10^{-3}	1.62	0.63	0.7
	5×10^{-4}	0.32	0.10	5.9
	5×10^{-6}	0.14	0.010	249

Table 3.4. Average relative errors in the flow curves and r-values of MAT 2 under C5T10R.

Algorithm	$\Delta\varepsilon_{xx}$	$Error_{\sigma}$ (%)	$Error_{r}$ (%)	Total CPU time(sec)
CPM	5×10^{-3}	0.42	124	0.8
	5×10^{-4}	0.18	4.88	5.9
	5×10^{-6}	0.21	0.048	206
EBM-4R	5×10^{-3}	0.27	3.43	0.7
	5×10^{-4}	0.17	0.19	6.0
	5×10^{-6}	0.21	0.022	202
EBM-14R/AD	5×10^{-3}	0.49	0.30	0.6
	5×10^{-4}	0.25	0.05	5.7
	5×10^{-6}	0.22	0.021	201
EBM-14R/ND	5×10^{-3}	0.49	0.29	0.7
	5×10^{-4}	0.25	0.04	6.0
	5×10^{-6}	0.22	0.021	227

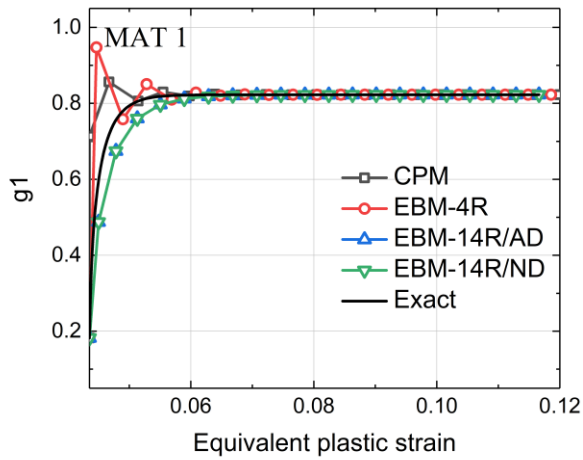

(a)

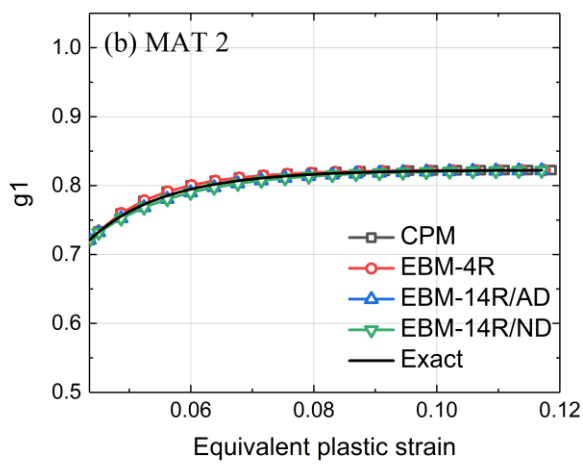

(b)

Figure. 3.10. Evolutions of the state variables g_1 for different stress integration algorithms with strain increment $\Delta\varepsilon_{xx} = 5\times10^{-3}$: (a) MAT 1and (b) MAT 2.

3.5.1.2. Loading condition: C5T10CR

Figure 3.11 and 12 show the flow stresses and r-value evolutions under the cross-loading path, C5T10CR, for MAT 1 and MAT 2, respectively. The accuracy and stability of the investigated stress integration algorithms for MAT 1 and MAT 2 are summarized in Table 3.5 and Table 3.6, respectively. Similar to the reverse loading path, C5T10R, overall accuracies in flow stress and r-values increase as the strain increment decreases as readily expected. However, due to the anisotropic hardening and its orthogonal distortion in the e-HAH model, special observations can be also noticed, which mostly occur with the large strain increment, $\Delta\varepsilon_{xx} = 5\times10^{-3}$. The evolution of the r-value predicted by CPM showed abnormal behavior as shown in Figure 3.11(a). This is because the semi-explicit algorithm does not account for the minimization of residual for a flow rule. Moreover, as shown in Figure 3.11(a) and (b), the flow stresses and r-values predicted by CPM and EBM-4R show different tendencies from algorithms with 14 residual-based EBMs. In Figure 3.13(a) and (b), the evolutions of the two-state variables, g_1 and g_2, with strain increment, $\Delta\varepsilon_{xx} = 5\times10^{-3}$ are presented. Under this loading path, the transient behavior of CPM and EBM-4R is controlled by g_2 because the loading path indicator $\cos\chi$ is negative for both algorithms (Figure 3.14

(a)). However, in contrast, other algorithms including the exact solution $\cos\chi$ is positive which leads g_1 to having a major effect on the transient behavior. This is the cause of abnormally predicted flow stress curves and r-value evolutions of the two algorithms. That is, the undesirable evolutions of state variables result in significantly deviated stress updates in the HAH model as shown in Figure 3.14(d).

Similar to MAT 1, oscillating flow curves are also predicted with CPM and EBM-4R for MAT 2 when the time increment is not small enough. In this loading path, this fluctuating flow behavior is attributed to the state variable g_L associated with the latent hardening (Figure 3.15). Note that the flow curve of MAT 2 is more influenced by g_L than MAT 1 because of the slower evolution of $\mathbf{h}^s$.

In terms of the computational time, all investigated numerical algorithms present marginally similar computation times in comparison to a much larger difference in accuracy, especially under large strain increments. However, there is a meaningful point to be noticed between the algorithms of EBM-14R/ND and EBM-14R/AD. That is, the finite difference gradient-based algorithm (EBM-14R/ND) has a 10~15% longer CPU time than those of the analytical gradient algorithm (EBM-14R/AD) for the C5T10CR loading path.

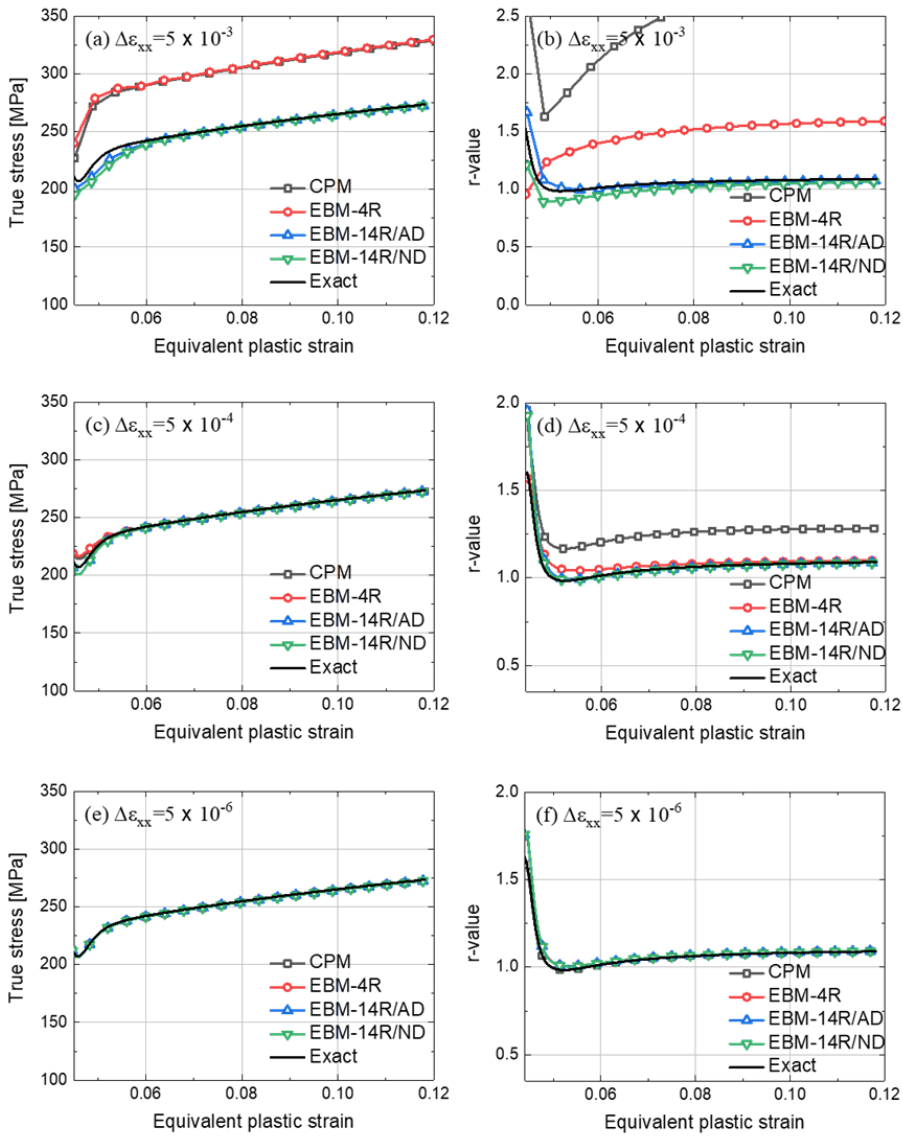

Figure. 3.11. The evolution of the flow stresses and r-values of MAT 1 under C5T10CR path for different stress integration algorithms with strain increments: (a),(b) $\Delta\varepsilon_{xx} = 5\times10^{-3}$, (c), (d) $\Delta\varepsilon_{xx} = 5\times10^{-4}$, and (e), (f) $\Delta\varepsilon_{xx} = 5\times10^{-6}$.

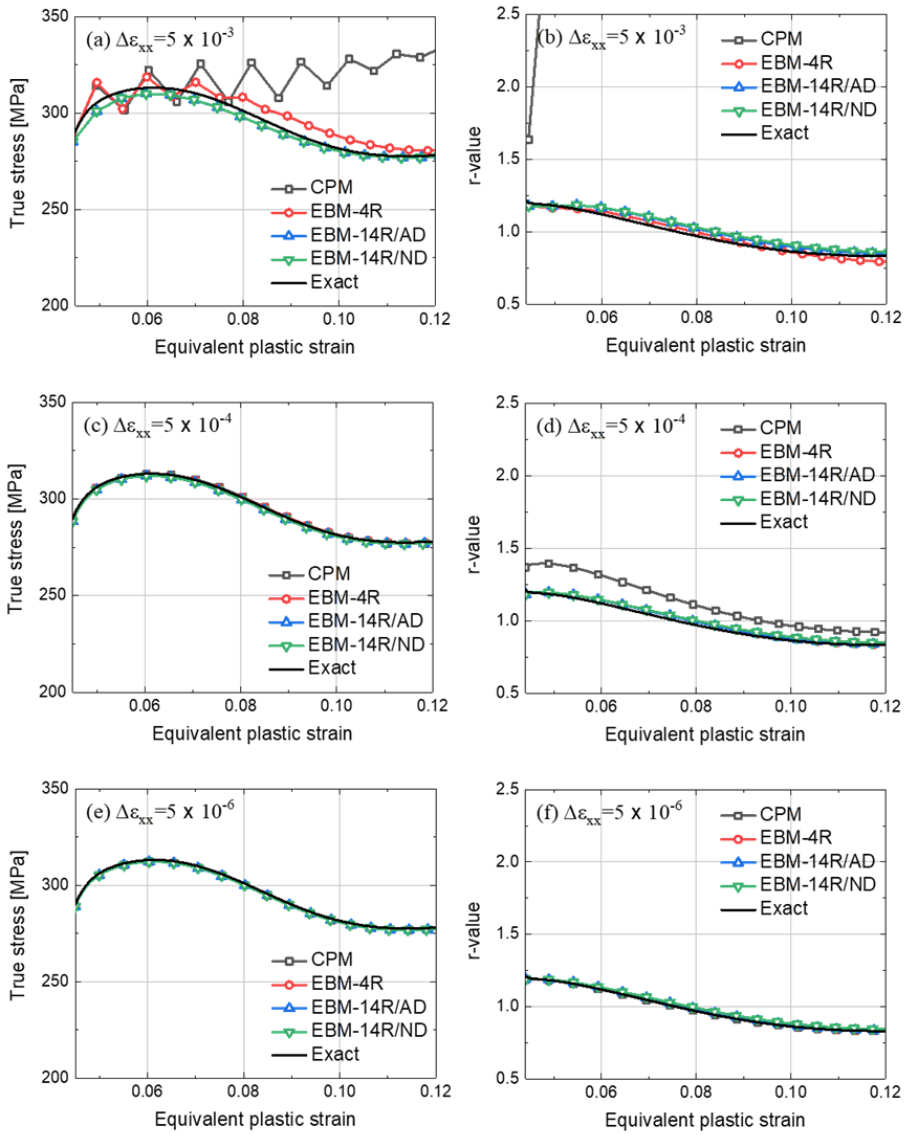

Figure. 3.12. The evolution of the flow stresses and r-values of MAT 2 under the C5T10CR path for different stress integration algorithms with strain increments: (a),(b) $\Delta\varepsilon_{xx} = 5\times10^{-3}$, (c), (d) $\Delta\varepsilon_{xx} = 5\times10^{-4}$, and (e), (f) $\Delta\varepsilon_{xx} = 5\times10^{-6}$.

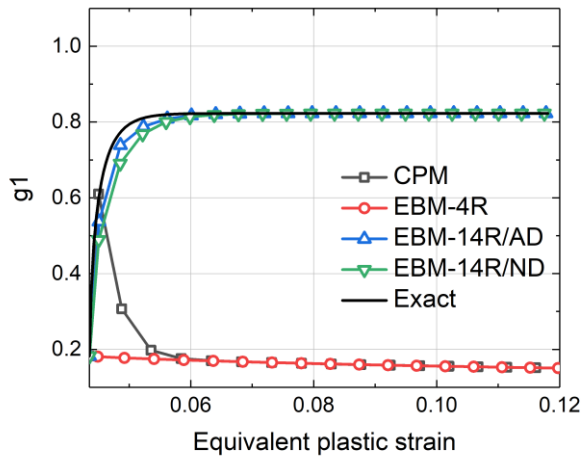

(a)

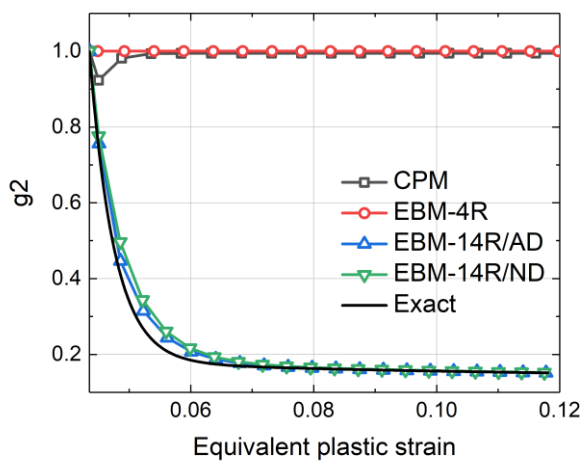

(b)

Figure 3.13. The evolutions of (a) g_1, (b) g_2 for different numerical algorithms under the C5T10CR loading path. The strain increment is $\Delta\varepsilon_{xx} = 5\times10^{-3}$.

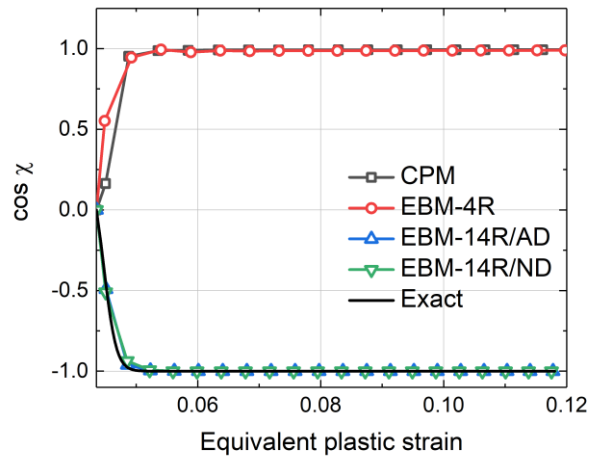

(a)

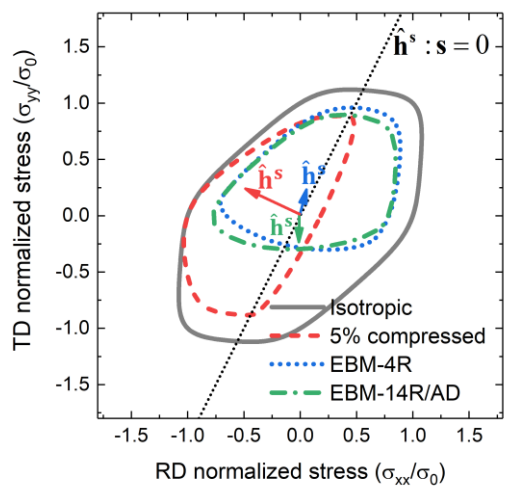

(b)

Figure 3.14. The evolutions (a) $\cos\chi$ for different numerical algorithms under the C5T10CR loading path. (b) Yield loci for EBM-4R and EBM-14R/AD with $\mathbf{h}^{s}$. The strain increment is $\Delta\varepsilon_{xx} = 5\times10^{-3}$.

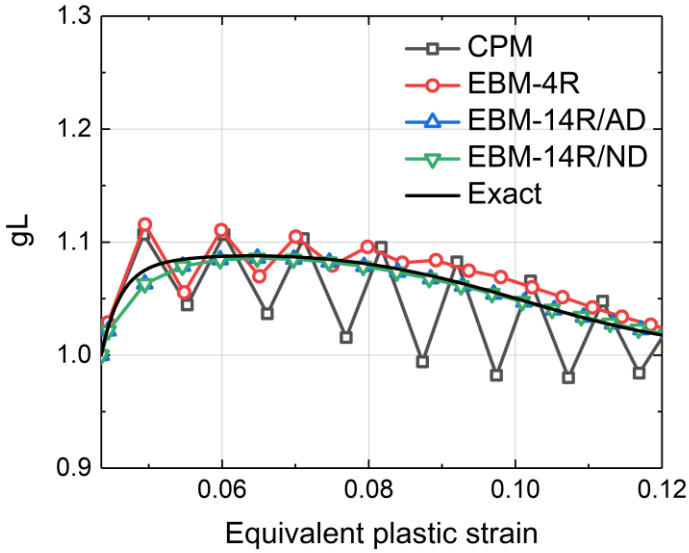

Figure 3.15. Evolution of g_L for different stress integration algorithms under the loading path C3T10CR with strain increment, $\Delta\varepsilon_{xx} = 5\times10^{-3}$.

Table 3.5. Average relative errors in the flow curves and r-values of MAT 1 under C5T10CR.

Algorithm	$\Delta\varepsilon_{xx}$	$Error_{\sigma}$ (%)	$Error_{r}$ (%)	Total CPU time(sec)
CPM	5×10^{-3}	22.2	155	1.6
	5×10^{-4}	0.56	19.4	5.9
	5×10^{-6}	0.65	0.57	196
EBM-4R	5×10^{-3}	22.4	43.8	0.5
	5×10^{-4}	0.61	2.86	6.2
	5×10^{-6}	0.65	1.60	210
EBM-14R/AD	5×10^{-3}	0.38	2.78	0.8
	5×10^{-4}	0.88	1.89	6.0
	5×10^{-6}	0.66	1.57	222
EBM-14R/ND	5×10^{-3}	0.44	4.77	1.1
	5×10^{-4}	0.88	1.84	7.6
	5×10^{-6}	0.66	1.58	260

Table 3.6. Average relative errors in the flow curves and r-values of MAT 2 under C5T10CR.

Algorithm	$\Delta\varepsilon_{xx}$	$Error_{\sigma}$ (%)	$Error_{r}$ (%)	Total CPU time(sec)
CPM	5×10^{-3}	12.7	663	0.8
	5×10^{-4}	0.16	13.4	5.7
	5×10^{-6}	0.27	0.10	210
EBM-4R	5×10^{-3}	1.61	2.98	0.5
	5×10^{-4}	0.11	1.60	6.0
	5×10^{-6}	0.28	0.96	208
EBM-14R/AD	5×10^{-3}	0.57	3.71	0.7
	5×10^{-4}	0.33	1.55	7.1
	5×10^{-6}	0.28	0.95	200
EBM-14R/ND	5×10^{-3}	0.56	4.91	1.3
	5×10^{-4}	0.33	2.45	13.0
	5×10^{-6}	0.28	1.83	221

3.5.2. Industrial problem: S-rail forming and springback

In this section, the proposed stress integration algorithms are applied to the simulation of the large-scale industrial part forming with purely implicit FE software. Though the implicit FE has been employed for the large-scale models, this is often limited to simple material constitutive law such as isotropic and kinematic hardening. To the best knowledge of the present authors, the application of the anisotropic distortional hardening model with cross-hardening or softening (that is, HAH model) to the simulation of industrial forming process with a static implicit FE is the first trial. Alternatively, numerous studies have employed the combined dynamic explicit and implicit approach for complex forming and elastic driven springback simulations, respectively. This is even more true when the elastic-plasticity constitutive laws become more complex like the present anisotropic hardening model, HAH.

In this study, the S-rail part forming and springback simulations are performed as a benchmark of the industrial forming process [42]. The simulations were carried out by the static implicit solver, ABAQUS/Standard. From the simulation results, springback, equilibrium iterations, time increment, and computation time during the forming step were comparatively

analyzed among CPM, EBM-14R/AD, and EBM-14R/ND algorithms. Real automotive sheet metals made of dual-phase steel (DP780) and stainless steel (STS) are employed in the simulations. Note that DP780 shows significant cross-contraction (or softening) behavior under loading path changes due to the large Baushinger effect induced by its martensitic islands embedded in the ferrite matrix. In contrast, the STS sheet exhibits stress over-shooting or cross-hardening behavior under loading path changes. The material properties and their related model parameters are listed in Table. 3.7. In Figure 3.16, the FE model set-up including tool and sheet dimensions is presented.

Table 3.7. Constitutive parameters of isotropic linear elasticity and e-HAH model.

Elastic and isotropic hardening parameters										
Material		E[GPa]		Poisson's ratio		K (MPa)		e_0		n
DP780		194.0		0.33		1295.0		0.0008		0.142
STS		223.9		0.33		882.6		0.0056		0.224
Yld2000-2d coefficients										
Material	m	α_1	α_2	α_3	α_4	α_5	α_6	α_7	α_8	
DP780	6	0.946	1.022	1.015	1.000	1.011	0.968	1.009	1.006	
STS	2	1.0	1.0	1.0	1.0	1.0	1.0	1.0	1.0	
Enhanced HAH model parameters										
Material	q	k	k_1	k_2	k_3	k_4	k_5	L	k_L	S	k_S
DP780	2	120.0	150.0	78.5	0.25	1.0	0.0	1.0	0.0	0.8	75.0
STS	2	18.7	580.0	10.0	0.90	0.88	240	1.65	384.0	1.0	0.0

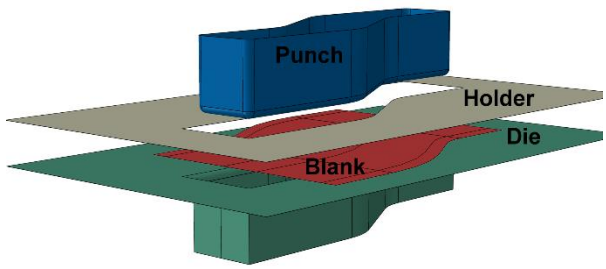

(a)

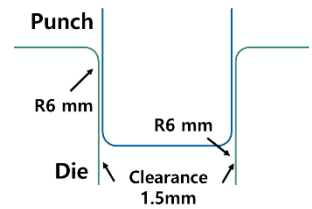

(b)

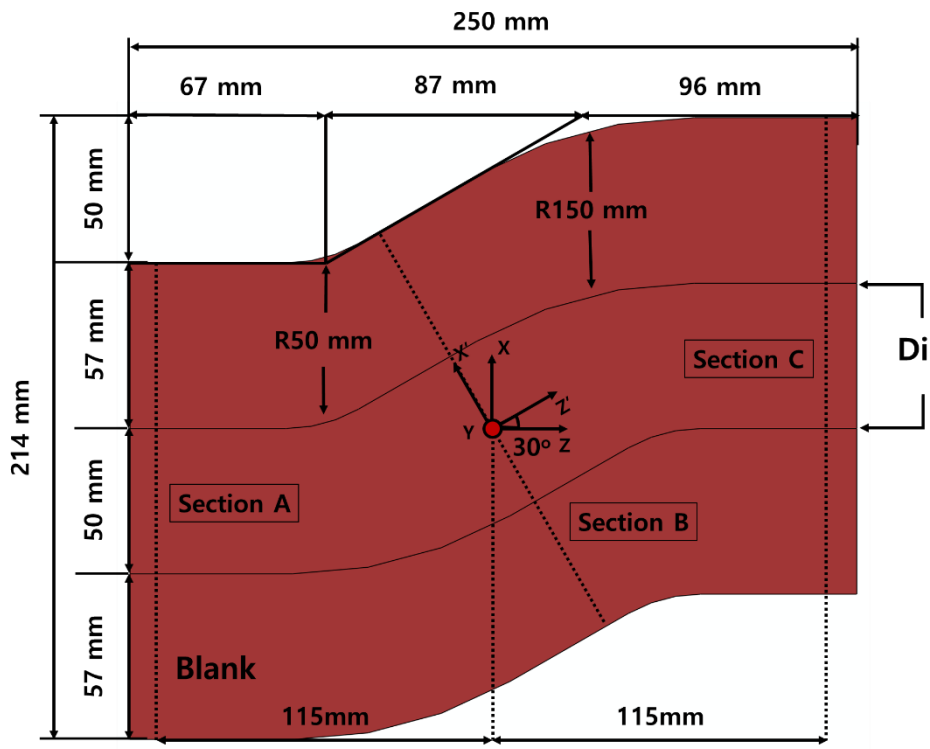

(c)

Figure 3.16. (a) Schematic view of FE model set-up for S-rail forming simulation, (b)-(c) dimensions of the tools and blank, respectively.

.

The thickness of the blank sheet is 1.2mm and the blank holding force of 200kN was applied during the forming simulation. The friction coefficient between the blank and tools was set as 0.05. A total of 37mm punch displacement was applied. As for blank elements, 4264 4-node shell elements with reduced integration (S4R) were used. The simulation consisted of holding, forming, and springback steps. Springback simulations were conducted by removing the tools after applying constraints on three specific nodes on X'-Z' plane to prevent the rigid body motion. That is, the center node was fixed, one node on the Z' axis was constrained along the X' and Y' direction, and the last node on the X' axis was constrained along the Z' direction. The simulation time for each step equals one (though it does not have physical meaning due to the static implicit FE algorithm. This is a relative measure for the strain increment control for different stress integration algorithms). The reference, minimum and maximum time increments for forming step were 5.0×10^{-3}, 1.0×10^{-5} and 1.0×10^{-2}, respectively.

The springbacks at sections A, B, and C are described in Figure 3.16(c). Section A and C are on the Z-plane $\pm115\,\mathrm{mm}$ away from the center. Section B lies on the Z'-plane which is 30 degrees rotated plane along the Y-axis.

In Figure 3.17 and 18, the springback results at sections A, B, and C are presented for DP780 and STS. There are almost no differences in springback results among the investigated algorithms. This may be due to the automatic time stepping built-in ABAQUS and the time increment is relatively small enough to have accurate solutions.

In Table 3.8, the averaged equilibrium iteration number, averaged time increment (Δt_{avg}) and relative wallclock time are listed. The relative wallclock time is normalized with the value calculated by the CPM. There are quite big differences in the size of time increment and the calculation time among the algorithms. The average time increment for CPM is almost half of the one based on EBM. It is considered that the tangent modulus calculated with CPM is not consistent with the Newton-Raphson method in ABAQUS, which requires a rather smaller time step compared to EBM algorithms.

For both materials, EBM-14R/AD and EBM-14R/ND show the negligible difference for averaged time increment and the average equilibrium iteration number. In other words, the approximate computation cost for global equilibrium calculation in FE software between the two algorithms is similar. It is presumed that the two algorithms have very similar accuracy under a given time increment. In the case of the STS, the EBM-14R/AD and the

EBM-14R/ND show similar wallclock times, whereas in the case of the DP780 it is different. The EBM-14R/ND is approximately 40% slower than the EBM-14R/AD and the difference is much bigger than the ones of single element analysis. The reason may be due to the difference in convergence speed due to the selection of yield function. The difference between DP780 and STS is the exponent of the anisotropic yield function. Therefore, the degree of nonlinearity in the non-quadratic yield function may bring different numerical accuracies in calculating numerical derivatives.

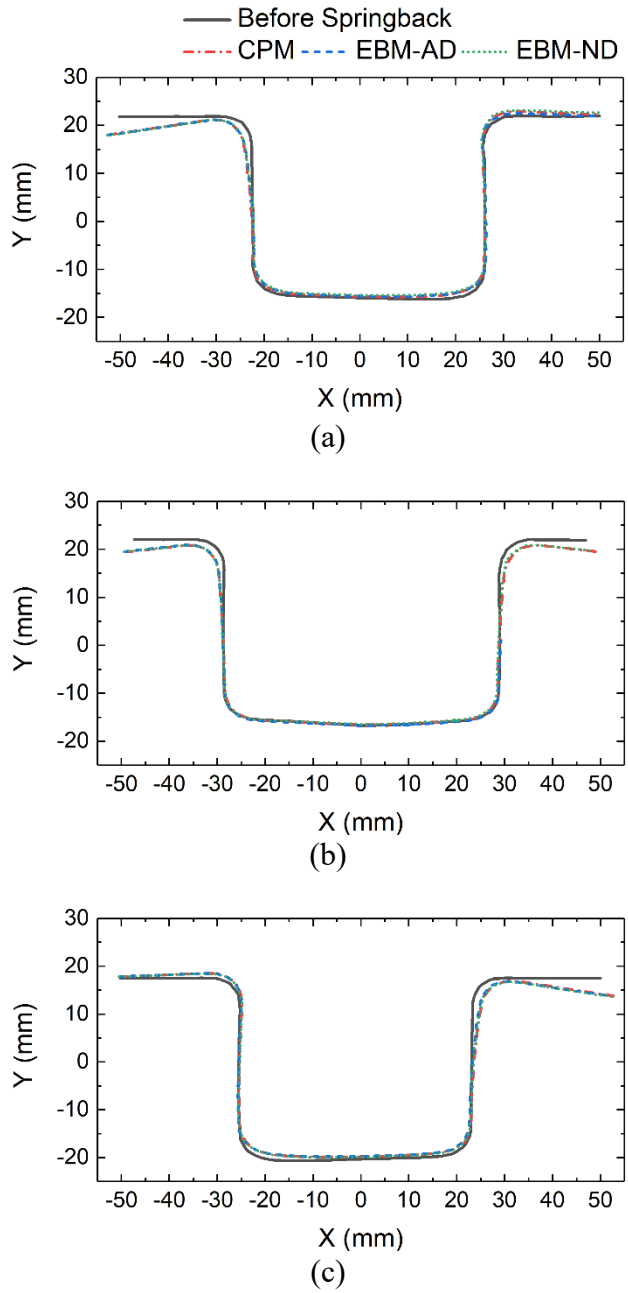

Figure 3.17. Springback results of DP780 at (a) section A, (b) section B and (c) section C.

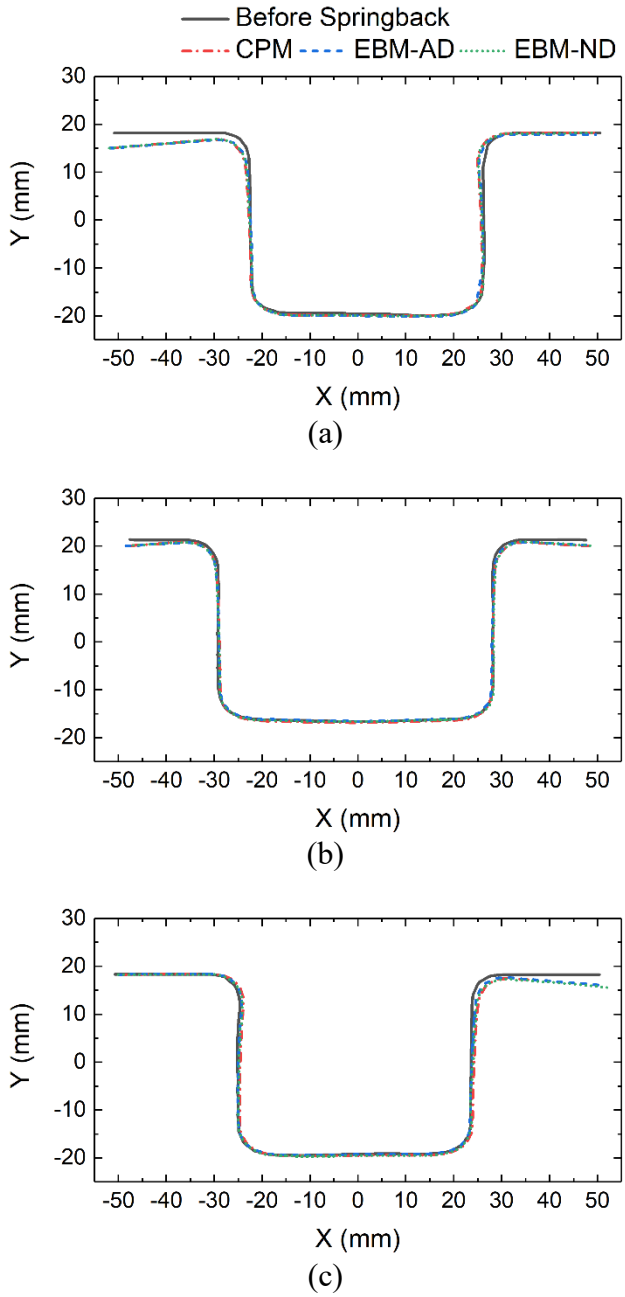

Figure 3.18. Springback results of STS at (a) section A, (b) section B, and (c) section C.

Table 3.8. The averaged equilibrium iteration number, the averaged time increment, and the relative wallclock time during the forming step.

Algorithm	Average equilibrium iteration number		Δt_{avg}		Relative wallclock time	
	DP780	STS	DP780	STS	DP780	STS
CPM	13.42	13.71	1.21×10^{-3}	5.62×10^{-4}	1.0	1.0
EBM-14R/AD	9.47	12.72	2.23×10^{-3}	1.10×10^{-3}	0.59	0.57
EBM-14R/ND	9.90	12.53	2.26×10^{-3}	1.12×10^{-3}	0.84	0.54

3.6. Summary

In this study, a fully implicit stress integration algorithm is developed for the enhanced version of the HAH model, which is capable of reproducing the cross-hardening and softening under complex loading path changes by introducing the distortional hardening concept. Particularly, the proposed algorithm solves for the complete set of residuals defined from the HAH model in the context of the Euler backward method (EBM). The major difference between the developed model and other previous stress integration algorithms can be summarized as follows.

- The developed EBM algorithm is formulated based on a total of 14 residuals for stress tensor, microstructure deviator tensor, and the whole state variables associated with the HAH model. On the contrary, the previous algorithms for the HAH models introduced a partially implicit scheme by considering a limited number of residuals for the simplicity of modeling. This leads to unstable and inaccurate evolutions of plastic state variables related to the distortions of yield function at loading path changes.

- For calculating the first and second derivatives of yield surface, which are inevitably required in the formulations of common predictor-corrector numerical schemes, the present model provided both analytical (EBM-AD) and finite difference-based numerical methods (EBM-ND). The analytical expressions of the HAH yield surface are given in the appendix.

The accuracy and robustness of the developed algorithm and implementation were validated by one-element analysis and a large-sized industrial problem. For the one-element analysis, the compression-tension test and compression-cross tension test were conducted for two representative materials. For the large-sized problem, the S-rail benchmark forming and

springback simulations were conducted. The summary of the validations is presented as follows.

- The semi-explicit CPM and the implicit EBM with partially introduced residuals (EBM-4R) resulted in abnormal evolution of stress-strain curve or r-value for both reversed and cross-loading conditions when the strain increment became larger. In contrast, the fully implicit with the complete set of residuals (EBM-14R) showed stable and accurate results regardless of investigated strain increments. Moreover, with the EBM-14R algorithm, both methods based on analytical and numerical derivatives provided virtually the same accuracy.

- For the cross-loading path, the ignorance of the residuals for the evolution of the HAH yield surface led to the abnormally wrong rotation of the microstructure deviator $\mathbf{h}^{s}$, which brought about undesirable evolutions of other state variables. This justifies the better accuracy and robustness of the present fully implicit algorithm based on full consideration of residuals of the HAH model.

- For the S-rail forming and springback, the investigated algorithms

were all successful without divergence even with static implicit solver and complicated HAH model. However, the EBM-based algorithms required less computational time than the CPM. This is due to the smaller time step determined from the automatic time increment resulted from the non-consistent tangent modulus of the CPM algorithm.

- Noticeable differences in averaged time increments and the equilibrium iteration number were obtained between the EBM-AD and EBM-ND in the S-rail forming simulations. But, the yield surface exponent, which determines the sharpness of the non-quadratic yield function at the bi-axial stress state, played as a more dominant factor for the computation cost for the numerical derivative-based EBM algorithm.

4. Anisotropic strengths prediction of steel plate after prior bending-reverse bending deformation

4.1. Experiments

In this study, a carbon steel plate made of SNT355 with a thickness of 6.6 mm was investigated. This material has been used for manufacturing structural pipes and its chemical composition is listed in Table 4.1. The material has been used for manufacturing structural pipes. Owing to its low carbon concentration, the material exhibits yield point elongation in a uniaxial tension test. All experiments on the material characterization and the bending/reverse-bending (BRB) were conducted using an Instron 8801 universal testing machine (10 tons). Strain distributions were measured using digital image correlation (DIC) and VIC-3D software.

Table 4.1. Composition of SNT 355 carbon steel specimens.

	C	Si	Mn	P	S	N
Weight (%)	<0.22	< 0.55	< 1.60	< 0.030	< 0.015	< 0.006

4.1.1. Uniaxial tension and disk compression tests

Uniaxial tension tests were conducted to measure the basic elastic-plastic properties and anisotropy of the investigated material. In addition, a special disk compression test was additionally conducted to obtain an equi-biaxial flow stress curve and plastic anisotropy. Tensile tests were conducted at 0° (TD), 45° (DD), and 90° (RD) from the reference direction, which corresponds to the transverse to the rolling direction of the plate. The specimen geometry used for the tensile test is presented in Figure. 4.1. All tests were conducted under quasi-static conditions with a strain rate of 1×10^{-3}/s. The Lankford coefficients (or r-value) were also measured from the tensile test along the three orientations.

The disk compression test was conducted by compressing a 12-mm diameter disk (Figure 4.2(a)) along the thickness direction. Aerosol-type graphite was applied to the specimen surface to reduce friction between the specimen and tool. An engineering strain, defined as $(X_0 - X)/X_0$, was measured using the initial X_0 and current distance X, marked in the testing jig displacement using the DIC technique (Figure 4.2(b)). The measured stress-strain curves are shown in Figure. 4.3, and their values are summarized in Table 4.2. Note that the stress-strain curves show obvious upper and lower

yield points, particularly in the uniaxial loading along the 0° direction and in the disk compression tests. In addition, planar anisotropy was observed in both the stress and r-value but was more pronounced in the r-values.

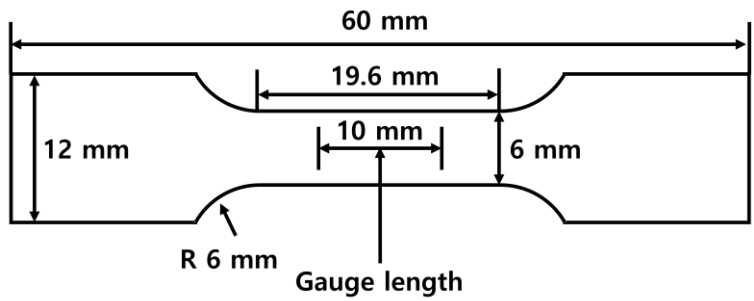

Figure 4.1. A tensile test specimen with dimensions.

(a)

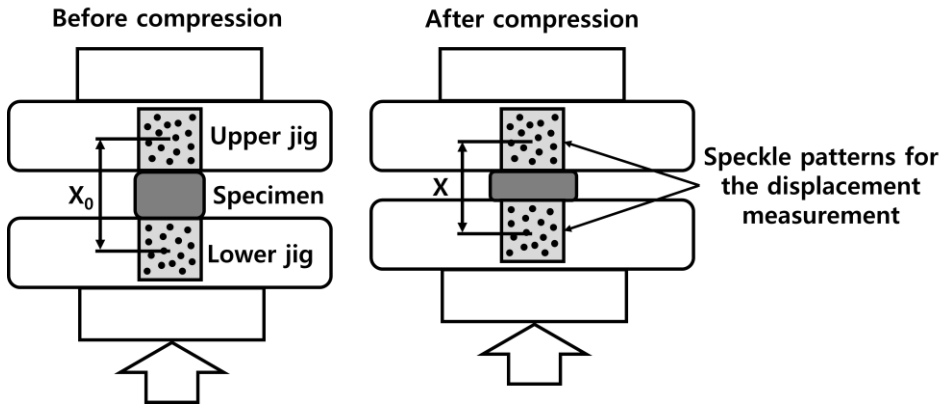

(b)

Figure 4.2. (a) A tensile test specimen with dimensions, (b) schematic illustrations for the disk compression test.

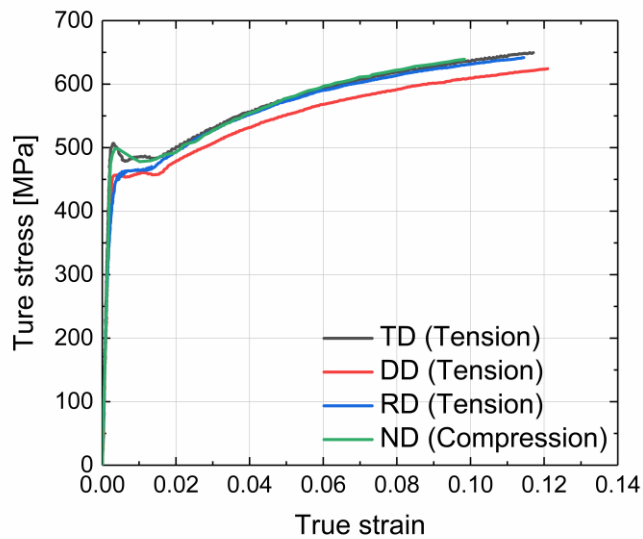

Figure 4.3. Measured uniaxial tensile stress-strain curves along 0° (TD), 45° (DD), and 90° (RD). Besides, the flow stress curve of disk compression along the material normal direction (ND) is also presented.

Table 4.2. Basic mechanical properties of SNT 355.

Loading	Young's modulus [GPa]	Upper yield strength [MPa]	Lower yield strength [MPa]	Tensile strength [MPa]	Uniform elongation [mm/mm]	r-value
Tensile 0°	207	495.5	477.7	575.5	0.124	0.769
45°		-	456.1	553.3	0.129	0.939
90°		-	462.5	574.3	0.123	0.5
Compression		500.1	479.5	-	-	-

4.1.2. Tension-compression-tension test and two-step tension test

To characterize the anisotropic hardening under a load reversal condition, a continuous tension-compression-tension (TCT) test was conducted. To avoid a non-uniform deformation caused by the Lüders band propagation [43] at an early strain of approximately 1.4%, the magnitudes of the pre-strain were set as 3% and 4%. Approximately 2% compression was applied after each pre-strain and then followed by tension up to specimen rupture. The same specimen configurations were applied for the TCT test as for the uniaxial tensile test. The same specimen as applied in the uniaxial tensile test was used for the TCT test.

Two-step tension (TT) tests were conducted to identify the cross-loading response of the material. First, a large-sized specimen (shown in Figure. 4.4(a)) was prepared with reduced thickness from the as-received specimen (owing to the load limit of the tensile test equipment) using electrical discharging machining. During the first loading step, 3% and 4% pre-strains were applied to the large-sized specimens. Then, small-sized specimens (as shown in Figure. 4.4(a)) 45 ° and 90° from the reference directions were taken from the pre-tensioned large-sized specimen. The strain was measured within the gauge length shown in Figure. 4.4(a) using the DIC technique. The strain

distribution of the large-sized specimen is reasonably uniform, as shown in Figure. 4.4(b).

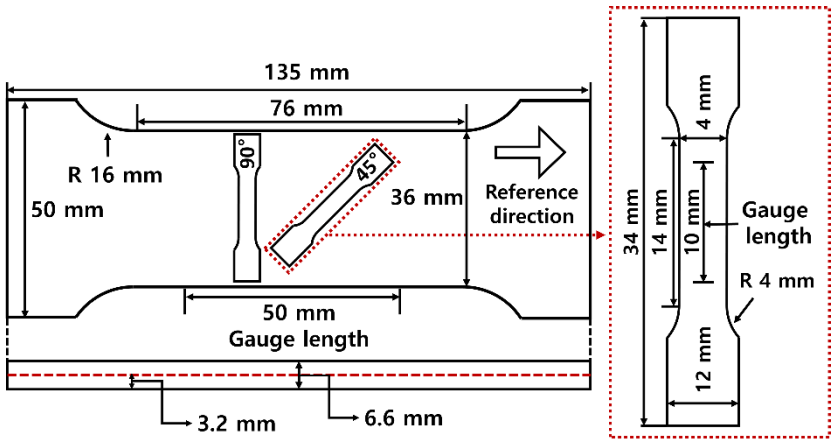

(a)

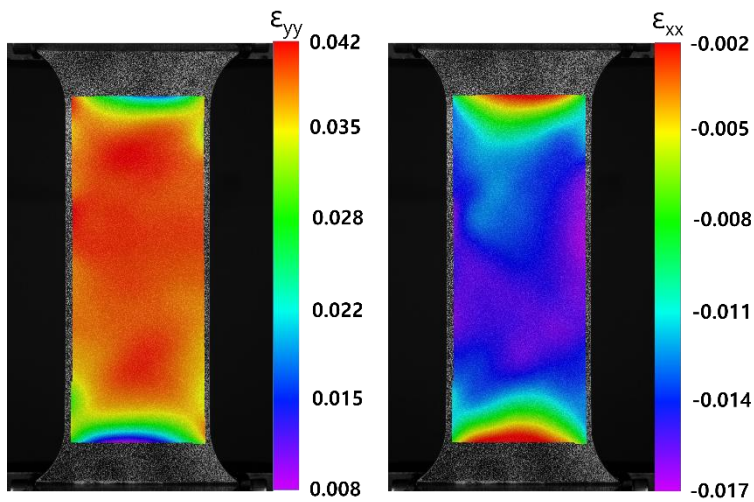

(b)

Figure 4.4. (a) Sub-sized specimens taken from a large-sized specimen for the two-step tension test, and (b) example strain distributions of the large-sized specimens.

4.1.3. Bending-reverse bending (BRB) test

A four-point bending-reverse bending (BRB) test was employed in this study to replicate the strain path change in the pipe (or tube) formation. The experimental setup of the BRB test is shown in Figure. 4.5(a) and (b). The strain measurement area was chosen at the center of the plate, as shown in Figure 4.6, and the DIC was used to obtain the strain distribution. The dimensions of the bending specimen and span distances are shown in Figure. 4.6. The deflection during the bending test was controlled using an extensometer (Figure. 4.5(b)).

In Figure. 4.7(a), the BRB test procedure is presented. The same number marked in the specimens symbolizes the same specimen. The test consists of bending, (first) unloading, reverse bending, and (second) unloading, which is schematically shown in Figure. 4.7 (a)–(d), respectively. After the first unloading (Figure. 4.7 (b)), the shape of the specimen was scanned to measure the amount of springback. Then, the unbent specimen was reversed, bent again, and unbent to obtain the final flattened specimen (Figure. 4.7(c)–(d)). The applied deflections for the initial bending and reverse bending were 27.0 and 26.8 mm, respectively.

Upon completing the BRB test, uniaxial tensile specimens were taken out

from the region between two inner pins, as shown in Figure. 4.7(e). Uniaxial tensile tests at 0°, 45°, and 90° from the reference direction were conducted to measure the strengths after the BRB test.

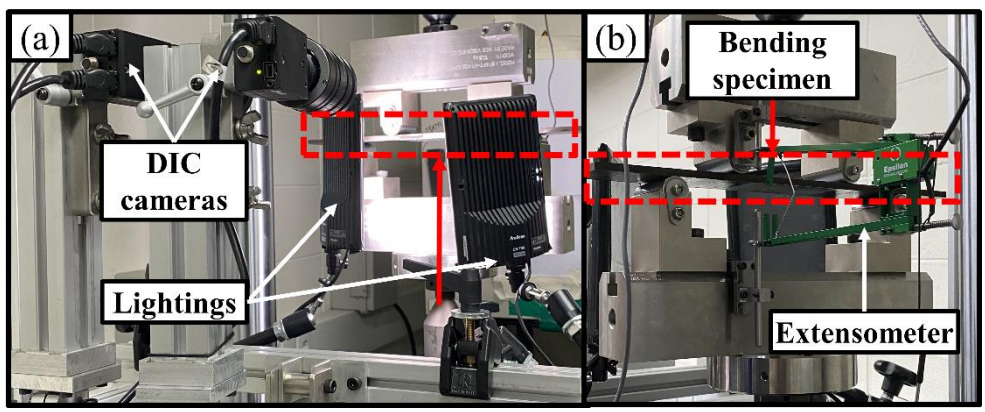

Figure 4.5. Experimental setup for a bending/reverse bending (BRB) test: (a) front side view, (b) backside view.

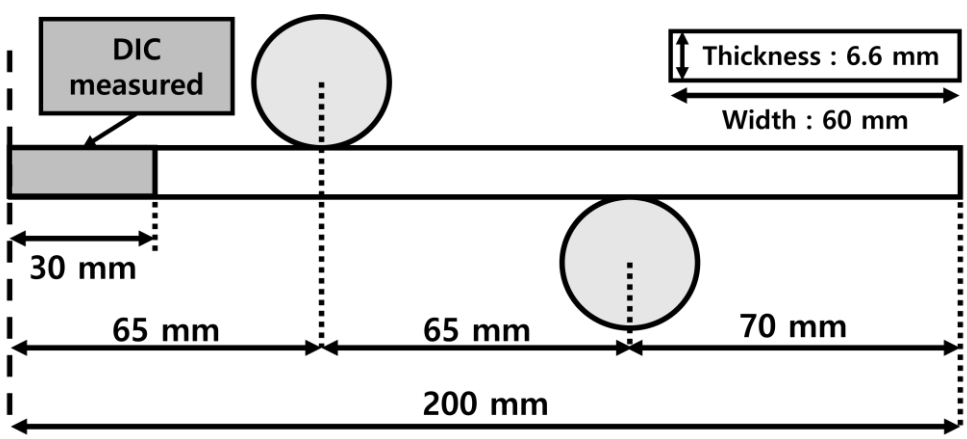

Figure 4.6. Test dimensions of the bending/reverse bending (BRB) test.

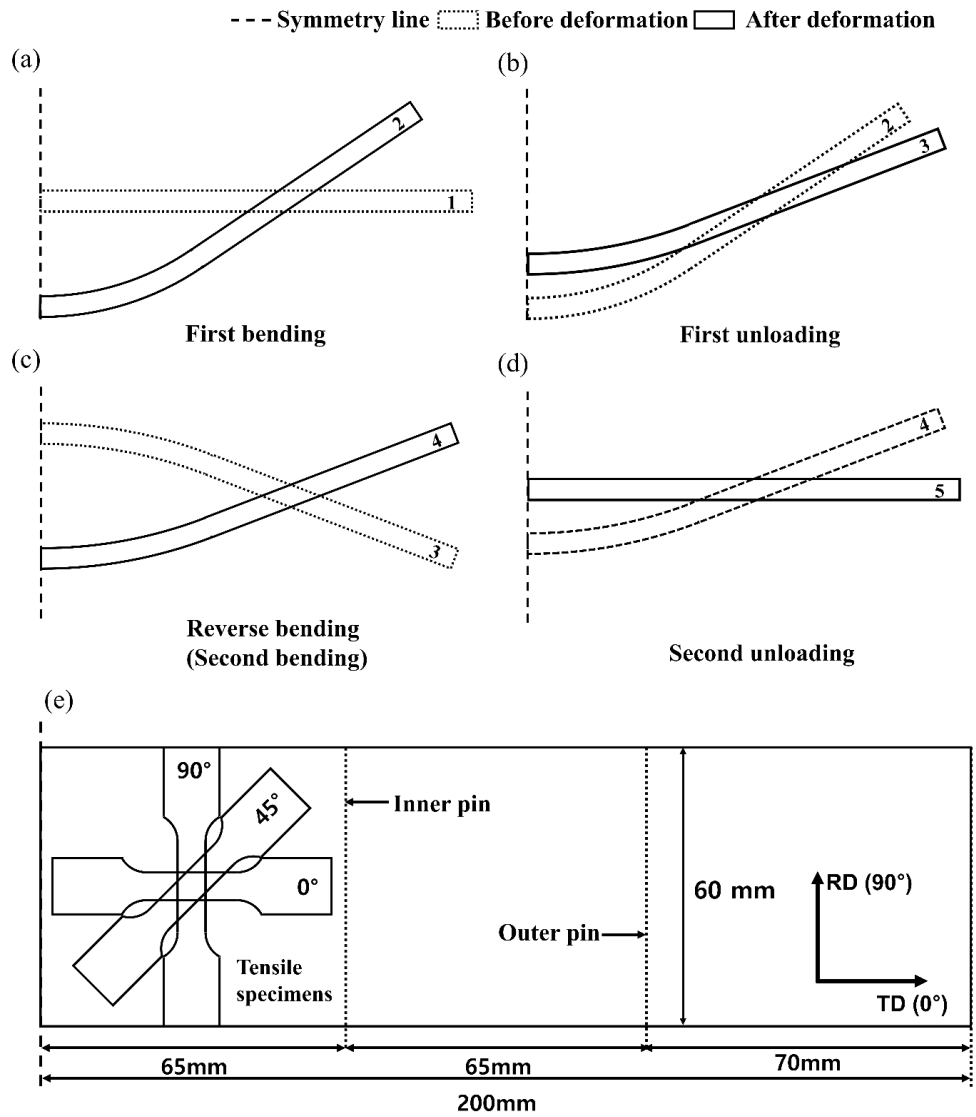

Figure 4.7. Schematic illustration of the BRB test: (a) bending, (b) first unloading, (c) reverse bending, (d) second unloading, and (e) locations of tensile specimens taken out from the BRB test specimen.

4.2. Material modeling

4.2.1. Plastic anisotropy

For the plastic anisotropy of the initial (as-received) plate, Hill's 1948 yield function [74] was implemented.

$$\phi(\boldsymbol{\sigma}) = \sqrt{\begin{matrix} F\left(\sigma_{yy}-\sigma_{zz}\right)^2 + G\left(\sigma_{zz}-\sigma_{xx}\right)^2 + H\left(\sigma_{xx}-\sigma_{yy}\right)^2 \\ +2L\sigma_{yz}{}^2 + 2M\sigma_{zx}{}^2 + 2N\sigma_{xy}{}^2 \end{matrix}} . \tag{4.1}$$

where F, G, H, L, M, and N are the coefficients of anisotropy, and the subscripts x and y represent 0° and 90° to the rolling direction, respectively. The anisotropic coefficients were identified from the directional differences in yield strengths and the biaxial stress measured from the disk compression stress. The yield stresses were determined after removing the unstable region of yield point elongation. Note that the coefficients L and M were assumed to be 1.5, which corresponds to the isotropic condition of the through-thickness stress components. It is a reasonable assumption because the major deformation mode of the BRB and subsequent tension is not much associated with the through-thickness deformation. There have been studies applying the same assumptions in the literature [75, 76] for the prediction of sheet plastic anisotropy. The other coefficients are listed in Table 4.3 and the yield function is represented in Figure 4.8. with von-Mises criterion.

Table 4.3. Hill 1948 anisotropy coefficients.

F	*G*	*H*	*L*	*M*	*N*
0.5041	0.4899	0.5101	1.5	1.5	1.669

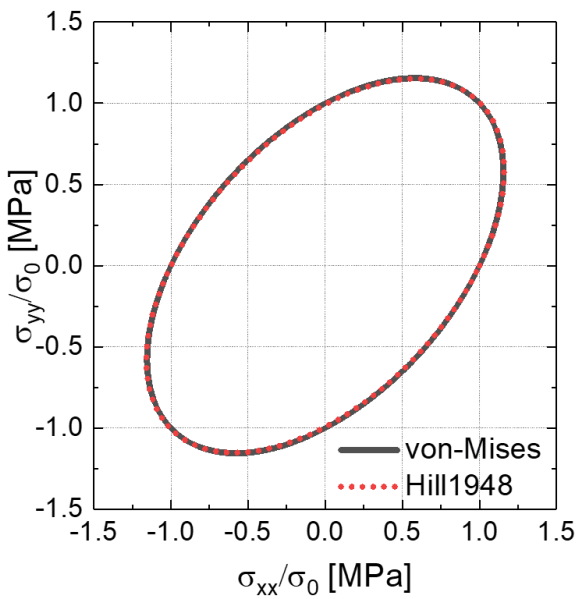

Figure 4.8. Identified Hill1948 and von-Mises yield locus.

4.2.2. Apparent elastic chord modulus

Many studies reported that the modulus of elastic unloading or reloading decreased after applying prior plastic deformation. The variation of the modulus has been explained and modeled by continuum damage mechanics [77-84]. But, in this study, the simplified chord modulus approach based on dislocation-based anelasticity [85,86] was employed because it has been preferred in the modeling of sheet metal forming process, especially for springback simulations [16, 44, 46, 87-93].

$$E\left(\bar{\varepsilon}\right) = E_0 - \left(E_0 - E_a\right)\left\{1 - \exp\left(-\xi\bar{\varepsilon}\right)\right\}. \tag{4.2}$$

where E_0 and E_a represent the initial Young's modulus and a saturated chord modulus after a prior equivalent plastic strain, respectively. In addition, ξ is a material constant. The material parameters for the investigated material were E_a =170.5 GPa and ξ =234.2, which were determined by fitting the unloading and reloading curves of the TCT tests. The degradation of the chord modulus according to Eq. (4.2) is shown in Figure 4.9. It is shown that approximately 18% of the initial elastic modulus decreased at a plastic strain of less than 5%, which is important for the simulation of elastic unloading.

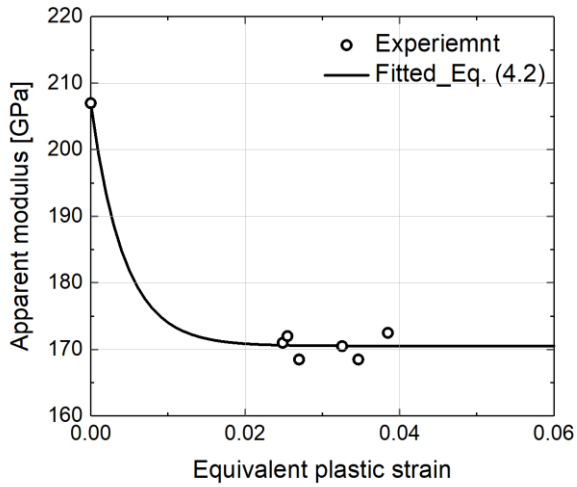

Figure 4.9. The apparent elastic modulus measured as a concept of chord modulus.

4.2.3. Monotonic stress-strain curve (without strain path change)

To accurately capture the hardening behavior of SNT355 steel at lower strain, the yield point elongation was modeled using a simple law. The hardening law combines perfect plasticity with a lower yield point (σ_y) and a typical monotonic hardening law (σ_H) and written as

$$\bar{\sigma}\left(\bar{\varepsilon}\right) = R\left(\bar{\varepsilon}\right)\cdot\sigma_y + \left\{1 - R\left(\bar{\varepsilon}\right)\right\}\cdot\sigma_H . \tag{4.3}$$

$$R\left(\bar{\varepsilon}\right) = 0.5 - \frac{1}{\pi}\arctan\left(\xi_L\left(\bar{\varepsilon} - \bar{\varepsilon}_L\right)\right). \tag{4.4}$$

where $R\left(\bar{\varepsilon}\right)$ is newly proposed to approximate a step function at $\bar{\varepsilon}=\bar{\varepsilon}_L$. Here, ξ_L determines the slope of the step, $\bar{\varepsilon}_L$ is an equivalent plastic strain where the yield phenomenon ends and σ_{H} represents a common monotonic strain-hardening law without instability. In this study, a combined Swift-Voce hardening law was used to accurately reproduce the flow stress curve.

$$\sigma_{\mathrm{H}}\left(\bar{\varepsilon}\right)=W\cdot K_S\left(\varepsilon_0+\bar{\varepsilon}\right)^n+\left(1-W\right)\left(K_V-Q\cdot\exp\left(-\beta\cdot\bar{\varepsilon}\right)\right). \tag{4.5}$$

where W, K_S, ε_0, n, K_S, Q, and β are the material constants. On the right-hand side, the first and second terms contribute to the power-law and saturation-type hardening behaviors, respectively, and their weight is determined by a constant W. Using Eq. (4.5), the fitted hardening curve is shown in Figure 4.10, which presents an extremely high correlation with the experiment within the entire measured deformation range. The identified monotonic hardening parameters are listed in Table 4.4. The isotropic part of the HAH model corresponds to the isotropic hardening (IH) and their model parameters are identical. The HAH model converged to the IH model when only monotonic loading is considered. Interested readers can refer to the previous article by Barlat et al. [37-39].

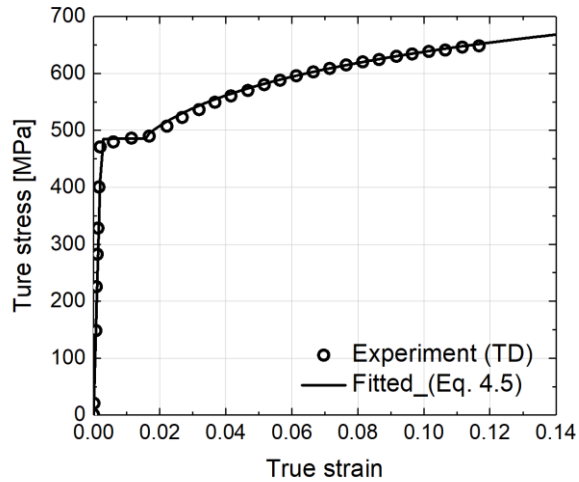

Figure 4.10. The comparison of plastic hardening curve between measured and fitted values.

Table 4.4. Coefficients for the monotonic hardening curve (Eq. (4.5))

Isotropic hardening (IH) coefficients						
ξ_L	$\bar{\varepsilon}_L$	σ_y [MPa]	W	K_S [MPa]	ε_0	n
				881.4	1.04×10^{-4}	0.1432
				K_V [MPa]	Q[MPa]	β
15000	0.0142	479.616	0.9514	769.9	536.0	42.23

4.2.4. Anisotropic hardening behaviors under strain path changes

In this section, the anisotropic hardening behaviors are modeled using the distortional HAH model with newly proposed multi-component evolution laws. The model parameters were calibrated using experimentally measured TCT and TT test results (see Chapter 4.1.2 and 4.1.3). In addition, for comparison purposes, other widely used hardening models were also considered. The comparisons include the classical isotropic hardening (IH) and isotropic–kinematic hardening (IKH) models. Note that the isotropic hardening law can be simply obtained by turning off all anisotropic hardening-related terms in the investigated HAH model. However, the IKH model has a back stress concept, similar to the concept of the microstructure deviator, which translates the yield surface. A brief summary of the IKH model is provided in Appendix D. To achieve sufficiently high accuracy in the monotonic and reverse loading conditions between the HAH and IKH models, the IKH with three back stress components was employed in this study. Then the distinctive predictive ability of other more complex loading paths, the TT tests, is studied among different hardening models. The identified anisotropic hardening parameters are listed in Table 4.5.

The anisotropic hardening coefficients of IKH (C_i, γ_i with $i = 1–3$) and HAH model (R_i, $k_{1,j}$, $k_{2,j}$, k_3, k_4, and k_5 with $j = 1–2$) were calibrated by

applying a best-fitting procedure using the TCT curves. Moreover, the coefficients k, L, k_L, C, and k_C, which are related to the cross-loading behavior, were identified from the TT tests. Note that the IKH model does not have parameters for the cross-loading condition, while they are predicted using the calibrated parameters from either reverse or cross-loading data. In general, kinematic hardening models have been calibrated based on reversed loading conditions.

The TCT stress-strain curves are predicted by the three hardening laws for 3% and 4% pre-strains in Figure 4.11(a) and (b), respectively. As shown in the figures, all hardening laws perfectly fit the monotonic stress-strain curves. However, the IH model over-predicts the flow stresses after the loading direction is reversed. By contrast, both kinematic hardening (IKH) and distortional hardening (HAH) models could predict the reversed stress-strain curves with virtually identical accuracy.

Figure 4.11 shows stress-strain curves of TT loadings with different pre-strains of large-sized tensile specimens. For the tension tests at 45°, as shown in Figure 4.12(a), experiments showed lower yield stresses in the second loading than the stress before unloading from the first tensile tests. Then, flow stresses saturated rapidly to the monotonic tensile curve as the deformation proceeded. As expected, the stress-strain curve predicted by the IH model

recovered the monotonic curve owing to its isotropic yield surface expansion. In the case of the IKH model, it captured the lowered yield stress in the second loading, but the magnitude was quite under-estimated. Contrary to the two conventional models, the distortional hardening-based HAH model with cross-loading related evolution laws could reproduce the cross-softening of the second tensile loading with significantly improved accuracy.

For the second tension 90° from the first loading, the flow stress also exhibited a cross-softening but did not converge to the monotonic stress-strain curve within the measured region. Similarly, the IH model could not produce softening of the second loading curve, and the IKH model significantly underestimated it. Again, the HAH model could only predict the softened flow stress under the cross-loading condition.

Table 4.5. Coefficients for the iso-kinematic hardening and HAH model

Isotropic-kinematic hardening (IKH) coefficients						
C_1 [MPa]	γ_1	C_2 [MPa]	γ_2	C_3 [MPa]	γ_3	
19500	201.5	1528.0	16.5	740.8	5.5	
HAH coefficients (with q = 2)						
k	R_1	R_2	$k_{1,1}$	$k_{1,2}$	$k_{2,1}$	$k_{2,2}$
9.65	0.65	0.35	355.7	16.4	132.5	81.5
k_3	k_4	k_5	L	k_L	C	k_C
0.41	1.0	0	1.0	0	0.85	42.5

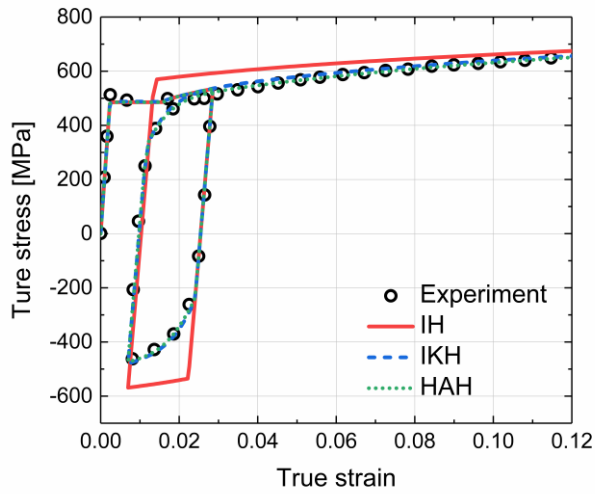

(a)

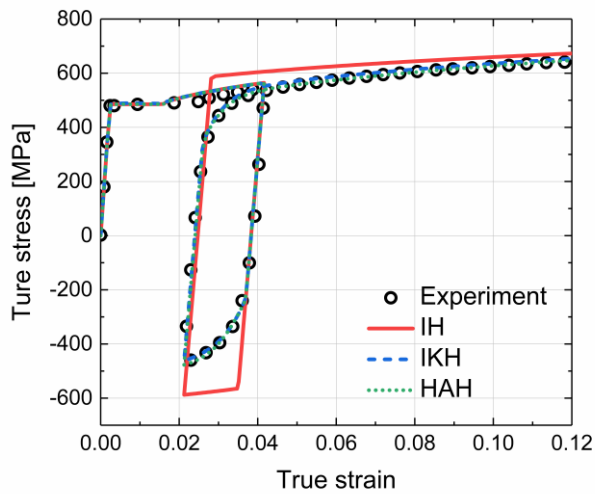

(b)

Figure 4.11. Predicted TCT stress–strain curves by IH, IKH, and HAH models: (a) Tension 3% + Compression 2% + Tension and (b) Tension 4% + Compression 2% + Tension.

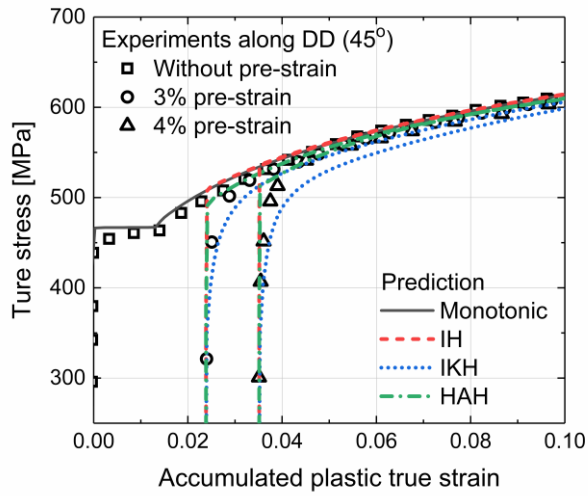

(a)

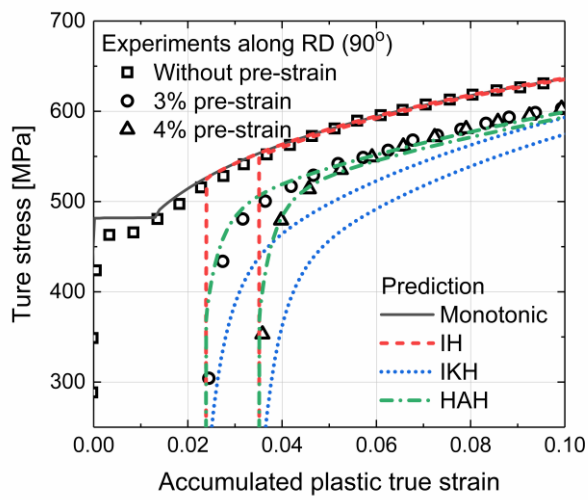

(b)

Figure 4.12. Predicted stress-strain curves of two-step tension for pre-strains using IH, IKH, and HAH models: (a) 45° tension and (b) 90° tension after 0° tension.

4.3. Strength prediction of the plate after bending-reverse bending

As an example of a pipe formation, a four-point bending test and simulation were utilized for the validation of the proposed material modeling. To summarize, bending represents the formation of a pipe using a planar plate, and reverse bending is used for the flattening process before the tensile test. For the finite element (FE) simulation of the BRB test and the tensile tests for the strength prediction, Abaqus/standard finite element software was used with the implementation of HAH and IKH models in the user material subroutine, UMAT.

The simulation consists of a BRB step and a subsequent tensile test step. The BRB step involved bending, unloading, reverse bending, and unloading processes, and tensile tests were conducted along three different material orientations. Figure 4.13(a) shows the test specimens taken from the BRB specimens in the experiment, and those for the FE simulations are shown in Figure 4.13(b). Sub-sized specimens at 45° were removed from the large-sized specimen A, and 0° and 90° specimens were removed from the large-sized specimen B, as shown in the figure.

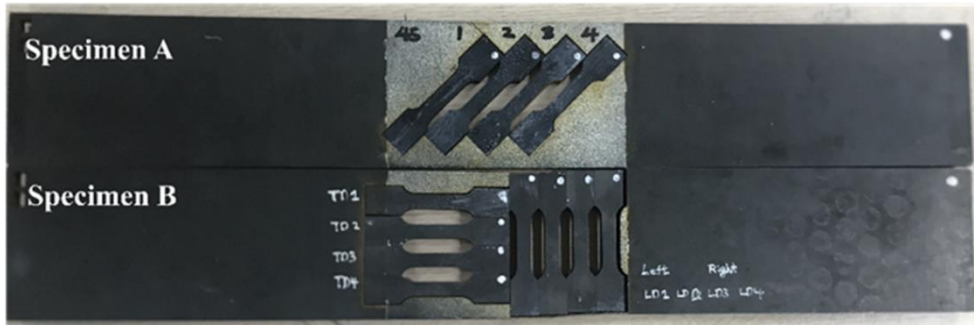

(a)

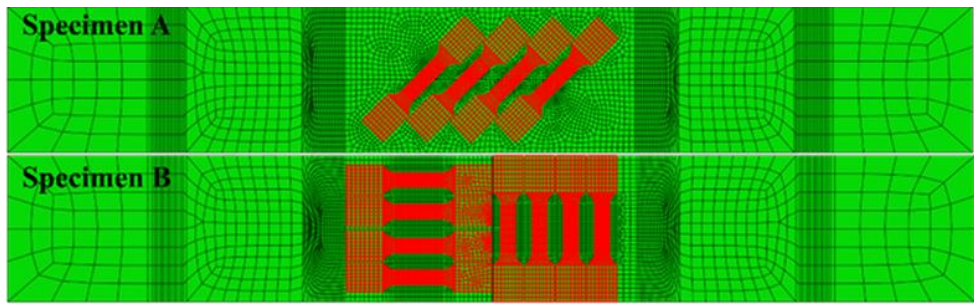

(b)

Figure 4.13. (a) Tensile specimens for measuring strengths along three different material orientations and (b) the corresponding FE simulation models for BRB and tensile tests.

In the FE models, mixed eight (C3D8R) and four-node (C3D6) continuum elements were used as the plate material, and the analytical rigid surface element was used for modeling the pins. There were nine elements throughout the thickness of the specimen. The friction between the plate and rigid pin was 0.12, which was determined by comparing the simulated bending strains with those of the experiments. Figure 4.14(a) shows the distribution of the longitudinal strain measured from the side of the bending specimen with the DIC technique. Note that the strain at the edge region is missing owing to the experimental limitation of the current DIC measurement. After reconstructing the strain distribution at the edge region using an FE-like interpolation scheme [94], the strain distribution can be obtained for the entire thickness region, as shown in Figure 4.14(b). The friction coefficient was then iteratively determined until the simulated strain distribution matched the experimental value (Figure 4.14(c)).

Figure 4.15 shows a comparison of the FE calculated shapes of the plate specimen after the first bending and unloading using IH, IKH, and HAH models with the experimental profile. It is shown that all three hardening models show good agreement with the measured springback profile. This result is well expected because the major deformation mode is monotonic, which can be captured even by isotropic hardening (IH) and the three models

result in virtually the same result. Figure 4.16(a) and (b) show the calculated reaction force-displacement curves after the first bending and subsequent reverse bending. Again, the three models could predict the force curve with good agreement because the deformation does not involve any remarkable change in the strain path. However, in the reverse-bending case, the IH model significantly over-predicted the force whereas the IKH and HAH models showed extremely good agreement with the experiment. This is because in the reverse bending, the material experiences prior plastic deformation in the first bending, which represents the loading-reverse loading path. Since only IKH and HAH models could calibrate the tension followed by compression (or vice versa), the reduced punch (pin) load during reverse bending could be well predicted.

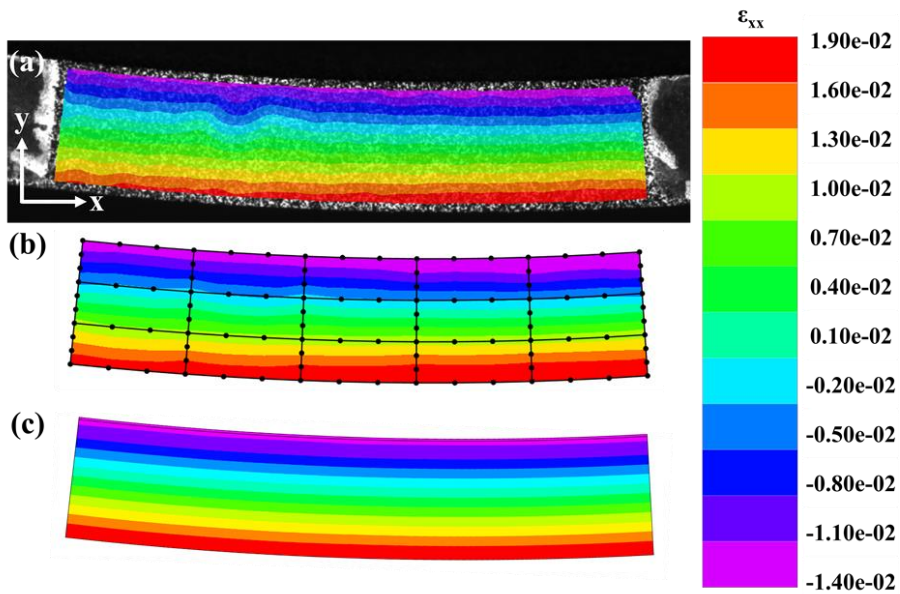

Figure 4.14. Longitudinal strain distribution viewed from the side of the bending specimen. (a) DIC measured strain contour, (b) reconstructed strain field, and (c) FE simulated strain field with optimized friction coefficient.

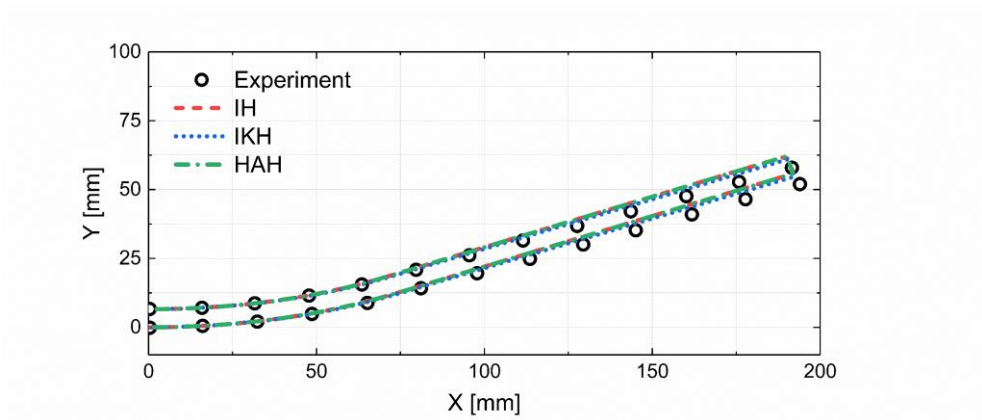

Figure 4.15. Comparison of FE calculated deflection of the plate after first bending and unloading, i.e., springback profile.

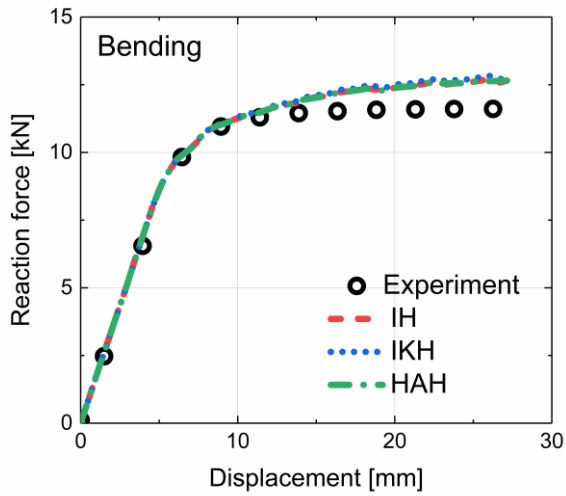

(a)

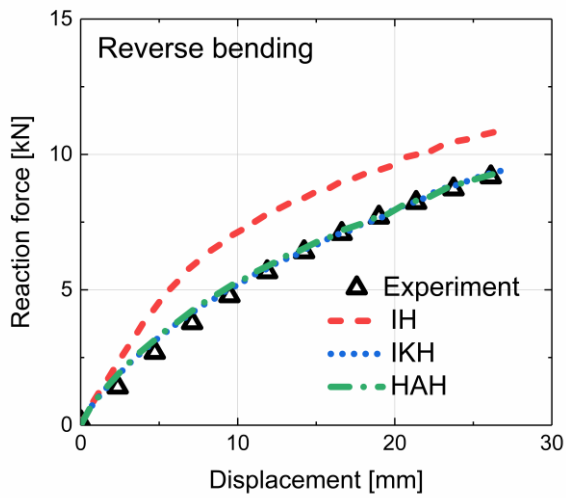

(b)

Figure 4.16. Comparison of FE calculated (a) punch reaction force-displacement curves during bending, and (b) reverse bending with three hardening models.

Figure 4.17-4.19 shows the engineering stress-strain curves of the specimens after the BRB test. As already mentioned in Chapter 4.1.3. these samples experienced prior bending and reverse bending (with elastic unloading). Therefore, this test corresponds to the evaluation of the model prediction for the strength of the material after the loading path changes. For the FE simulations, the IH, IKH, and HAH were compared with experimental curves measured from three different material orientations. Figure 4.17-4.19(a) present the stress-strain curves of the 0°, 45°, 90° specimens, Figure 4.17-4.19(b) are their respective close-up figures within the small strain range. The measured stress-strain data were obtained from at least four tests and each representative curve was provided in the figures. In addition, for a detailed comparison, the yield and tensile strengths are summarized in Table 4.6 as well. In the table, the relative errors of the simulated values from the experimental data are presented using the equation, $Error\,(\%) = \frac{\sigma_{\text{pre}} - \sigma_{\text{exp}}}{\sigma_{\text{exp}}} \times 100$. Here, σ_{pre} and σ_{exp} are the predicted and measured strengths, respectively.

The experimental data did not show noticeable upper yield points for all curves of the material orientations, but the yield plateaus up to a 1.25% strain could still be observed. Moreover, the BRB plate showed a much lower yield

strength of the 0° specimen than the material before BRB loading, that is, 477.7 versus 433.6 MPa (see Table 4.6). Interestingly, the yield strengths of the other two oriented specimens along the 45 ° and 90° directions were similar. The FE simulation results showed that the classical IH model over-predicted the yield stresses in all directions. In particular, the yield strength of the 0° specimen had an error of over 15% compared to the experiment. However, even the IH model could predict the flow stresses at a large strain, and the tensile strengths could be predicted within an error of 3%. The isotropic–kinematic hardening model or IKH could better predict the overall flow stresses along three orientations than the IH model. In particular, the large strain strength, including the tensile strength, could be predicted within an error of 1% for the 0° and 45° specimens. Because the IKH model could include the Bauschinger effect, the yield strength for the 0° specimen could be well captured from the experiment within an error of 2%. This is because the major deformation mode of BRB loading consists of load reversal at 0° from the reference direction. However, even the kinematic hardening model failed to predict the yield strengths of the 45° and 90° specimens. The relative errors were approximately over 10%. By contrast, the proposed distortional HAH hardening model could predict both the yield strength and the tensile strength in all three orientations within a 1% error. The different predictive

accuracies among the three hardening models can be well compared in the close-up Figure 4.17. Note that the IKH model significantly under-estimates the yield strength under the cross-loading history, which is because the large Bauschinger effect in the reference direction is memorized in the other two material orientations. By contrast, the HAH model has constitutive parameters that can be calibrated for the cross-loading mode independently from those for reversed loading conditions. Figure 4.17-4.19 also shows that all three hardening models failed to reproduce the yield plateau observed in the experiment. This limitation will be discussed in detail in the next section.

Table 4.6. Comparison of FE predicted and measured yield strength (YS) and tensile strength (TS) of three different oriented plates after bending-reverse bending. The percentages (%) denote relative errors between the experimental value and different hardening models.

Orient-ation	Strength	Exp. (MPa)	Relative errors (%)		
			IH	IKH	HAH
0°	YS	433.6	15.3	-1.34	0.90
	TS	582.2	1.46	0.67	0.07
45°	YS	459.4	3.94	-11.8	0.52
	TS	565.2	2.11	0.87	0.66
90°	YS	463.4	6.50	-9.82	0.41
	TS	577.5	2.60	1.41	1.07

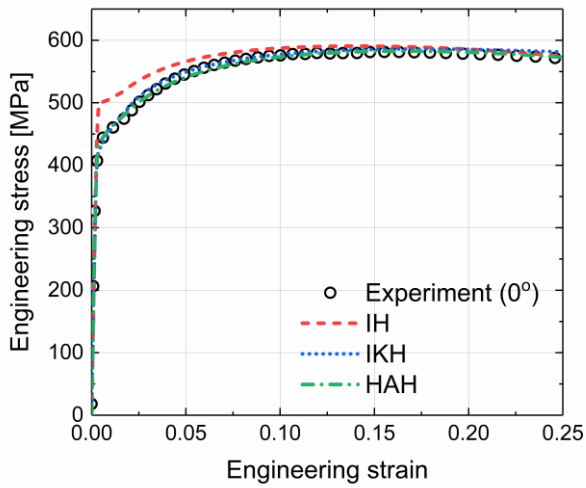

(a)

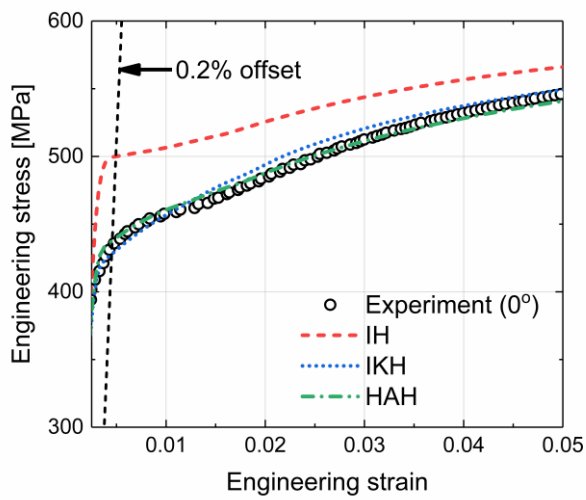

(b)

Figure 4.17. (a) Engineering stress-strain curves of specimens after BRB test along 0° direction, and (b) a magnified graph up to 5% engineering strain.

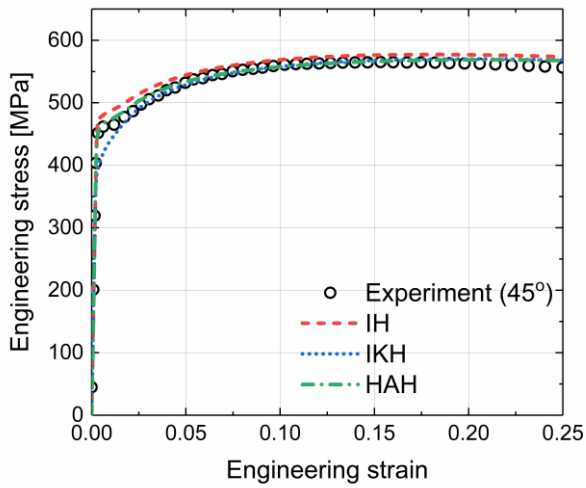

(a)

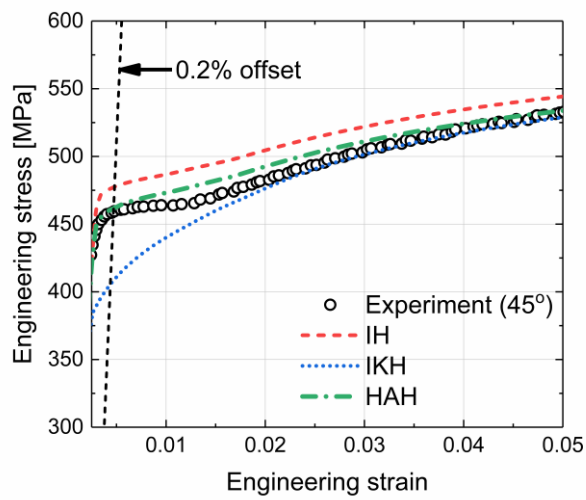

(b)

Figure 4.18. (a) Engineering stress-strain curves of specimens after BRB test along 45° direction, and (b) a magnified graph up to 5% engineering strain.

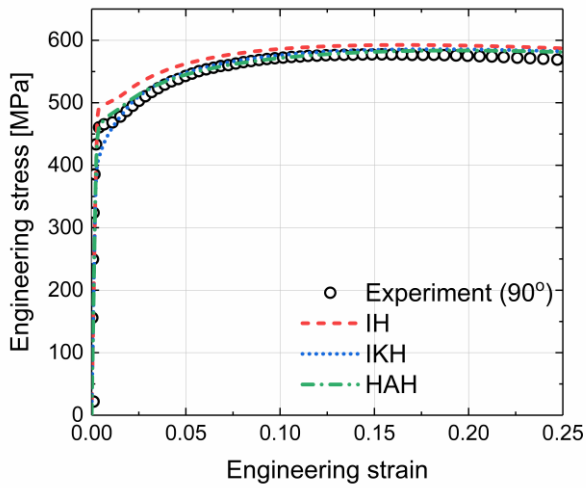

(a)

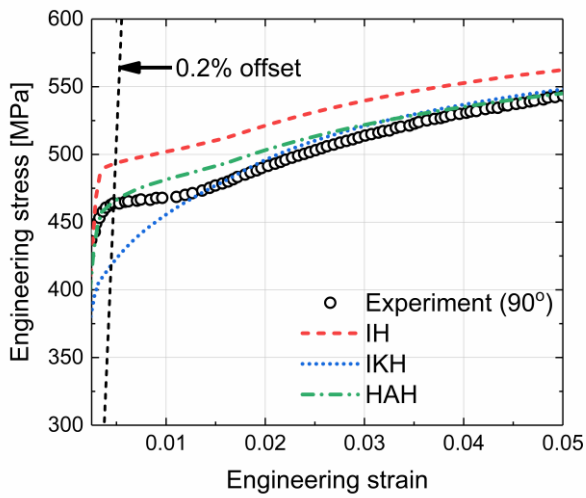

(b)

Figure 4.19. (a) Engineering stress-strain curves of specimens after BRB test along 90° direction, and (b) a magnified graph up to 5% engineering strain.

4.4. Discussion

4.4.1. Effect of hardening model

In the previous sections, isotropic hardening (IH) and two anisotropic hardening models (IKH and HAH) were implemented during the FE simulations. The predictive accuracy of each model for the tensile flow stress after bending and reverse bending (BRB) was compared with the experiment results. Three tensile orientations were considered as validation. The results showed that the anisotropic hardening models based on kinematic hardening and distortional hardening could predict the tensile flow stress well under a reverse loading path, that is, the tensile strength at 0° after the BRB. However, only the distortional hardening-based HAH model could predict the tensile strength of specimens along the 45 and 90° directions after the BRB. These two directions correspond to the near-cross-loading strain path change.

To analyze the difference in the stress state, yield surfaces are described for the three hardening models. As an example, a finite element was selected from the center of the 90° tensile specimen taken from the BRB plate. The deformation path in the selected element corresponds to the compression followed by tension before applying tensile loading for evaluation of the strength. Figure 4.20(a) and (b) represents the yield surfaces corresponding

to the onset of plastic yielding (or yield stress) and maximum force (or tensile strength), respectively. In the figures, the stress components σ_{xx} and σ_{yy} correspond to the stresses along the 0° and 90° directions, respectively. As shown in Figure 4.20(a), the area of the yield surface (or equivalent area of the elastic region) predicted by IH is the largest, which caused an over-predicted yield strength. By contrast, the stresses on the yield surfaces of IKH and HAH along the x-direction are similar; thus, their prediction of the yield strength was comparable along the 0° direction. The stresses on the yield surfaces in the y-direction are the least and largest for the IKH and IH models, respectively. The stress predicted by the HAH model is between the IH and IKH models and is close to the stress on the initial yield surface (as-received state). This is consistent with the experimental results shown in Figure 4.18(b). In Figure 4.20(b), the flow curves along the 90° direction show almost no difference among the three models. This marginal difference corresponds to insignificant differences in tensile strengths predicted by the three models (Table 4.6).

The negligible difference in strength prediction at large strain may be attributed to the small maximum bending strain of approximately 2% in this study, which is due to the limit of the machine capacity. To amplify the effect of the hardening model on the prediction of strength after cyclic bending

deformation, an additional FE simulation for the BRB test with increased deflection was performed. For this, a 54-mm deflection was applied during the first bending stage. Then, 49.5- and 51.5-mm deflections were applied to the cases of the IH and IKH (and HAH) models in the reversed bending step. The maximum bending strain in the first bending step was 4.5%. Using the deformation path, tensile loading was applied to each direction of the specimen in the FE simulation. Figure. 4.21 shows that the IH model results in significantly higher yield stress than those of the IKH and HAH models. The two anisotropic hardening models presented similar stress-strain curves along the 0° tension. Notably, the flow stresses predicted by the IKH model along the 45° and 90° tension resulted in considerable softening compared to the IH and HAH models up to a strain of 5%. Therefore, the analysis clearly demonstrates that the proper choice of hardening model can be critical for predicting the anisotropic strength of the material, which experienced prior complex loading path changes. In the present study, anisotropic hardening was employed to estimate the strengths after a reversed loading path. Moreover, the distortional hardening concept may be preferably utilized for the prediction of the yield strength under both reversed and cross-loading conditions.

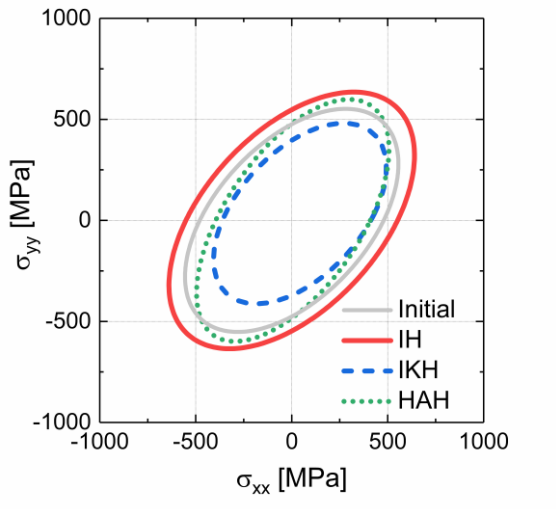

(a)

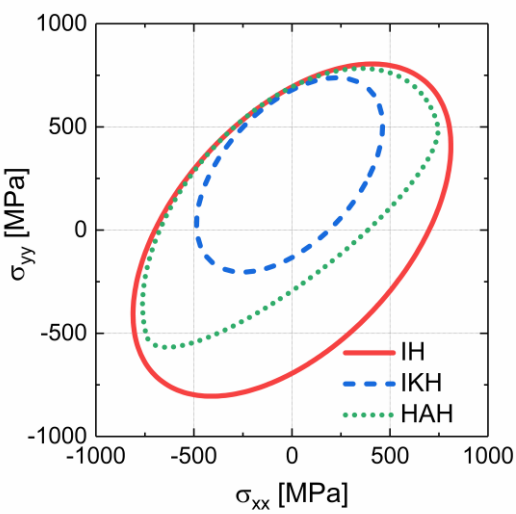

(b)

Figure 4.20. Yield surfaces predicted by IH, IKH, and HAH models at an element of 90° tensile specimen under the (a) yield point and (b) tensile strength.

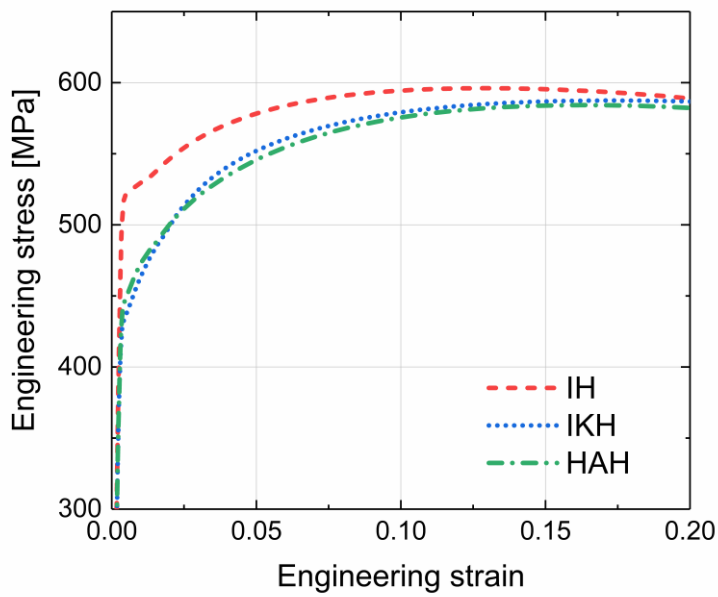
Engineering stress [MPa]
600
500
400
300
0.00
0.05
0.10
0.15
0.20
Engineering strain
IH
IKH
HAH

(a)

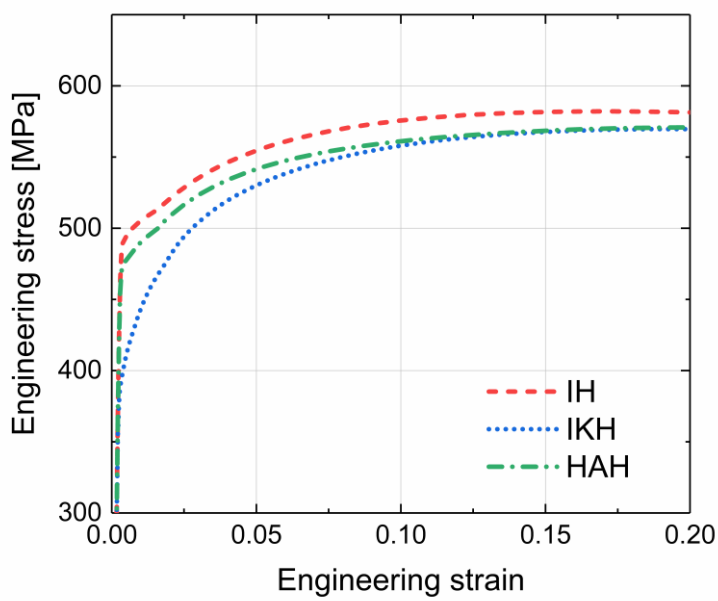
Engineering stress [MPa]
600
500
400
300
0.00
0.05
0.10
0.15
0.20
Engineering strain
IH
IKH
HAH

(b)

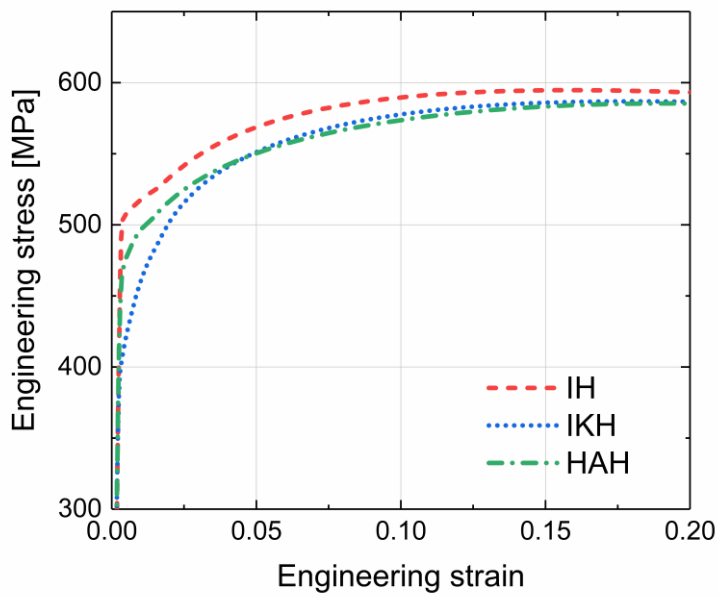

(c)

Figure 4.21. Engineering stress-strain curves predicted by different hardening models after cyclic bending with the maximum bending strain of 4.7%: (a) 0°, (b) 45°, and (c) 90° tension.

4.4.2. Effect of yield point phenomenon

The uniaxial tension and disk compression tests indicated the existence of yield point phenomenon with upper and lower yield stresses in the investigated materials. This well-known phenomenon originates from the solute interactions under the Cottrell atmosphere with dislocations in low-carbon steel. That is, the pinning and release of dislocations owing to the interstitial atoms result in the upper yield point and the subsequent stress decrease in the stress-strain curve [95,96]. There is also another different mechanism causing the yield point phenomenon. The grain boundaries of the material with ultra-fine grained microstructure trap the dislocations and this causes similar behaviors of the dislocations as they are in the Cottrell atmosphere [97-100].

Many models were developed to express the yield point phenomenon [102-109]. Because the propagation of the Lüders front is highly related to the strain rate, many studies developed based on the rate-dependent plasticity model [102-105]. Also, some researchers suggested rate-independent hardening law for the yield point phenomenon for the sake of simplicity and predicted the macroscopically observed phenomenon very well [106-109]. According to Rainer and Volker [109], the true material hardening

accompanying the yield point phenomenon is observed differently through common measurements. The authors reported that the actual upper and lower yield stresses in the inhomogeneous deformation region were higher and lower than those measured by the uniaxial tensile test. In this discussion, the effect of the yield point phenomenon on the prediction of yield stress after cyclic bending deformation is presented by implementing the concept of true hardening behavior at the early deformation level.

To estimate the intrinsic (true) hardening behavior in the yield point region, the isotropic hardening law was split into early linear hardening (actually softening) from the upper yield point and subsequent nonlinear hardening. The simulation was then iterated until the apparent hardening curve measured by the experiment was obtained. For this, Eq. (4.5) was slightly modified as $\sigma_L = S \cdot \bar{\varepsilon} + \sigma_{y,upper}$. Here, S is a slope connecting the upper yield point and lower yield point and $\sigma_{y,upper}$ equals the true upper yield stress. The identified true upper and lower yield points satisfied the suggested equation in [4.5], which represented the Lüders strain extremely well. The determined values are S =12677.4 and $\sigma_{y,upper}$ = 542.1 MPa.

Figure 4.22(a) shows the true hardening determined through the above procedure and results in an apparent stress-strain curve. The predicted curve

with the modified early hardening model showed excellent agreement with the experimentally determined uniaxial tensile curve in Figure 4.1. Therefore, the new hardening could capture very well the inhomogeneous deformation in the yield point elongation region, including the yield plateau in Figure 4.22(b). Moreover, the modified hardening model could reproduce the Lüders band progression successfully, as demonstrated by the FE results in Figure 4.22(c), which corresponds to the deformation stage in Figure 4.22(b) within the inhomogeneous deformation region.

The previous simplified hardening based on combined perfect plastic and nonlinear hardening (see Eq. (4.5)) in the region of the yield point elongation could not accurately capture the inflected flow curves after cyclic BRB deformation. The modified hardening with initial linear softening was used for the prediction of the yield strengths in the three material orientations. Only the HAH model was used, and the results are shown in Figure 4.23. Note that the modified hardening model could reproduce the inflected (or stagnated) flow stress curves at approximately 1% strain. This stagnated hardening of the pre-deformed material was more pronounced in the 45° and 90° specimens, which is also consistent with the experiment. By contrast, hardening with the initial perfect plasticity predicted only monotonically increasing hardening without stagnation. This observation with the aid of an

FE simulation revealed the importance of modeling the yield point phenomenon if the yield strength or flow stress at the early deformation region needs to be accurately predicted. The existence of a yield plateau can be explained as follows. During bending and reverse bending, the materials through the plate thickness undergo plastic deformation. If the deformation is homogeneously applied with sufficient plastic strain, the material should not exhibit yield point elongation in the second tensile test. However, owing to the nature of bending, the material elements near the neutral surface are near elastic or plastic with a small amount under the investigated loading condition. Therefore, the additional tensile loading led to subsequent plastic deformation in the near-neutral surface, which induced the yield point elongation. Of course, the material elements away from the neutral surface during bending and reverse bending continue to experience a uniform deformation beyond the lower yield point region. Therefore, the deformation through the plate thickness is both homogeneous (near the plate surface) and inhomogeneous (near the neutral surface). During the second tensile loading, the deformation is localized in the material near the plate center because of the strain-softening from the upper yield point, whereas the other material elements do not significantly deform. The deformation in the center continues until the overall equilibrium is satisfied. Subsequently, the deformation becomes homogenous,

which is represented by continuous hardening after the stagnated flow region in Figure 4.23. Note that the Lüders strain increases as the magnitude of the upper yield point increases.

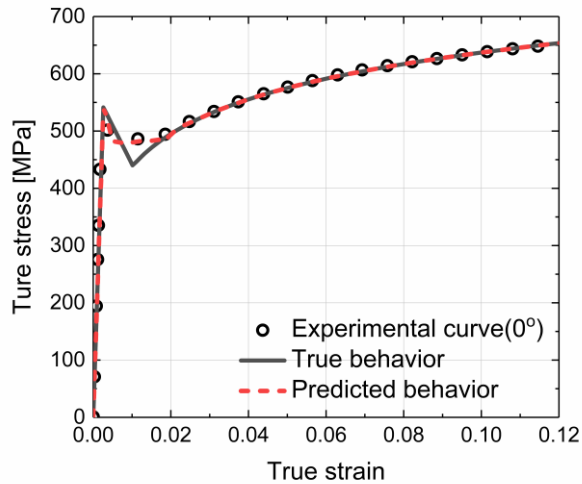

(a)

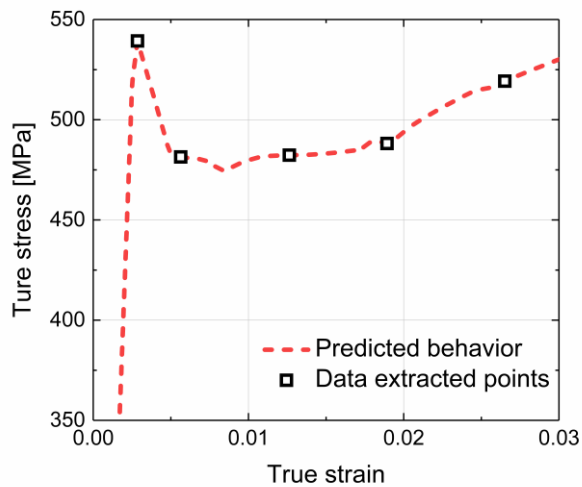

(b)

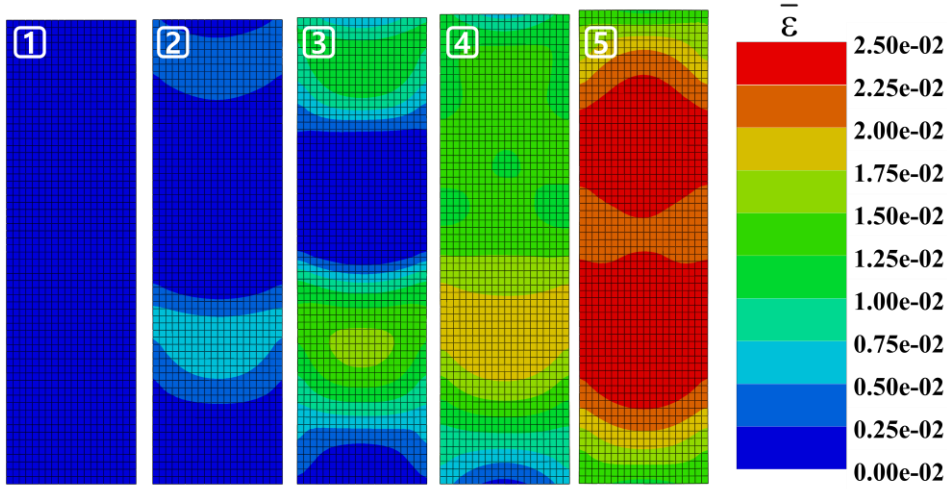

(c)

Figure 4.22. (a) Identified true stress-strain curve implemented in the finite element model, the resultant (apparent) stress-strain curve, and experimental data. (b) Magnified (predicted) flow curve in the inhomogeneous deformation region. (c) Evolution of inhomogeneous deformation during yield point phenomenon. The color code denotes the equivalent plastic strain.

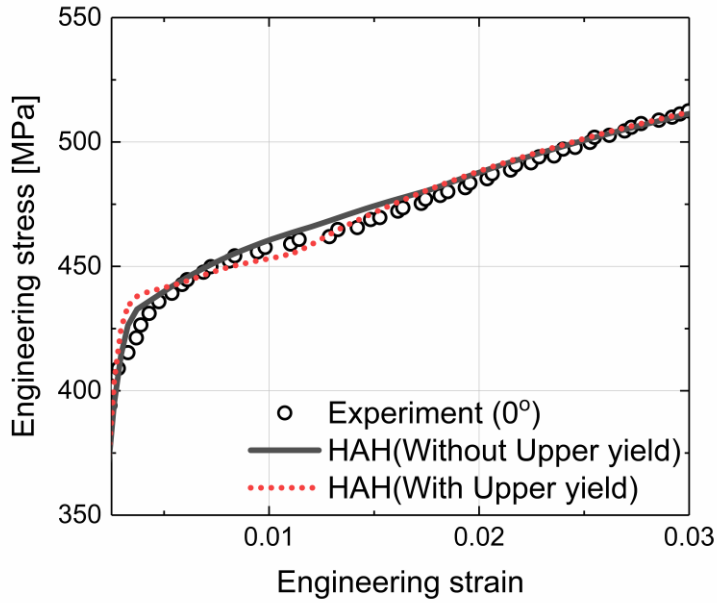
550
500
450
400
350
Engineering stress [MPa]
0.01
0.02
0.03
Engineering strain
Experiment (0°)
HAH(Without Upper yield)
HAH(With Upper yield)

(a)

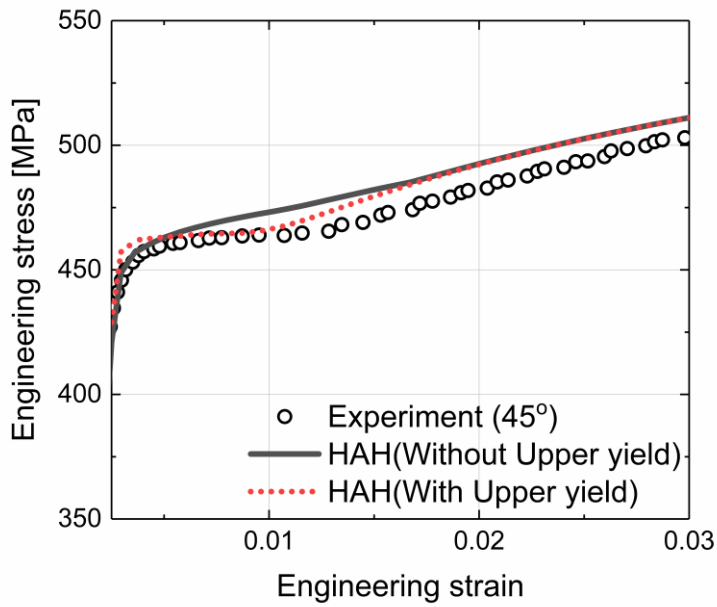
550
500
450
400
350
Engineering stress [MPa]
0.01
0.02
0.03
Engineering strain
Experiment (45°)
HAH(Without Upper yield)
HAH(With Upper yield)

(b)

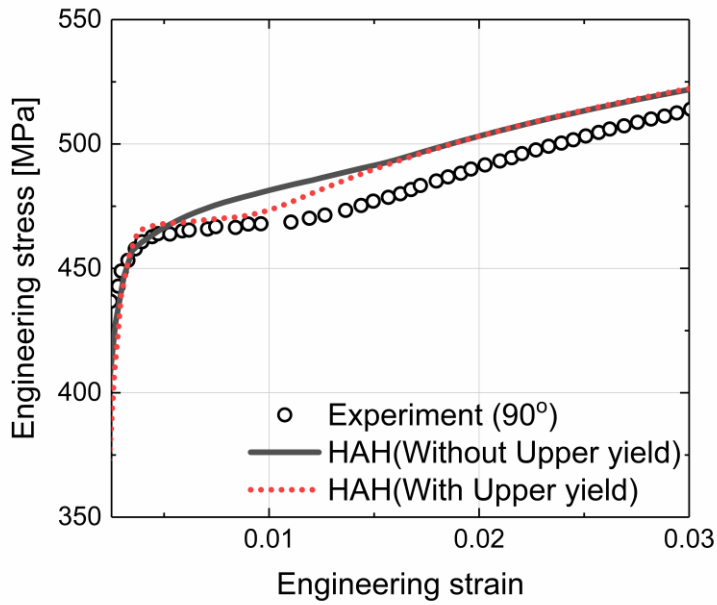

(c)

Figure 4.23. Comparison of predicted engineering stress-strain curves after BRB loading. The FE predicted curves are compared between the perfect plastic and linear softening model at the yield point elongation region: (a) 0°, (b) 45°, and (c) 90° tensile curves.

4.5. Summary

In this study, a comparative study on the effect of the hardening model on the prediction strength of steel pipes was presented. Three hardening models based on isotropic hardening, combined isotropic–kinematic hardening, and homogenous yield function-based anisotropic hardening (HAH) model were investigated. The parameters of the HAH model were identified using two-step tension and disk compression tests. To simulate the commonly applied manufacturing process of steel pipes, a BRB test was proposed. Tensile tests on the specimens taken out from the formed plate after the BRB process were performed in three different material orientations. The conclusions are summarized as follows.

- The investigated HAH distortional hardening model could capture most of the anisotropic hardening behaviors in the proposed two-step tension tests. That is, the Bauschinger effect and transient hardening behavior could be reproduced in the reverse loading experiment, whereas the cross-softening in the tension followed by the second orthogonal tension test. By contrast, the kinematic hardening model only captured the Bauschinger effect in the load-

reversal but underestimated it under the cross-loading condition.

- The predicted strengths along both the circumferential and transverse directions to the major bending direction matched very well with the experimentally measured yield and tensile strengths when the HAH hardening model with modified evolution rule was applied. However, the conventionally employed isotropic hardening and isotropic–kinematic hardening model resulted in either an over- or under-estimated yield strength after the prior BRB test. In the case of the tensile strength, the isotropic-kinematic hardening could reasonably predict the measured value.
- When the prior bending strain increased, the influence of the hardening model was more significant in the prediction of both the yield and tensile strengths.
- In addition to the flow strengths, the stagnated flow stress behavior under early plastic deformation after the bending and reverse bending processes could be well captured when the true yield point phenomenon was properly calibrated using the inverse numerical method.

5. Conclusion

In order to propose a model for predicting the anisotropic strengths of API steel pipe, the enhanced version of the HAH model was investigated. The enhanced version of the HAH model can express the anisotropic hardening behaviors in both the reverse-loading path and the cross-loading path, e.g. Buaschinger effect, transient behavior, permanent softening, latent hardening (cross-hardening), and contraction (cross-softening). For the stable numerical calculation of the HAH model inside finite element simulation, the fully implicit stress update algorithm was proposed in this study. Based on the proposed algorithm, the anisotropic strengths of the steel plate after bending/reverse-bending deformation were predicted.

Most of the applications using the HAH model were focused on the expression of the anisotropic behaviors of automotive steel sheets. Unlike previous studies, the strain range that this study interest in is relatively small(~4%). To express the early part of transient behavior with a high evolution rate after pre-deformation, multi-component evolution laws were proposed. The HAH model with multi-component evolution law could express the transient behavior right after the Bauschinger effect.

Because of the relatively small strain range that this study concern, finite

element simulation with an implicit solver is more efficient than the explicit solver. To get the stable solution using the implicit solver, a robust implicit algorithm for the HAH model is required. In this study, unlike previously proposed algorithms of the HAH model, an algorithm that considers all the state variables used in the model is proposed with the investigation in terms of the two subjects, i.e., the effect of the number of introduced residuals, and the difference between analytical derivatives and numerical derivatives.

- To investigate the effect of the number of residuals (or state variables) considered in the algorithms, three algorithms were studied, i.e., the cutting-plane algorithm (CPM or Semi-explicit), the Euler backward method with 4 residuals (EBM-4R), and the Euler backward method with 14 residuals (EBM-14R). Through one element assessment, the algorithms with a reduced number of residuals (CPM and EBM-4R) can predict a totally wrong r-value and the stress value. For the large-scale forming simulation, the EBM-based algorithm required much less computational time than the CPM algorithm. This is the due to time increment size difference. Because of the inaccurate consistent tangent modulus of CPM the size of automatically decided average time increment is relatively small compared to the one of EBM.

- To investigate the difference between the algorithms using analytical derivatives and numerical derivatives, EBM-14/AD and EBM-14/ND algorithms were proposed. In one element assessment, both algorithms showed similar performance in accuracy and calculation speed. However, the large-scale simulations with the material DP780 showed a difference between the two algorithms. The EBM-14/ND required more computation cost for the calculation. This result is expected to come from the non-quadratic yield locus used for the simulation. When the yield function exponent is not quadratic, the algorithms with numerical derivatives can cause additional computational cost within the stress update algorithm.

The BRB test was designed to mimic the pipe forming process of the API steel pipe. To validate the proposed HAH model with multi-component evolution laws and the stress update algorithm, the strengths prediction of the steel plate after bending/reverse-bending (BRB) deformation was performed. For the comparative study, the predictions using isotropic hardening, iso-kinematic hardening, and HAH models were conducted.

- The anisotropic hardening coefficients were identified based on

the TCT and TT tests. The isotropic hardening couldn't express any of the anisotropic hardening behavior as expected. The iso-kinematic hardening could capture the reversal loading behavior (TCT tests) very well but could not express the cross-loading behaviors (TT tests). The prediction by the proposed HAH model showed good agreement with the anisotropic hardening experimental results.

- As represented in the anisotropic hardening expression in TCT and TT tests, the IH model over-predict all the strengths after the BRB test. The IKH model could capture the strengths along the TD, which load-reversal behavior is important, but not for other directions. The proposed HAH model could capture the strengths along all the directions quite reasonably. As a result, the consideration of anisotropic hardening behaviors under the cross-loading state is very important to predict the anisotropic strengths prediction of the material with cyclic bending deformation.

Appendix A: Analytical derivatives of the HAH model

The first and second derivatives of the HAH model [39] are derived analytically as follows.

A.1. The first derivatives of equivalent stress

Only the derivatives in the case of $\mathbf{h}^{\mathbf{s}} : \hat{\mathbf{s}} > 0$ are presented here because a similar procedure can be employed for $\mathbf{h}^{\mathbf{s}} : \hat{\mathbf{s}} < 0$.

$$\frac{\partial \Phi}{\partial \boldsymbol{\sigma}} = \Phi^{1-q} \left\{ \begin{array}{l} \left(\psi(\mathbf{s}) + \psi(\mathbf{s}_{\mathrm{p}}) \right)^{\frac{q}{2}-1} \left(\psi(\mathbf{s}) \dfrac{\partial \psi(\mathbf{s})}{\partial \boldsymbol{\sigma}} + \psi(\mathbf{s}_{\mathrm{p}}) \dfrac{\partial \psi(\mathbf{s}_{\mathrm{p}})}{\partial \boldsymbol{\sigma}} \right) \\ + \mathrm{f}_2^{q} (2\hat{\mathbf{h}}^{\mathbf{s}} : \mathbf{s})^{q-1} 2\hat{\mathbf{h}}^{\mathbf{s}} : \dfrac{\partial \mathbf{s}}{\partial \boldsymbol{\sigma}} \end{array} \right\}, \tag{A.1.1}$$

$$\frac{\partial \Phi}{\partial \hat{\mathbf{h}}^{\mathbf{s}}} = \Phi^{1-q} \left\{ \begin{array}{l} \left(\psi(\mathbf{s}) + \psi(\mathbf{s}_{\mathrm{p}}) \right)^{\frac{q}{2}-1} \left(\psi(\mathbf{s}) \dfrac{\partial \psi(\mathbf{s})}{\partial \hat{\mathbf{h}}^{\mathbf{s}}} + \psi(\mathbf{s}_{\mathrm{p}}) \dfrac{\partial \psi(\mathbf{s}_{\mathrm{p}})}{\partial \hat{\mathbf{h}}^{\mathbf{s}}} \right) \\ + \mathrm{f}_2^{q} (2\hat{\mathbf{h}}^{\mathbf{s}} : \mathbf{s})^{q-1} 2\mathbf{s} \end{array} \right\}, \tag{A.1.2}$$

For $\mathbf{h}^{\mathbf{s}} : \hat{\mathbf{s}} > 0$, $\dfrac{\partial \Phi}{\partial \mathrm{g}_1} = \dfrac{\partial \Phi}{\partial \mathrm{g}_3} = \dfrac{\partial \Phi}{\partial \mathrm{g}_4} = \dfrac{\partial \Phi}{\partial \mathrm{g}_{\mathrm{R}}} = 0.$

For $\mathbf{h}^{\mathbf{s}} : \hat{\mathbf{s}} < 0$, $\dfrac{\partial \Phi}{\partial \mathrm{g}_2} = \dfrac{\partial \Phi}{\partial \mathrm{g}_3} = \dfrac{\partial \Phi}{\partial \mathrm{g}_4} = \dfrac{\partial \Phi}{\partial \mathrm{g}_{\mathrm{R}}} = 0.$

$$\frac{\partial \Phi}{\partial g_2} = \frac{1}{q}\Phi^{1-q}\left\{\left(2\hat{\mathbf{h}}^{s} : \mathbf{s}\right)^{1-q}\left(-\frac{1}{g_2^2}\right)\right\}, \tag{A.1.3}$$

$$\frac{\partial \Phi}{\partial g_L} = \Phi^{1-q}\left\{\left(\psi(\mathbf{s}) + \psi(\mathbf{s}_p)\right)^{\frac{q}{2}-1}\left(\psi(\mathbf{s})\frac{\partial \psi(\mathbf{s})}{\partial g_L} + \psi(\mathbf{s}_p)\frac{\partial \psi(\mathbf{s}_p)}{\partial g_L}\right)\right\}$$
$$\frac{\partial \psi(\mathbf{s})}{\partial g_L} = \frac{\partial \phi}{\partial \mathbf{s}''}\cdot\left(-\frac{1}{g_L^2}\mathbf{s}_0\right) \text{ and } \frac{\partial \psi(\mathbf{s}_p)}{\partial g_L} = \frac{\partial \phi}{\partial \mathbf{s}''}\cdot\left(-\frac{4(1-g_S)}{g_L^2}\mathbf{s}_0\right) \tag{A.1.4}$$

$$\frac{\partial \Phi}{\partial g_C} = \Phi^{1-q}\left\{\left(\psi(\mathbf{s}) + \psi(\mathbf{s}_p)\right)^{\frac{q}{2}-1}\psi(\mathbf{s}_p)\frac{\partial \psi(\mathbf{s}_p)}{\partial g_C}\right\}$$
where , (A.1.5)
$$\frac{\partial \psi(\mathbf{s}_p)}{\partial g_C} = \frac{\partial \phi}{\partial \mathbf{s}''}\cdot\left(-\frac{4}{g_L}\mathbf{s}_0\right).$$

A.2. The second derivatives of equivalent stress

Similarly, only the derivatives in the case of $\mathbf{h}^{s} : \hat{\mathbf{s}} > 0$ are presented here.

$$\frac{\partial^2 \Phi}{\partial \boldsymbol{\sigma}\partial \boldsymbol{\sigma}} = \frac{1}{q}\left(\frac{1}{q}-1\right)\Phi^{2-q}\left(\mathbf{A}\otimes\mathbf{A}\right) + \frac{1}{q}\Phi^{1-q}\frac{\partial \mathbf{A}}{\partial \boldsymbol{\sigma}}$$

With

$$\mathbf{A} = q\Phi^{q-1}\frac{\partial \Phi}{\partial \boldsymbol{\sigma}} \qquad \mathbf{B} = 2\left\{\psi(\mathbf{s})\frac{\partial \psi(\mathbf{s})}{\partial \boldsymbol{\sigma}} + \psi(\mathbf{s}_p)\frac{\partial \psi(\mathbf{s}_p)}{\partial \boldsymbol{\sigma}}\right\}$$
$$\frac{\partial \mathbf{A}}{\partial \boldsymbol{\sigma}} = \frac{q}{2}\left(\frac{q}{2}-1\right)\left\{\psi(\mathbf{s})^2 + \psi(\mathbf{s}_p)^2\right\}^{\frac{q}{2}-2}\mathbf{B}\otimes\mathbf{B} \tag{A.2.1}$$
$$+\frac{q}{2}\left\{\psi(\mathbf{s})^2 + \psi(\mathbf{s}_p)^2\right\}^{\frac{q}{2}-1}\frac{\partial \mathbf{B}}{\partial \boldsymbol{\sigma}}$$
$$+f_2^q q(q-1)\left(2\hat{\mathbf{h}}^{s} : \frac{\partial \mathbf{s}}{\partial \boldsymbol{\sigma}}\right)\otimes\left(2\hat{\mathbf{h}}^{s} : \frac{\partial \mathbf{s}}{\partial \boldsymbol{\sigma}}\right)$$

$$\frac{\partial \mathbf{B}}{\partial \boldsymbol{\sigma}} = 2\left\{\begin{array}{l} \dfrac{\partial \psi(\mathbf{s})}{\partial \boldsymbol{\sigma}} \otimes \dfrac{\partial \psi(\mathbf{s})}{\partial \boldsymbol{\sigma}} + \dfrac{\partial \psi(\mathbf{s}_p)}{\partial \boldsymbol{\sigma}} \otimes \dfrac{\partial \psi(\mathbf{s}_p)}{\partial \boldsymbol{\sigma}} \\ +\psi(\mathbf{s}) \dfrac{\partial^2 \psi(\mathbf{s})}{\partial \boldsymbol{\sigma} \partial \boldsymbol{\sigma}} + \psi(\mathbf{s}_p) \dfrac{\partial^2 \psi(\mathbf{s}_p)}{\partial \boldsymbol{\sigma} \partial \boldsymbol{\sigma}} \end{array}\right\}$$

$$\frac{\partial^2 \psi(\mathbf{s})}{\partial \boldsymbol{\sigma} \partial \boldsymbol{\sigma}} = \left(\frac{\partial \mathbf{s}''}{\partial \mathbf{s}} \cdot \frac{\partial \mathbf{s}}{\partial \boldsymbol{\sigma}}\right)^{\mathrm{T}} \cdot \left(\frac{\partial^2 \phi}{\partial \mathbf{s}'' \partial \mathbf{s}''}\right) \cdot \left(\frac{\partial \mathbf{s}''}{\partial \mathbf{s}} \cdot \frac{\partial \mathbf{s}}{\partial \boldsymbol{\sigma}}\right)$$

$$\frac{\partial^2 \psi(\mathbf{s}_p)}{\partial \boldsymbol{\sigma} \partial \boldsymbol{\sigma}} = \left(\frac{\partial \mathbf{s}_p''}{\partial \mathbf{s}} \cdot \frac{\partial \mathbf{s}}{\partial \boldsymbol{\sigma}}\right)^{\mathrm{T}} \cdot \left(\frac{\partial^2 \phi}{\partial \mathbf{s}_p'' \partial \mathbf{s}_p''}\right) \cdot \left(\frac{\partial \mathbf{s}_p''}{\partial \mathbf{s}} \cdot \frac{\partial \mathbf{s}}{\partial \boldsymbol{\sigma}}\right)$$

$$\frac{\partial^2 \Phi}{\partial \boldsymbol{\sigma} \partial \hat{\mathbf{h}}^s} = (1-q)\,\Phi^{-1} \frac{\partial \Phi}{\partial \boldsymbol{\sigma}} \otimes \frac{\partial \Phi}{\partial \hat{\mathbf{h}}^s} + \frac{1}{q} \Phi^{1-q} \frac{\partial \mathbf{A}}{\partial \hat{\mathbf{h}}^s}$$

With

$$\frac{\partial \mathbf{A}}{\partial \hat{\mathbf{h}}^s} = \frac{q}{2}\left(\frac{q}{2}-1\right)\left\{\psi(\mathbf{s})^2 + \psi(\mathbf{s}_p)^2\right\}^{\frac{q}{2}-2} \mathbf{B} \otimes \mathbf{B}^{\hat{\mathbf{h}}^s}$$

$$+\frac{q}{2}\left\{\psi(\mathbf{s})^2 + \psi(\mathbf{s}_p)^2\right\}^{\frac{q}{2}-1} \cdot \frac{\partial \mathbf{B}}{\partial \hat{\mathbf{h}}^s} + f_2^q q\left(2\hat{\mathbf{h}}^s : \mathbf{s}\right)^{q-1} 2\left(\frac{\partial \mathbf{s}}{\partial \boldsymbol{\sigma}}\right)^{\mathbf{T}}$$

$$+f_2^q q(q-1)\left(2\hat{\mathbf{h}}^s : \mathbf{s}\right)^{q-2}\left(2\hat{\mathbf{h}}^s : \frac{\partial \mathbf{s}}{\partial \boldsymbol{\sigma}}\right) \otimes 2\mathbf{s}$$

$$\mathbf{B}^{\hat{\mathbf{h}}^s} = 2\left\{\psi(\mathbf{s}) \frac{\partial \psi(\mathbf{s})}{\partial \hat{\mathbf{h}}^s} + \psi(\mathbf{s}_p) \frac{\partial \psi(\mathbf{s}_p)}{\partial \hat{\mathbf{h}}^s}\right\} \qquad \text{(A.2.2)}$$

$$\frac{\partial \mathbf{B}}{\partial \hat{\mathbf{h}}^s} = 2\left\{\begin{array}{l} \dfrac{\partial \psi(\mathbf{s})}{\partial \boldsymbol{\sigma}} \otimes \dfrac{\partial \psi(\mathbf{s})}{\partial \hat{\mathbf{h}}^s} + \dfrac{\partial \psi(\mathbf{s}_p)}{\partial \boldsymbol{\sigma}} \otimes \dfrac{\partial \psi(\mathbf{s}_p)}{\partial \hat{\mathbf{h}}^s} \\ +\psi(\mathbf{s}) \dfrac{\partial^2 \psi(\mathbf{s})}{\partial \boldsymbol{\sigma} \partial \hat{\mathbf{h}}^s} + \psi(\mathbf{s}_p) \dfrac{\partial^2 \psi(\mathbf{s}_p)}{\partial \boldsymbol{\sigma} \partial \hat{\mathbf{h}}^s} \end{array}\right\}$$

$$\frac{\partial^2 \psi(\mathbf{s})}{\partial \boldsymbol{\sigma} \partial \hat{\mathbf{h}}^s} = \left\{\left(1 - \frac{1}{g_L}\right) \mathrm{H}\left(\frac{\partial \phi}{\partial \mathbf{s}''} : \hat{\mathbf{h}}^s\right) \mathbf{I_4} + \hat{\mathbf{h}}^s \otimes \frac{\partial \phi}{\partial \mathbf{s}''}\right\} \cdot \frac{\partial \mathbf{s}}{\partial \boldsymbol{\sigma}}$$

$$\frac{\partial^2 \psi(\mathbf{s}_p)}{\partial \boldsymbol{\sigma} \partial \hat{\mathbf{h}}^s} = \left\{-\left(\frac{4(1-g_S)}{g_L}\right) \mathrm{H}\left(\frac{\partial \phi}{\partial \mathbf{s}''} : \hat{\mathbf{h}}^s\right) \mathbf{I_4} + \hat{\mathbf{h}}^s \otimes \frac{\partial \phi}{\partial \mathbf{s}''}\right\} \cdot \frac{\partial \mathbf{s}}{\partial \boldsymbol{\sigma}}$$

$$\frac{\partial^2\Phi}{\partial\boldsymbol{\sigma}\partial g_2}=\left(\frac{1-q}{q}\right)\Phi^{-q}\mathbf{A}\cdot\frac{\partial\Phi}{\partial g_2}+\frac{1}{q}\Phi^{1-q}\left\{\frac{-q\left(2\hat{\mathbf{h}}^{s}:\mathbf{s}\right)^{q-1}}{g_2^2}\right\}\left(2\hat{\mathbf{h}}^{s}:\frac{\partial\mathbf{s}}{\partial\boldsymbol{\sigma}}\right) \qquad \text{(A.2.3)}$$

$$\frac{\partial^2\Phi}{\partial\boldsymbol{\sigma}\partial g_L}=\left(\frac{1-q}{q}\right)\Phi^{-q}\frac{\partial\Phi}{\partial g_L}\mathbf{A}+\frac{1}{q}\Phi^{1-q}\frac{\partial\mathbf{A}}{\partial g_L}$$

With

$$\frac{\partial\mathbf{A}}{\partial g_L}=\frac{q}{2}\left(\frac{q}{2}-1\right)\left\{\psi(\mathbf{s})^2+\psi(\mathbf{s}_p)^2\right\}^{\frac{q}{2}-2}\mathbf{B}\cdot B^{g_L}$$

$$+\frac{q}{2}\left\{\psi(\mathbf{s})^2+\psi(\mathbf{s}_p)^2\right\}^{\frac{q}{2}-1}\cdot\frac{\partial\mathbf{B}}{\partial g_L}$$

$$B^{g_L}=2\left\{\psi(\mathbf{s})\frac{\partial\psi(\mathbf{s})}{\partial g_L}+\psi(\mathbf{s}_p)\frac{\partial\psi(\mathbf{s}_p)}{\partial g_L}\right\} \qquad \text{(A.2.4)}$$

$$\frac{\partial\mathbf{B}}{\partial g_L}=2\left\{\begin{array}{l}\dfrac{\partial\psi(\mathbf{s})}{\partial\boldsymbol{\sigma}}\dfrac{\partial\psi(\mathbf{s})}{\partial g_L}+\dfrac{\partial\psi(\mathbf{s}_p)}{\partial\boldsymbol{\sigma}}\dfrac{\partial\psi(\mathbf{s}_p)}{\partial g_L}\\ +\psi(\mathbf{s})\dfrac{\partial^2\psi(\mathbf{s})}{\partial\boldsymbol{\sigma}\partial g_L}+\psi(\mathbf{s}_p)\dfrac{\partial^2\psi(\mathbf{s}_p)}{\partial\boldsymbol{\sigma}\partial g_L}\end{array}\right\}$$

$$\frac{\partial^2\psi(\mathbf{s})}{\partial\boldsymbol{\sigma}\partial g_L}=\frac{\partial\phi}{\partial\mathbf{s}''}\cdot\left(-\frac{1}{g_L^2}\frac{\partial\mathbf{s_0}}{\partial\mathbf{s}}\right)\cdot\frac{\partial\mathbf{s}}{\partial\boldsymbol{\sigma}}$$

$$\frac{\partial^2\psi(\mathbf{s}_p)}{\partial\boldsymbol{\sigma}\partial g_L}=\frac{\partial\phi}{\partial\mathbf{s}_p''}\cdot\left(-\frac{4(1-g_S)}{g_L^2}\frac{\partial\mathbf{s_0}}{\partial\mathbf{s}}\right)\cdot\frac{\partial\mathbf{s}}{\partial\boldsymbol{\sigma}}$$

$$\frac{\partial^2\Phi}{\partial\boldsymbol{\sigma}\partial g_C}=\left(\frac{1-q}{q}\right)\Phi^{-q}\frac{\partial\Phi}{\partial g_C}\mathbf{A}+\frac{1}{q}\Phi^{1-q}\frac{\partial\mathbf{A}}{\partial g_C} \qquad \text{(A.2.5)}$$

With

$$\frac{\partial \mathbf{A}}{\partial g_C} = \frac{q}{2}\left(\frac{q}{2}-1\right)\left\{\psi(\mathbf{s})^2 + \psi(\mathbf{s}_p)^2\right\}^{\frac{q}{2}-2} \mathbf{B}\cdot B^{g_C}$$

$$+\frac{q}{2}\left\{\psi(\mathbf{s})^2 + \psi(\mathbf{s}_p)^2\right\}^{\frac{q}{2}-1}\cdot\frac{\partial \mathbf{B}}{\partial g_C}$$

$$B^{g_C} = 2\psi(\mathbf{s}_p)\frac{\partial \psi(\mathbf{s}_p)}{\partial g_C}$$

$$\frac{\partial \mathbf{B}}{\partial g_C} = 2\left\{\frac{\partial \psi(\mathbf{s}_p)}{\partial \boldsymbol{\sigma}}\frac{\partial \psi(\mathbf{s}_p)}{\partial g_C} + \psi(\mathbf{s}_p)\frac{\partial^2 \psi(\mathbf{s}_p)}{\partial \boldsymbol{\sigma}\partial g_C}\right\}$$

$$\frac{\partial^2 \psi(\mathbf{s}_p)}{\partial \boldsymbol{\sigma}\partial g_C} = \frac{\partial \phi}{\partial \mathbf{s}_p''}\cdot\left(-\frac{4}{g_L}\frac{\partial \mathbf{s_0}}{\partial \mathbf{s}}\right)\cdot\frac{\partial \mathbf{s}}{\partial \boldsymbol{\sigma}}$$

A.3. The first derivatives of the state variables $g_i\,(i = 1 \sim 4, L, C, R)$**.**

$$\partial_{g_1}\left(\frac{\partial g_1}{\partial \bar{\varepsilon}}\right) = \begin{cases} -k_2 & \left(\hat{\mathbf{h}}^{\mathbf{s}} : \mathbf{s} \geq 0\right) \\ -\dfrac{k_1 g_4}{g_1^2} & \left(\hat{\mathbf{h}}^{\mathbf{s}} : \mathbf{s} < 0\right) \end{cases} \tag{A.3.1}$$

$$\partial_{g_4}\left(\frac{\partial g_1}{\partial \bar{\varepsilon}}\right) = \begin{cases} 0 & \left(\hat{\mathbf{h}}^{\mathbf{s}} : \mathbf{s} \geq 0\right) \\ \dfrac{k_1}{g_1} & \left(\hat{\mathbf{h}}^{\mathbf{s}} : \mathbf{s} < 0\right) \end{cases} \tag{A.3.2}$$

$$\partial_{\bar{\varepsilon}}\left(\frac{\partial g_1}{\partial \bar{\varepsilon}}\right) = \begin{cases} -k_2 k_3 \dfrac{\bar{\sigma}(0)}{\bar{\sigma}\left(\bar{\varepsilon}\right)^2}\bar{\sigma}'\left(\bar{\varepsilon}\right) & \left(\hat{\mathbf{h}}^{\mathbf{s}} : \mathbf{s} \geq 0\right) \\ 0 & \left(\hat{\mathbf{h}}^{\mathbf{s}} : \mathbf{s} < 0\right) \end{cases} \tag{A.3.3}$$

$$\partial_{g_2}\left(\frac{\partial g_2}{\partial \bar{\varepsilon}}\right)=\begin{cases}-\dfrac{k_1 g_3}{g_2^2} & \left(\hat{\mathbf{h}}^s:\mathbf{s}\geq 0\right)\\ -k_2 & \left(\hat{\mathbf{h}}^s:\mathbf{s}<0\right)\end{cases} \tag{A.3.4}$$

$$\partial_{g_2}\left(\frac{\partial g_2}{\partial \bar{\varepsilon}}\right)=\begin{cases}-\dfrac{k_1 g_3}{g_2^2} & \left(\hat{\mathbf{h}}^s:\mathbf{s}\geq 0\right)\\ -k_2 & \left(\hat{\mathbf{h}}^s:\mathbf{s}<0\right)\end{cases} \tag{A.3.5}$$

$$\partial_{g_4}\left(\frac{\partial g_2}{\partial \bar{\varepsilon}}\right)=\begin{cases}\dfrac{k_1}{g_2} & \left(\hat{\mathbf{h}}^s:\mathbf{s}\geq 0\right)\\ 0 & \left(\hat{\mathbf{h}}^s:\mathbf{s}<0\right)\end{cases} \tag{A.3.6}$$

$$\partial_{\bar{\varepsilon}}\left(\frac{\partial g_2}{\partial \bar{\varepsilon}}\right)=\begin{cases}0 & \left(\hat{\mathbf{h}}^s:\mathbf{s}\geq 0\right)\\ -k_2 k_3 \dfrac{\bar{\sigma}(0)}{\bar{\sigma}\left(\bar{\varepsilon}\right)^2}\bar{\sigma}'\left(\bar{\varepsilon}\right) & \left(\hat{\mathbf{h}}^s:\mathbf{s}<0\right)\end{cases} \tag{A.3.7}$$

$$\partial_{g_3}\left(\frac{\partial g_3}{\partial \bar{\varepsilon}}\right)=\begin{cases}0 & \left(\hat{\mathbf{h}}^s:\mathbf{s}\geq 0\right)\\ -k_5 & \left(\hat{\mathbf{h}}^s:\mathbf{s}<0\right)\end{cases} \tag{A.3.8}$$

$$\partial_{g_4}\left(\frac{\partial g_4}{\partial \bar{\varepsilon}}\right)=\begin{cases}-k_5 & \left(\hat{\mathbf{h}}^s:\mathbf{s}\geq 0\right)\\ 0 & \left(\hat{\mathbf{h}}^s:\mathbf{s}<0\right)\end{cases} \tag{A.3.9}$$

$$\partial_{g_L}\left(\frac{\partial g_L}{\partial \bar{\varepsilon}}\right)=-k_L \tag{A.3.10}$$

$$\partial_{\bar{\varepsilon}}\left(\frac{\partial g_L}{\partial \bar{\varepsilon}}\right)=k_L\left(\sqrt{L\left(1-\cos^2\chi\right)+\cos^2\chi}-1\right)\left(\frac{\bar{\sigma}'\left(\bar{\varepsilon}\right)\cdot\bar{\sigma}\left(0\right)}{\bar{\sigma}\left(\bar{\varepsilon}\right)^2}\right) \tag{A.3.11}$$

$$\begin{aligned}\partial_{\boldsymbol{\sigma}}\left(\frac{\partial g_L}{\partial \bar{\varepsilon}}\right)=k_L&\left(\frac{\bar{\sigma}\left(\bar{\varepsilon}\right)-\bar{\sigma}\left(0\right)}{\bar{\sigma}\left(\bar{\varepsilon}\right)}\right)\frac{\left(1-L\right)\cos\chi}{\sqrt{L\left(1-\cos^2\chi\right)+\cos^2\chi}}\\&\times\frac{\sqrt{H}}{\sqrt{\mathbf{s}:\mathbf{s}}}\left(\mathbf{I}_4-\frac{1}{3}(\mathbf{I}\otimes\mathbf{I})\right)\cdot\left(\hat{\mathbf{h}}^s-\frac{\hat{\mathbf{h}}^s:\mathbf{s}}{\left(\mathbf{s}:\mathbf{s}\right)}\mathbf{s}\right)\end{aligned} \tag{A.3.12}$$

$$\partial_{\hat{\mathbf{h}}^s}\left(\frac{\partial g_L}{\partial \bar{\varepsilon}}\right)=k_L\left(\frac{\bar{\sigma}\left(\bar{\varepsilon}\right)-\bar{\sigma}\left(0\right)}{\bar{\sigma}\left(\bar{\varepsilon}\right)}\right)\frac{\left(1-L\right)\cos\chi}{\sqrt{L\left(1-\cos^2\chi\right)+\cos^2\chi}}\frac{\sqrt{H}}{\sqrt{\mathbf{s}:\mathbf{s}}}\mathbf{s} \tag{A.3.13}$$

$$\partial_{g_C}\left(\frac{\partial g_C}{\partial \bar{\varepsilon}}\right)=-k_C \tag{A.3.14}$$

$$\partial_{\boldsymbol{\sigma}}\left(\frac{\partial g_C}{\partial \bar{\varepsilon}}\right)=2k_C\left(S-1\right)\left(H\frac{\hat{\mathbf{h}}^s:\mathbf{s}}{\left(\mathbf{s}:\mathbf{s}\right)}\right)\left(\mathbf{I}_4-\frac{1}{3}(\mathbf{I}\otimes\mathbf{I})\right)\cdot\left(\hat{\mathbf{h}}^s-\frac{\hat{\mathbf{h}}^s:\mathbf{s}}{\left(\mathbf{s}:\mathbf{s}\right)}\mathbf{s}\right) \tag{A.3.15}$$

$$\partial_{\hat{\mathbf{h}}^s}\left(\frac{\partial g_C}{\partial \bar{\varepsilon}}\right)=2k_C\left(C-1\right)H\frac{\hat{\mathbf{h}}^s:\mathbf{s}}{\left(\mathbf{s}:\mathbf{s}\right)}\mathbf{s} \tag{A.3.16}$$

$$\partial_{g_R}\left(\frac{\partial g_R}{\partial \bar{\varepsilon}}\right)=-k_R \tag{A.3.17}$$

$$\partial_{\boldsymbol{\sigma}}\left(\frac{\partial g_R}{\partial \bar{\varepsilon}}\right)=-2k_R k'_R\left(H\frac{\hat{\mathbf{h}}^s:\mathbf{s}}{\left(\mathbf{s}:\mathbf{s}\right)}\right)\left(\mathbf{I}_4-\frac{1}{3}(\mathbf{I}\otimes\mathbf{I})\right)\cdot\left(\hat{\mathbf{h}}^s-\frac{\hat{\mathbf{h}}^s:\mathbf{s}}{\left(\mathbf{s}:\mathbf{s}\right)}\mathbf{s}\right) \tag{A.3.18}$$

$$\partial_{\hat{\mathbf{h}}^s}\left(\frac{\partial g_R}{\partial \bar{\varepsilon}}\right)=-2k_R k'_R H\frac{\hat{\mathbf{h}}^s:\mathbf{s}}{\left(\mathbf{s}:\mathbf{s}\right)}\mathbf{s} \tag{A.3.19}$$

A.4. The first derivatives of the state variables $\hat{\mathbf{h}}^{s}$.

The value $\mathrm{sgn}\left(\cos(\chi)\right)$ used in this section is defined as follows.

$$\mathrm{sgn}\left(\cos(\chi)\right)=\begin{cases}+1 & \left(\hat{\mathbf{h}}^{s}:\mathbf{s}\geq 0\right)\\ -1 & \left(\hat{\mathbf{h}}^{s}:\mathbf{s}<0\right)\end{cases} \tag{A.4.1}$$

$$\partial_{g_R}\left(\frac{\partial\hat{\mathbf{h}}^{s}}{\partial\bar{\varepsilon}}\right)=\mathrm{k}\,\mathrm{sgn}\left(\cos(\chi)\right)\left(\hat{\mathbf{s}}-\cos(\chi)\hat{\mathbf{h}}^{s}\right) \tag{A.4.2}$$

$$\begin{aligned}\partial_{\sigma}\left(\frac{\partial\hat{\mathbf{h}}^{s}}{\partial\bar{\varepsilon}}\right)=\mathrm{k}\,\mathrm{sgn}\left(\cos\chi\right)\left(|\cos\chi|^{1/z}+g_R\right)\times\\ \left[\begin{array}{l}\frac{1}{\sqrt{H}}\frac{1}{\sqrt{\mathbf{s}:\mathbf{s}}}\left\{\mathbf{I}_4-\frac{(\mathbf{s}\otimes\mathbf{s})}{\mathbf{s}:\mathbf{s}}-\mathrm{H}\hat{\mathbf{h}}\otimes\left(\hat{\mathbf{h}}^{s}-\frac{\hat{\mathbf{h}}^{s}:\mathbf{s}}{(\mathbf{s}:\mathbf{s})}\mathbf{s}\right)\right\}\\ \cdot\left(\mathbf{I}_4-\frac{1}{3}(\mathbf{I}\otimes\mathbf{I})\right)\\ +\left(\hat{\mathbf{s}}-\cos\chi\hat{\mathbf{h}}^{s}\right)\otimes\frac{1}{z}\mathrm{sgn}\left(\cos\chi\right)|\cos\chi|^{1/z-1}\\ \frac{\sqrt{\mathrm{H}}}{\sqrt{\mathbf{s}:\mathbf{s}}}\cdot\left(\hat{\mathbf{h}}^{s}-\frac{\hat{\mathbf{h}}^{s}:\mathbf{s}}{(\mathbf{s}:\mathbf{s})}\mathbf{s}\right)\end{array}\right]\end{aligned} \tag{A.4.3}$$

$$\partial_{\hat{\mathbf{h}}^{\mathrm{s}}}\left(\frac{\partial\hat{\mathbf{h}}^{\mathrm{s}}}{\partial\bar{\varepsilon}}\right)=\mathrm{k}\,\mathrm{sgn}\left(\cos\chi\right)\begin{bmatrix}-\left(|\cos\chi|^{1/z}+g_R\right)\dfrac{\sqrt{\mathrm{H}}}{\sqrt{\mathbf{s}:\mathbf{s}}}\\ \left\{\hat{\mathbf{h}}^{\mathrm{s}}\otimes\mathbf{s}+\left(\hat{\mathbf{h}}^{\mathrm{s}}:\mathbf{s}\right)\mathbf{I}_4\right\}+\\ \dfrac{1}{z}\mathrm{sgn}\left(\cos\chi\right)|\cos\chi|^{1/z-1}\\ \left(\hat{\mathbf{s}}-\cos\chi\hat{\mathbf{h}}^{\mathrm{s}}\right)\otimes\dfrac{\sqrt{\mathrm{H}}}{\sqrt{\mathbf{s}:\mathbf{s}}}\mathbf{s}\end{bmatrix} \tag{A.4.4}$$

Appendix B Numerical derivatives of e-HAH model

In the previous study by Choi and Yoon [57], the central finite difference method was adopted for numerical derivatives because of its faster convergence and lower error. Therefore, in this study, the same finite difference is employed. For the step size decision for numerical differentiation, the scaled stress space idea [69] is used. For the sake of simplicity, the Voigt notation under the plane stress condition is used. The step sizes for each state variable are defined based on common step size, as follows.

$$2\Phi^a=\left|X_1'-X_2'\right|^a+\left|2X_2''+X_1''\right|^a+\left|2X_1''+X_2''\right|^a, \tag{B.1}$$

In this study, $\mathrm{a}=1.0\times10^{-6}$ was employed for the calculation. Examples of the first and second derivatives with respect to stress are shown

as follows.

$$\frac{\partial \Phi}{\partial \sigma_3} \approx \frac{\Phi\left(\sigma_1, \sigma_2, \sigma_3 + \delta\sigma_3\right) - \Phi\left(\sigma_1, \sigma_2, \sigma_3 - \delta\sigma_3\right)}{2\delta\sigma_3}, \tag{B.2}$$

$$\frac{\partial^2 \Phi}{\partial \sigma_3 \partial \sigma_3} \approx \frac{\Phi\left(\sigma_1, \sigma_2, \sigma_3 + \delta\sigma_3\right) - 2\Phi\left(\sigma_1, \sigma_2, \sigma_3\right) + \Phi\left(\sigma_1, \sigma_2, \sigma_3 - \delta\sigma_3\right)}{\left(\delta\sigma_3\right)^2}, \tag{B.3}$$

$$\frac{\partial^2 \Phi}{\partial \sigma_1 \partial \sigma_3} \approx \frac{1}{4\delta\sigma_1\delta\sigma_3} \begin{bmatrix} \Phi\left(\sigma_1 + \delta\sigma_1, \sigma_2, \sigma_3 + \delta\sigma_3\right) \\ -\Phi\left(\sigma_1 - \delta\sigma_1, \sigma_2, \sigma_3 + \delta\sigma_3\right) \\ -\Phi\left(\sigma_1 + \delta\sigma_1, \sigma_2, \sigma_3 - \delta\sigma_3\right) \\ +\Phi\left(\sigma_1 - \delta\sigma_1, \sigma_2, \sigma_3 - \delta\sigma_3\right) \end{bmatrix}, \tag{B.4}$$

Similarly, all other derivatives associated with the HAH can be calculated. There is a remark for using numerical derivatives with respect to $g_i \left(i = 1 \sim 4, L, S, R\right)$. g values have an admissible range of value; e.g. $0 < g_1 \leq 1$. When g_1 equals 0 or 1, the numerical derivatives cannot be defined. In this case, the forward or backward difference method can be applied.

Appendix C: Yld2000-2d yield function

A non-quadratic anisotropic yield function proposed by Barlat et al. [71, 72] is formulated as follows

$$2\Phi^a = \left|X_1' - X_2'\right|^a + \left|2X_2'' + X_1''\right|^a + \left|2X_1'' + X_2''\right|^a, \tag{C.1}$$

Where X_i' and $X_i''(i=1, 2)$ are the principal values of linearly transformed Cauchy stress. For simplicity, the Voigt notation is used for the formulation. The relationship between $\boldsymbol{X}'(or\ \boldsymbol{X}'')$ and $\boldsymbol{\sigma}$ is as follows.

$$\begin{aligned} \boldsymbol{X}' &= C' \cdot \mathbf{s} = C' \cdot T \cdot \boldsymbol{\sigma} = L' \cdot \boldsymbol{\sigma} \\ \boldsymbol{X}'' &= C'' \cdot \mathbf{s} = C'' \cdot T \cdot \boldsymbol{\sigma} = L'' \cdot \boldsymbol{\sigma} \end{aligned}, \tag{C.3}$$

The components of linear transformation matrixes consist of the anisotropic coefficients $\alpha_{1\sim8}$ as follows.

$$\begin{aligned} L' &= \frac{1}{3}\begin{bmatrix} 2\alpha_1 & -\alpha_1 & 0 \\ -\alpha_2 & 2\alpha_2 & 0 \\ 0 & 0 & 3\alpha_7 \end{bmatrix} \\ L' &= \frac{1}{9}\begin{bmatrix} -2\alpha_3 + 2\alpha_4 + 8\alpha_5 - 2\alpha_6 & \alpha_3 - 4\alpha_4 - 4\alpha_5 + 4\alpha_6 & 0 \\ 4\alpha_3 - 4\alpha_4 - 4\alpha_5 + \alpha_6 & -2\alpha_3 + 8\alpha_4 + 2\alpha_5 - 2\alpha_6 & 0 \\ 0 & 0 & 9\alpha_8 \end{bmatrix} \end{aligned} \tag{C.3}$$

Appendix D: Isotropic-kinematic hardening (IKH) model

The yield criterion for the isotropic-kinematic hardening was proposed by Chaboche [22], and is expressed as follows:

$$\phi(\boldsymbol{\sigma}-\boldsymbol{\alpha})=\bar{\sigma}_{iso}\left(\bar{\boldsymbol{\varepsilon}}\right), \tag{D.1}$$

where $\boldsymbol{\alpha}$ is a back stress tensor describing the translation of the yield surface, and $\bar{\sigma}_{iso}\left(\bar{\boldsymbol{\varepsilon}}\right)$ is an isotropic hardening term that determines the size of the yield surface. The translation of the yield surface can be modeled with multi-component back stresses with a nonlinear evolution law as follows.

$$\boldsymbol{\alpha}=\sum_{i=1}^{n}\boldsymbol{\alpha}_i\,, \tag{D.2}$$

$$d\boldsymbol{\alpha}_i=\frac{C_i}{\bar{\sigma}_{iso}}(\boldsymbol{\sigma}-\boldsymbol{\alpha})\cdot d\bar{\boldsymbol{\varepsilon}}-\gamma_i\boldsymbol{\alpha}_i\cdot d\bar{\boldsymbol{\varepsilon}}\,, \tag{D.3}$$

where C_i and γ_i are the hardening coefficients. In this study, three back stress tensors (i = 3) were employed.

To produce the same monotonic hardening curve as the IH and HAH models, the following isotropic hardening term was used in the IKH model.

$$\bar{\sigma}_{iso}\left(\bar{\boldsymbol{\varepsilon}}\right)=\bar{\sigma}\left(\bar{\boldsymbol{\varepsilon}}\right)-\sum_{i=1}^{n}\frac{C_i}{\gamma_i}\left\{1-\exp\left(-\gamma_i\bar{\boldsymbol{\varepsilon}}\right)\right\}, \tag{D.4}$$

Reference

[1] R. Sowerby, D.K. Uko, Y. Tomita, A review of certain aspects of the Bauschinger effect in metals, Mater. Sci. Eng. 41 (1) (1979) 43-58.

[2] P.S. Bate, D.V. Wilson, Analysis of the Bauschinger effect, Acta Metall. 34 (6) (1986) 1097-1105.

[3] F. Yoshida, T. Uemori, A model of large-strain cyclic plasticity describing the Bauschinger effect and workhardening stagnation, Int. J. Plast. 18 (5-6) (2002) 661-686.

[4] R.K. Boger, R.H. Wagoner, F. Barlat, M.G. Lee, K. Chung, Continuous, large strain, tension/compression testing of sheet material, Int. J. Plast. 21 (12) (2005) 2319-2343.

[5] A.A. Mamun, R.J. Moat, J. Kelleher, P.J. Bouchard, Origin of the Bauschinger effect in a polycrystalline material, Mater. Sci. Eng. A 707 (2017) 576-584.

[6] K.P. Li, W.P. Carden, R.H. Wagoner, Simulation of springback, Int. J. Mech. Sci. 44 (1) (2002) 103-122.

[7] M.G. Lee, D. Kim, C. Kim, M.L. Wenner, K. Chung, Spring-back evaluation of automotive sheets based on isotropic–kinematic hardening laws

and non-quadratic anisotropic yield functions, part III: applications, Int. J. Plast. 21 (5) (2005) 915-953.

[8] M.G. Lee, D. Kim, C. Kim, M.L. Wenner, R.H. Wagoner, K. Chung, A practical two-surface plasticity model and its application to spring-back prediction, Int. J. Plast. 23 (7) (2007) 1189-1212.

[9] R.H. Wagoner, H. Lim, M.G. Lee, Advanced issues in springback, Int. J. Plast. 45 (2013) 3-20.

[10] P. Franciosi, The concepts of latent hardening and strain hardening in metallic single crystals. Acta Metall. 33 (9) (1985) 1601-1612.

[11] J.H. Schmitt, E.L. Shen, J.L. Raphanel, A parameter for measuring the magnitude of a change of strain path: validation and comparison with experiments on low carbon steel, Int. J. Plast. 10 (5) (1994) 535-551.

[12] G. Vincze, F. Barlat, E.F. Rauch, C.N. Tomé, M.C. Butuc, J.J. Grácio, Experiments and modeling of low carbon steel sheet subjected to double strain path changes, Metall. Mater. Trans. A 44 (10) (2013) 4475-4479.

[13] J. Ha, M. G. Lee, F. Barlat, Strain hardening response and modeling of EDDQ and DP780 steel sheet under non-linear strain path, Mech. Mater. 64 (2013) 11-26.

[14] W. Wen, M. Borodachenkova, C.N. Tomé, G. Vincze, E.F. Rauch, F. Barlat, J.J. Grácio, Mechanical behavior of low carbon steel subjected to strain path changes: Experiments and modeling, Acta Mater. 111 (2016) 305-314.

[15] S.B. Zaman, F. Barlat, J.H. Kim, Deformation-induced anisotropy of uniaxially prestrained steel sheet, Int. J. Solids Struct. 134 (2018) 20-29.

[16] L. Sun, R.H. Wagoner, Proportional and non-proportional hardening behavior of dual-phase steels, Int. J. Plast. 45 (2013) 174-187.

[17] J. Liao, J. A. Sousa, A.B. Lopes, X. Xue, F. Barlat, A.B. Pereira, Mechanical, microstructural behaviour and modelling of dual phase steels under complex deformation paths, Int. J. Plast. 93 (2017) 269-290.

[18] J. Ha, J. Lee, J.H. Kim, M.G. Lee, F. Barlat, Investigation of plastic strain rate under strain path changes in dual-phase steel using microstructure-based modeling. Int. J. Plast. 93 (2017) 89-111.

[19] W. Prager, A new methods of analyzing stresses and strains in work hardening plastic solids, J. Appl. Mech.(ASME), 23 (1956) 493-496.

[20] H. Ziegler, A modification of Prager's hardening rule, Q. Appl. Math. 17 (1) (1959) 55-65.

[21] P.J. Armstrong, C.O. Frederick, A mathematical representation of the multiaxial Bauschinger effect, in: Central Electricity Generating Board Report, Berkeley Nuclear Laboratories, 1966.

[22] J.L. Chaboche, Time-independent constitutive theories for cyclic plasticity, Int. J. Plasticity 2 (1986) 149–188.

[23] N. Ohno, J.D. Wang, Kinematic hardening rules with critical state of dynamic recovery, part I: formulation and basic features for ratchetting behavior, Int. J. Plast. 9(3) (1993) 375-390.

[24] F. Yoshida, T. Uemori, K. Fujiwara, Elastic–plastic behavior of steel sheets under in-plane cyclic tension–compression at large strain, Int. J. Plast. 18 (5-6) (2002) 633-659.

[25] K. Chung, M.G. Lee, D. Kim, C. Kim, M.L. Wenner, F. Barlat, Spring-back evaluation of automotive sheets based on isotropic-kinematic hardening laws and non-quadratic anisotropic yield functions: Part I: theory and formulation, Int. J. Plast. 21 (5) (2005) 861-882.

[26] M. Ortiz, E.P. Popov, Distortional hardening rules for metal plasticity, J. Eng. Mech.109 (4) (1983) 1042-1057.

[27] H.P. Feigenbaum, Y.F. Dafalias, Directional distortional hardening in

metal plasticity within thermodynamics, Int. J. Solids Struct. 44 (22-23) (2007) 7526-7542.

[28] H.P. Feigenbaum, Y.F. Dafalias, Simple model for directional distortional hardening in metal plasticity within thermodynamics, J. Eng. Mech. 134 (9) (2008) 730-738.

[29] C. Teodosiu, Z. Hu, Evolution of the intragranular microstructure at moderate and large strains: modelling and computational significance, in: S. Shen, P.R. Dawson (Eds.) Proceedings of Numiform'95 on Simulation of Materials Processing: Theory, Methods and Applications, Rotterdam, Balkema, 1995, pp. 173–182.

[30] M. François, A plasticity model with yield surface distortion for non proportional loading, Int. J. Plast. 17 (5) (2001) 703-717.

[31] H. Badreddine, Z.M. Yue, K. Saanouni, Modeling of the induced plastic anisotropy fully coupled with ductile damage under finite strains, Int. J. Solids Struct. 108 (2017) 49-62.

[32] J. Qin, B. Holmedal, O.S. Hopperstad, A combined isotropic, kinematic and distortional hardening model for aluminum and steels under complex strain-path changes, Int. J. Plast. 101 (2018) 156-169.

[33] D.G. Tari, M.J. Worswick, U. Ali, M.A. Gharghouri, Mechanical response of AZ31B magnesium alloy: Experimental characterization and material modeling considering proportional loading at room temperature, Int. J. Plast. 55 (2014) 247-267.

[34] H.J. Choi, K.J. Lee, Y. Choi, G. Bae, D.C. Ahn, M.G. Lee, Effect of evolutionary anisotropy on earing prediction in cylindrical cup drawing, JOM 69 (5) (2017) 915-921.

[35] A. Abedini, C. Butcher, M.J. Worswick, Application of an evolving non-associative anisotropic-asymmetric plasticity model for a rare-earth magnesium alloy, Metals 8 (12) (2018) 1013.

[36] T. Park, F. Abu-Farha, F. Pourboghrat, An evolutionary yield function model based on plastic work and non-associated flow rule, Metals 9 (5) (2019) 611.

[37] F. Barlat, J.J. Gracio, M.G. Lee, E.F. Rauch, G. Vincze, An alternative to kinematic hardening in classical plasticity, Int. J. Plast. 27 (9) (2011) 1309-1327.

[38] F. Barlat, J. Ha, J.J. Grácio, M.G. Lee, E.F. Rauch, G. Vincze, Extension of homogeneous anisotropic hardening model to cross-loading with latent effects, Int. J. Plast. 46 (2013) 130-142.

[39] F. Barlat, G. Vincze, J.J. Grácio, M.G. Lee, E.F. Rauch, C.N. Tomé, Enhancements of homogenous anisotropic hardening model and application to mild and dual-phase steels, Int. J. Plast. 58 (2014) 201-218.

[40] J.W. Lee, M.G. Lee, F. Barlat, Finite element modeling using homogeneous anisotropic hardening and application to spring-back prediction, Int. J. Plast. 29 (2012) 13-41.

[41] J.Y. Lee, J.W. Lee, M G. Lee, F. Barlat, An application of homogeneous anisotropic hardening to springback prediction in pre-strained U-draw/bending, Int. J. Solids Struct. 49 (25) (2012) 3562-3572.

[42] J. Choi, J. Lee, G. Bae, F. Barlat, M.G. Lee, Evaluation of springback for DP980 S rail using anisotropic hardening models, JOM 68 (7) (2016) 1850-1857.

[43] O.M. Badr, B. Rolfe, P. Zhang, M. Weiss, Applying a new constitutive model to analyse the springback behaviour of titanium in bending and roll forming, Int. J. Mech. Sci. 128 (2017) 389-400.

[44] J. Liao, X. Xue, M.G. Lee, F. Barlat, G. Vincze, A.B. Pereira, Constitutive modeling for path-dependent behavior and its influence on twist springback, Int. J. Plast. 93 (2017) 64-88.

[45] J. Choi, J. Lee, H.J. Bong, M.G. Lee, F. Barlat, Advanced constitutive modeling of advanced high strength steel sheets for springback prediction after double stage U-draw bending, Int. J. Solids Struct. 151 (2018) 152-164.

[46] S. Chen, J. Liao, H. Xiang, X. Xue, A.B. Pereira, Pre-strain effect on twist springback of a 3D P-channel in deep drawing, J. Mater. Process. Technol. (2019) 116224.

[47] S.J. Marcadet, D. Mohr, Effect of compression–tension loading reversal on the strain to fracture of dual phase steel sheets, Int. J. Plast 72 (2015) 21-43.

[48] J. Papasidero, V. Doquet, D. Mohr, Ductile fracture of aluminum 2024-T351 under proportional and non-proportional multi-axial loading: Bao–Wierzbicki re-sults revisited, Int. J. Solids Struct. 69 (2015) 459-474.

[49] A. Abedini, C. Butcher, M.J. Worswick, Experimental fracture characterisation of an anisotropic magnesium alloy sheet in proportional and non-proportional loading conditions, Int. J. Solids Struct. 144 (2018) 1-19.

[50] J.C. Simo, T.J.R. Hughes, Computational Inelasticity, Springer, 1998.

[51] J.C. Simo, R.L. Taylor, A return mapping algorithm for plane stress elastoplasticity, Int. J. Numer. Methods Eng. 22 (3) (1986) 649-670.

[52] F. Armero, A. Pérez-Foguet, On the formulation of closest-point projection algorithms in elastoplasticity—part I: The variational structure, Int. J. Numer. Methods Eng. 53 (2) (2002) 297-329.

[53] A. Pérez-Foguet, F. Armero, On the formulation of closest-point projection algorithms in elastoplasticity— part II: Globally convergent schemes, Int. J. Numer. Methods Eng. 53 (2) (2002) 297-329.

[54] J.C. Simo, M. Ortiz, A unified approach to finite deformation elastoplastic analysis based on the use of hyperelastic constitutive equations, Comput. Methods Appl. Mech. Eng. 49 (2) (1985) 221-245.

[55] J. Lee, M.G. Lee, F. Barlat, J.H. Kim, Stress integration schemes for novel homogeneous anisotropic hardening model, Comput. Methods Appl. Mech. Eng. 247 (2012) 73-92.

[56] J. Lee, D. Kim, Y.S. Lee, H.J. Bong, F. Barlat, M.G. Lee, Stress update algorithm for enhanced homogeneous anisotropic hardening model, Comput. Methods Appl. Mech. Eng. 286 (2015) 63-86.

[57] H. Choi, J.W. Yoon, Stress integration-based on finite difference method and its application for anisotropic plasticity and distortional hardening under associated and non-associated flow rules, Comput. Methods Appl. Mech. Eng. 345 (2019) 123-160.

[58] S.Y. Yoon, S.Y. Lee, F. Barlat, Numerical integration algorithm of updated homogeneous anisotropic hardening model through finite element framework, Comput. Methods Appl. Mech. Eng. 372 (2020) 113449.

[59] F. Barlat, S.Y. Yoon, S.Y. Lee, M.S. Wi, J.H. Kim, Distortional plasticity framework with application to advanced high strength steel, Int. J. Solids. Struct. 202 (2020) 947-962.

[60] P. Thibaux, F. Van den Abeele, (2010, January). Influence of the Forming Operations on the Yield Stress Measured on Pipe. *International Pipeline Conference* (Vol. 44212, pp. 399-407).

[61] S. Cooreman, D. Van Hoecke, M. Liebeherr, P. Thibaux, M. Yamaguti Enderlin (2016, September). Experimental and numerical study on the evolution of mechanical properties during spiral pipe forming. In *International Pipeline Conference* (Vol. 50275, p. V003T05A025). American Society of Mechanical Engineers.

[62] T. Zou, D. Li, G. Wu, Y. Peng, Yield strength development from high strength steel plate to UOE pipe, Mater Design 89 (2016) 1107-1122.

[63] J. Lee, D. Kim, L. Quagliato, S. Kang, N. Kim, Change of the yield stress in roll formed ERW pipes considering the Bauschinger effect, J. Mater. Process. Technol. 244 (2017) 304-313.

[64] J. Yi, S.C. Kang, H.M. Koh, K.F. Choo, Yield Strength Prediction of UOE Pipes: From Forming to Flattening, *International Journal of Offshore and Polar Engineering 28*(02) (2018) 206-211.

[65] J. Jiao, C. Lu, C. Lee, J. Bae, F. Barbaro, Introduction of the delta concept for characterising pipe yield strength, Int. J. Mater. Form (2019) 1-15.

[66] J. Yi, S.C. Kang, W. Park, J.F. Choo, Yield strength tracking of UOE pipe considering various thickness-to-diameter ratios. Mar Struct 68 (2019) 102616.

[67] H. Choi, S. Choi, S.C. Kang, C. Kim, M.G. Lee, Prediction of anisotropic strengths of steel plate after prior bending-reverse bending deformation: Application of distortional hardening model, Int. J. Mech. Sci 24 (2021) 106512.

[68] H. Choi, S. Choi, S.C. Kang, M.G. Lee, Fully Implicit Stress Update Algorithm for Distortion-Based Anisotropic Hardening with Cross-Loading Effect: Comparative Algorithmic Study and Application to Large-Size Forming Problem. Appl. Sci. 11 (12) (2021) 5509.

[69] H. Aretz, An advanced numerical differentiation scheme for plastic strain-rate computation, in: AIP Conf. Proc., AIP, 2007, pp.151–156.

[70] J.W. Yoon, D.Y. Yang, K. Chung, Elasto-plastic finite element method based on incremental deformation theory and continuum based shell elements for planar anisotropic sheet materials, Comput. Methods Appl. Mech. Eng. 174 (1999) 23–56.

[71] F. Barlat, J. C. Brem, J. W. Yoon, K. Chung, R.E. Dick, D.J. Lege, F. Pourboghrat, S.H. Choi, E. Chu, Plane stress yield function for aluminum alloy sheets - Part 1: Theory, Int. J. Plast. 19 (2003) 1297–1319.

[72] J.W. Yoon, F. Barlat, R.E. Dick, K. Chung, T.J. Kang, Plane stress yield function for aluminum alloy sheets—part II: FE formulation and its implementation, Int. J. Plast. 20 (3) (2004) 495-522.

[73] A. Žerovnik, V. Pepel, I. Prebil, R. Kunc, The yield-point phenomenon and cyclic plasticity of the uniaxially loaded specimens, Mater. Design. (92) (2016) 971-977.

[74] R. Hill, A theory of the yielding and plastic flow of anisotropic metals, Phys Eng Sci, 193 (1948), pp. 281-297.

[75] M. Luo, T. Wierzbicki, Numerical failure analysis of a stretch-bending test on dual-phase steel sheets using a phenomenological fracture model, Int. J. Solids Struct. 47(22-23) (2010) 3084–3102.

[76] V. Grolleau, C.C. Roth, V. Lafilé, B. Galpin, D. Mohr, Loading of mini-Nakazima specimens with a dihedral punch: Determining the strain to fracture for plane strain tension through stretch-bending, Int. J. Mech. Sci. 152 (2019) 329-345.

[77] L. Kachanov, Introduction to continuum damage mechanics (Vol. 10). Springer Science & Business Media; (1986)

[78] D. Krajcinovic, J. Lemaitre, Continuum damage mechanics: theory and applications (pp. 37-90). New York: Springer-Verlag; (1987)

[79] J.-L. Chaboche, Continuum damage mechanics: Part I—General concepts; (1988)

[80] J.-L. Chaboche, Continuum damage mechanics: Part II—Damage growth, crack initiation, and crack growth.; (1988)

[81] J. Lemaitre, J.-L. Chaboche, Mechanics of solid materials, Cambridge: Cambridge University Press; (1994).

[82] J. Lemaitre, R. Desmorat, Engineering damage mechanics: ductile, creep, fatigue and brittle failures, Berlin: Springer; (2005).

[83] S. Murakami, Continuum damage mechanics: a continuum mechanics approach to the analysis of damage and fracture (Vol. 185). Springer Science

& Business Media; (2012).

[84] K. Saanouni, Damage mechanics in metal forming: advanced modeling and numerical simulation. John Wiley & Sons; (2013).

[85] L. Sun, R.H. Wagoner, Complex unloading behavior: Nature of the deformation and its consistent constitutive representation, Int. J. Plast. 27(7) (2011) 1126-1144.

[86] D. Li, R.H. Wagoner, The nature of yielding and anelasticity in metals, Acta Materialia 206 (2021) 116625.

[87] K. Yamaguchi, H. Adachi, N. Takakura, Effects of plastic strain and strain path on youngs modulus of sheet metals, Met. Mater. 4(3) (1998) 420-425.

[88] R. Perez, J.A. Benito, J.M. Prado, Study of the inelastic response of TRIP steels after plastic deformation, ISIJ International 45(12) (2005) 1925-1933.

[89] A. Ghaei, D.E. Green, A. Aryanpour, Springback simulation of advanced high strength steels considering nonlinear elastic unloading–reloading behavior. Mater Des 88 (2015) 461-470.

[90] K.Y. Seo, J.H. Kim, H.S. Lee, J.H. Kim, B.M. Kim, Effect of

constitutive equations on springback prediction accuracy in the TRIP1180 cold stamping. Metals 8(1) (2018) 18.

[91] F. Yoshida, T. Amaishi, Model for description of nonlinear unloading-reloading stress-strain response with special reference to plastic-strain dependent chord modulus. Int J Plast, 130 (2020) 102708.

[92] S. F. Lajarin, R.A. Chemin Filho, C.J. Rebeyka, C.P. Nikhare, P.V.P. Marcondes, Numerical study on variation of chord modulus on the springback of high-strength steels. Int J Adv Manuf Tech, 106(11) (2020) 4707-4713.

[93] H. Hou, G. Zhao, L. Chen, H. Li, Springback behavior and a new chord modulus model of copper alloy during severe plastic compressive deformation. J Mater Process Tech 290 (2021) 116974.

[94] C. Kim, M.G. Lee, (2021). Finite Element-Based Virtual Fields Method with Pseudo-Real Deformation Fields. Manuscript submitted for publication.

[95] A.H. Cottrell, B.A. Bilby, Dislocation theory of yielding and strain ageing of iron. Proceedings of the Physical Society. Section A 62(1) (1949) 49.

[96] Johnston, W. G., & Gilman, J. J. (1959). Dislocation velocities, dislocation densities, and plastic flow in lithium fluoride crystals. Journal of

Applied Physics, 30(2), 129-144.

[97] E.O. Hall, Yield point phenomena in metals and alloys. Springer Science & Business Media; (2012)

[98] C.Y. Yu, P.W. Kao, C.P. Chang, Transition of tensile deformation behaviors in ultrafine-grained aluminum, Acta Mater. 53 (2005) 4019e4028.

[99] X.H. An, S.D. Wu, Z.F. Zhang, R.B. Figueiredo, N. Gao, T.G. Langdon, Enhanced strength-ductility synergy in nanostructured Cu and Cu-Al alloys processed by high-pressure torsion and subsequent annealing, Scr. Mater. 66(2012) 227e230.

[100] Y. Tomota, A. Narui, N. Tsuchida, Tensile behavior of fine-grained steels, ISIJ Int. 48 (2008) 1107e1113.

[101] S. Gao, M. Chen, S. Chen, N. Kamikawa, A. Shibata, N. Tsuji, Yielding behavior and its effect on uniform elongation of fine grained IF steel, Mater. Trans. 55(2014) 73e77.

[102] G. T. Hahn, A model for yielding with special reference to the yield-point phenomena of iron and related bcc metals. Acta metallurgica, 10(8) (1962) 727-738.

[103] M. Itoh, F. Yoshida, Y. Yamashita, M. Ohmori, FEM analysis for

nonuniform yielding processes in mild steel plates under stretching. JSME international journal. Ser. 1, Solid mechanics, strength of materials, 35(1) (1992) 70-77.

[104] F. Yoshida, A constitutive model of cyclic plasticity. Int J Plast 16(3-4) (2000) 359-380.

[105] F. Yoshida, Y. Kaneda, S. Yamamoto, A plasticity model describing yield-point phenomena of steels and its application to FE simulation of temper rolling. Int J Plast 24(10) (2008) 1792-1818.

[106] F. Aguirre, S. Kyriakides, S., H.D. Yun, Bending of steel tubes with Lüders bands. Int J Plast 20(7) (2004) 1199-1225.

[107] Kyriakides, S., Ok, A., & Corona, E. Localization and propagation of curvature under pure bending in steel tubes with Lüders bands. Int. J. Solids Struct. 45(10) (2008) 3074-3087.

[108] Y. Liu, S. Kyriakides, J.F. Hallai, Reeling of pipe with Lüders bands. Int. J. Solids Struct. 72 (2015) 11-25.

[109] R. Schwab, V. Ruff, On the nature of the yield point phenomenon, Acta Materialia 61(5) (2013) 1798-1808.

Korean abstract

본 연구에서는 HAH 왜곡 이방경화모델을 사용하여 API 강관의 이방강도 예측을 위한 수치 모델을 제안하였다. HAH 모델은 재료의 역 하중 또는 교차 하중 경로를 고려한 재료 거동을 표현할 수 있다. 기존 HAH 모델의 예측 정확도 향상을 위해 다성분 변화 법칙을 적용하였다. 모델을 유한요소해석에 안정적으로 적용하기 위하여 완전 내연 응력 적분법을 처음으로 제안하였다. 제안된 알고리즘은 응력, 등가 소성 변형률 및 모델의 상태변수 전부의 비선형 함수들의 잔여값을 고려하였다. 또한 다양한 적분 알고리즘, 재료 특성, 하중 조건, 변형률 증분에 따른 포괄적인 비교 평가를 수행하였다. 역/교차 하중시 모든 잔여값들을 고려한 완전 내연 알고리즘이 큰 변형률 증분에서도 강건하고 정확한 유동 응력과 r값의 변화를 예측함을 확인하였다. 반대로, 모든 잔여값들을 고려하지 않은 반-외연 또는 부분 내연 알고리즘의 경우 급격한 변형률 하중 변화에서 불안정한 해를 계산할 수 있다. 더불어, 모델의 복잡한 1차 또는 2차 미분 값의 대안을 위해 해석적인 미분과 수치적인 미분을 사용하였을 때 결과를 비교하였다. 개발된 알고리즘은 S-rail 성형 및 스프링백을 정적 내연 유한요소법에서도 안정적으로 계산되었다. 마지막으로 다성분 변화법칙 HAH모델을 굽힘/역굽힘 이후 강판의 방향별 강도 예측에 적용하였다.

굽힘/역굽힘 실험은 일반적인 강관 생산 공정의 변형을 실질적으로 모사하기 위해 고안되었다. HAH모델 사용시 예측된 강도는 실험값과 잘 일치하였다. 하지만, 기존 등방 경화 모델이나 등방-이동 경화 모델을 사용시 강도를 정확하게 예측하지 못 하였다. 역하중에서의 거동만 고려하는 등방-이동 경화모델과 달리 역하중과 교차하중에서의 재료의 거동을 모두 고려하는 HAH모델이 더 나은 예측 정확도를 보였다.

주요어: 이방 경화 거동, 교차 하중, 완전 내연 응력 적분법; 강도 예측; 강관 성형;

학번: 2018-39490

감사의 글

2015년 9월부터 시작한 학부연구생 때부터 박사학위를 마칠 때까지 저의 대학원 생활을 지도해주신 이명규 교수님께 감사를 드리고 싶습니다. 불편할 수도 있는 사제지간이지만 친근하고 스스럼없이 대해주시고, 연구 방면에서나 생활 방면에서나 부족함없이 지원해주신 덕에 행복하게 연구실 생활을 마무리할 수 있었습니다.

연구에 관련된 이론을 공부할 때 도움을 주시고 학위 심사도 맡아주신 이진우 박사님, 졸업 주제 연구를 함께해 주신 POSCO 강수창 박사님, 그리고 바쁜 일정에도 시간을 내주시어 논문 심사에 참가해 주시고 조언을 해주신 유웅열 교수님, 한흥남 교수님께도 감사의 말씀을 드립니다.

지난 연구실 생활을 돌아보니 함께한 동료들 덕에 참 행복했던 것 같습니다. 기초도 없이 아무것도 모를 때 하나하나 가르쳐주고 의지할 수 있다고 느끼게 해준 정연 누나, 우람이형, 원재형 감사합니다. 내가 버릇없이 장난쳐도 받아주고 함께 웃어주고 도와줬던 찬양이형, 우진이형 고맙다는 말을 전합니다. 학부 때부터 같이한 기정이, 나름 공동의 적으로부터 감정을 공유한 동준, 유미, 그리고 우리 차기 방장님 귀여운 경문이, 먼저 졸업한 재민이, 정환이, 수현이, 그리고 곧 졸업할 준호형과 함께해서 내가 아는 다른 대학원생들보다 즐겁게 연구할 수 있었던 것 같아서 고맙습니다. 항상 열심히 하는 커피 파트너 진홍이, 해외진출 꿈꾸는 찬미, 이번에 같이 졸업하는 재승이, 최근 2년 동안 많이 도와준 성환이 모

두 함께해서 너무 즐거웠습니다. 연구적인 접점이 적고 바이러스 때문에 친목을 나눌 기회가 적었다는 핑계로 제가 먼저 다가가지 못했던 서준, 정윤, 건진, 영민 대위님, 서연 누님, 혜진 누님, 지영 누님께 먼저 사과의 말을 드리면서 앞으로 순조롭게 졸업하시길 바랍니다. 그리고 형림 형님, 하시던 연구 잘 마무리하셔서 졸업 마무리하시길 바랍니다.

제가 원하는 일을 항상 옆에서 응원하고 지지해줬던 우리 가족에게 진심으로 감사의 인사를 표합니다. 집에서 말수도 적고 살갑지 못한 아들이지만 항상 옆에서 챙겨주려고 하시는 부모님, 정말 감사하고 사랑합니다. 가끔 티격태격하지만 무슨 일 있을 때 같이 생각하고 고민해주는 누나도 고맙습니다.

마지막으로, 내 대학원 생활을 기다려주고 옆에서 응원해준 내 연인 예쁜 아영아, 고맙고 미안하고 사랑해.

최 홍 진 드림